Investigation into nanostructured carbon-based materials for electrochemical applications

A thesis presented to the University of Dublin, Trinity College

for the degree of

Doctor of Philosophy in Chemistry

by

Hugo Nolan

Under the supervision of Prof. Georg Duesberg

School of Chemistry & CRANN

Trinity College Dublin

2015

Declaration

I declare that the work in this thesis has not been previously submitted as an exercise for a degree to this or any other university and is entirely my own work. Due acknowledgement and references are given to the work of others where appropriate.

I agree to deposit this thesis in the University's open access institutional repository or allow the Library to do so on my behalf, subject to Irish Copyright Legislation and Trinity College Library conditions of use and acknowledgement.

Hugo Nolan, September 2014

Acknowledgements

I must start this section by thanking Prof. Georg Duesberg for giving me the opportunity to do a PhD and for his support over the years. I initially joined his group for a three month undergrad final year research project back in September 2009. I thoroughly enjoyed my time spent in the group then and was fortunate to be able to return to the group full-time in July 2010.

Financial support for my PhD was provided by SFI initially via Georg's CSET CRANN grant and then via his AMBER grant for the last year.

During my time as a PhD student I received tremendous support from many people, but I have to thank Drs. Gar Keeley, Niall Mc Evoy and Ashok Kumar Nanjundan, in particular. The guidance, supervision and, above all, friendship proffered by them got me through my studies.

Of course, most the work presented throughout this thesis involved lots of other people; so there is a long list of colleagues who have assisted me over the years. Prof. Mike Lyons of the School of Chemistry was kind enough to offer the use of equipment and expertise for some electrochemical measurements. Thanks, especially, go to Dr. Richard Doyle, of Mike's group who actually helped with the measurements. Prof. Cormac McGuinness and Steve Callaghan from the School of Physics helped immensely with getting me started on XPS measurements. Prof. Valeria Nicolosi of both Physics and Chemistry and several of her group members; Dr. Beatriz Mendoza-Sanchez, Sean O'Brien and João Coelho all helped with sample preparation and data interpretation for supercap measurements. Within our group Dr. Nina Berner gave a hand and shared no small amount of knowledge with XPS measurements and analysis while Ehsan Rezvani and Maria O'Brien performed TEM studies on samples.

The members of the Duesberg group, both current and former, who I've had the pleasure of working with deserve specific thanks here; Sid, Nikos, Chris, Kay, Hye-Young, Toby, Nina, Ravi, Ehsan, Chanyoung, Christian, Sinéad, Riley, Maria, Marcel, Anne and Sarah.

Allen and Curtis, with whom I've been knocking around College for over eight years now, also deserve a mention. So to, do the people I've shared the office with over the last four years. I did manage to migrate to the best desk in the end! The ever-

evolving group of friends upstairs in the CRANN breakout at lunch time area kept me sane over the years. Some members of other groups who deserve particular mention for lab and social matters include Tom, Paul, Sophie, Brendan, Leo, James, Cormac, Eoin, Alan, Sarah-Louise, Sinéad Cullen, Sam, Hugh and many others. Without naming individuals, the rest of the postgrads and postdocs in the schools of Chemistry and Physics with whom I've shared my time in CRANN and Trinity have also been great.

Playing football on Thursday afternoons has kept my head clear and provided welcome distraction. Thanks to the lads for putting up with my "agricultural" football techniques. Playing rugby with DUFC for the last five years has been a central part of my routine and I don't know how I'd cope without regularly having such an outlet and being part of such a competitive environment.

I also have to thank my girlfriend, Michelle, for the emotional support and time spent together. Finally thanks to all of my family. My parents, Irene and Conor, always give their unwavering support. My sister, Bobbie, and my grandparents, Jo, Kevin, Angela and Gerry have also been a great source of support.

Abstract

Carbon materials, despite their ubiquitousness in nature and long studied properties, continue to be at the forefront of material research today. The last 20-30 years have seen renewed interest in structural allotropes such as fullerenes, nanotubes and graphene; which all bear the same basic bonding structure as graphite. Their discovery has seen an enormous surge in publications of so-called nanocarbons, with an extensive range of applications proposed on the basis of their excellent physical, chemical, electronic, mechanical and optical properties. Although these more recently discovered exotic materials account for the bulk of publications dealing with graphitic carbons, less glamorous but much more processesable materials such as Pyrolytic Carbon (PyC) continue to show great promise in a range of applications.

The chemical modification of carbon materials has been shown to modify their properties in different ways, rendering the material more suited to a given application. One area of heavy interest is the functionalisation of graphitic carbon materials with heteroatoms. Many electrochemical processes and applications have shown markedly enhanced performance with the introduction of dopants or surface functional groups on the electrode surface. N-doping, in particular, has been shown to modify the electronic structure and chemical properties of graphene, improving the material's performance in many applications, including sensing and energy conversion and storage.

This thesis presents functionalisation of graphitic carbon materials based on exposure to gentle reactive plasma conditions. In this technique the damage to the surface of treated materials is minimised by placing the samples downstream relative to the plasma source; eliminating kinetic damage from accelerated ions. Choice of gaseous atmosphere determined the nature of the functional groups introduced to the surface of the material studied. A range of graphitic materials were functionalised using this technique and their electrochemical properties were analysed and the results related to thorough physical and chemical characterisation of these materials.

The first material considered was PyC grown *via* Chemical Vapour Deposition (CVD). This material has been studied for decades and possesses high electrical

conductivity in conjunction with mechanical and chemical robustness; properties well suited to electrodes in electrochemical applications. Oxygen and nitrogen moieties were introduced on the PyC surface *via* either oxygen or ammonia plasma treatments; with both plasma treated films found to have significantly enhanced electrochemical performance. Further measurements showed that oxygen functionalised PyC performs exceptionally well in the simultaneous electrochemical detection of dopamine and paracetamol.

Having established the process with PyC, plasma treatment of graphitic materials was then extended to graphene grown by CVD. Monolayer graphene and few layer graphene (FLG) were grown on copper and nickel catalyst foils, respectively; and subsequently transferred to arbitrary substrates. Spectroscopic analysis of monolayer graphene allowed the structural changes in the film to be quantified as a function of oxygen plasma exposure time. A two step plasma treatment, consisting of an initial oxygen exposure followed by ammonia treatment, was found to introduce nitrogen groups in to the material very effectively. Graphene was found to require oxygen groups be introduced first in order to establish reactive sites for incorporation of further nitrogen groups with the removal of the oxygen moieties. FLG was functionalised with oxygen groups and was found to perform admirably in the detection of various biological molecules.

The ammonia plasma treatment was also used in the simultaneous reduction and N-doping of Graphene Oxide (GO) to form N-doped reduced Graphene Oxide (N-rGO). This material can be produced in gram scale quantities and was shown to have potential in electrochemical energy applications. N-rGO was demonstrated to catalyse the Oxygen Reduction Reaction (ORR), a key reaction in hydrogen fuel cells, and scalable fabrication of N-rGO supercapacitor electrodes was also demonstrated.

Finally, experiments involving graphitic carbon were developed to another family of materials with a layered atomic structure. MoS_2, a Transition Metal Dichalcogenide (TMD), was shown to readily catalyse the Hydrogen Evolution Reaction (HER); a crucial reaction in the clean generation of hydrogen gas. A scalable, reliable synthetic route to produce MoS_2 electrodes using conducting PyC as a backbone was developed. The performance of the MoS_2/PyC hybrid electrode was related to the structural properties of the catalytic MoS_2 surface layer, as probed by spectroscopic techniques.

In summary, a number of novel electrodes were synthesised by controllable and scalable gas phase processes. The electrodes were thoroughly characterised by surface analytical techniques and their electrochemical performance evaluated. The different electrodes showed promise in electrochemical sensing and energy storage and conversion.

Publication Highlights

This section serves to highlight some of the results in this thesis which have been published in peer-reviewed journals.
Elements of work presented in chapter 4 have appeared in the following publications:

1. "Synthesis and analysis of thin conducting pyrolytic carbon films", *Carbon* **50** (3), 1216-1226

   Niall McEvoy, Nikolaos Peltekis, Shishir Kumar, Ehsan Rezvani, **Hugo Nolan**, Gareth P Keeley, Werner J Blau, Georg S Duesberg

2. "Simultaneous electrochemical determination of dopamine and paracetamol based on thin pyrolytic carbon films", *Analytical Methods* **4** (7), 2048-2053

   Gareth P Keeley, Niall McEvoy, **Hugo Nolan**, Shishir Kumar, Ehsan Rezvani, Michael Holzinger, Serge Cosnier, Georg S Duesberg

3. "Nitrogen-doped pyrolytic carbon films as highly electrochemically active electrodes", *Physical Chemistry Chemical Physics* **15** (42), 18688-18693

   Hugo Nolan, Niall McEvoy, Gareth P Keeley, Stephen D Callaghan, Cormac McGuinness, Georg S Duesberg

Elements of work presented in chapter 5 have appeared in the following publications:

1. "Functionalisation of graphene surfaces with downstream plasma treatments", *Carbon* **54**, 283-290

   Niall McEvoy, **Hugo Nolan**, Nanjundan Ashok Kumar, Toby Hallam, Georg S Duesberg

2. "Electroanalytical Sensing Properties of Pristine and Functionalized Multilayer Graphene", *Chemistry of Materials* **26** (5), 1807-1812

   Gareth P Keeley, Niall McEvoy, **Hugo Nolan**, Michael Holzinger, Serge Cosnier, Georg S Duesberg

Elements of work presented in chapter 6 have appeared in the following publications:

1. "Plasma-assisted simultaneous reduction and nitrogen doping of graphene oxide nanosheets", *Journal of Materials Chemistry A* **1** (14), 4431-4435

   Nanjundan Ashok Kumar*, **Hugo Nolan***, Niall McEvoy*, Ehsan Rezvani, Richard L. Doyle, Michael E. G. Lyons, Georg S. Duesberg

2. "Nitrogen-doped reduced graphene oxide electrodes for electrochemical supercapacitors", *Physical Chemistry Chemical Physics* **16** (6), 2280-2284

   Hugo Nolan, Beatriz Mendoza-Sanchez, Nanjundan Ashok Kumar, Niall McEvoy, Sean O'Brien, Valeria Nicolosi, Georg S Duesberg

Elements of work presented in chapter 7 have appeared in the following publications:

1. "Molybdenum disulfide/pyrolytic carbon hybrid electrodes for scalable hydrogen evolution", *Nanoscale*, **6** (14), 8185-8191

   Hugo Nolan, Niall McEvoy, Maria O'Brien, Nina C Berner, Chanyoung Yim, Toby Hallam, Aidan R McDonald, Georg S Duesberg

* denotes equal contributions from these authors.

List of Abbreviations

- AFM: Atomic Force Microscopy
- BPPG: Basal Plane Pyrolytic Graphite
- CNT: Carbon Nanotube
- CV: Cyclic Voltammetry
- CVD: Chemical Vapour Deposition
- DSSC: Dye-Sensitised Solar Cell
- EIS: Electrochemical Impedance Spectroscopy
- EPPG: Edge Plane Pyrolytic Graphite
- ET: Electron Transfer
- FET: Field Effect Transistor
- GC: Glassy Carbon
- GO: Graphene Oxide
- HER: Hydrogen Evolution Reaction
- HRTEM: High-Resolution Transmission Electron Microscopy
- ITO: Indium Tin Oxide
- LPCVD: Low Pressure Chemical Vapour Deposition
- LSV: Linear Sweep Voltammetry
- MFC: Mass Flow Controller
- MLG: Multi-Layer Graphene
- N-PyC: Ammonia plasma treated Pyrolytic Carbon

- N-rGO: Nitrogen-doped Reduced Graphene Oxide
- O-PyC: Oxygen plasma treated Pyrolytic Carbon
- OER: Oxygen Evolution Reaction
- ORR: Oxygen Reduction Reaction
- PAH: Poly Aromatic Hydrocarbon
- PECVD: Plasma-Enhanced Chemical Vapour Deposition
- PMMA: Poly-Methyl Methacrylate
- PPF: Pyrolised Photoresist Film
- PyC: Pyrolytic Carbon
- QCM: Quartz Crystal Microbalance
- rGO: Reduced Graphene Oxide
- RHE: Reference Hydrogen Electrode
- RRDE: Rotating Ring Disk Electrode
- SAED: Selected Area Electron Diffraction
- SE: Spectroscopic Ellipsometry
- SEM: Scanning Electron Microscopy
- STEM: Scanning Transmission Electron Microscopy
- TEM: Transmission Electron Microscopy
- TMD: Transition Metal Dichalcogenide
- XPS: X-ray Photoelectron Spectroscopy
- XRD: X-Ray Diffraction

Contents

Chapter 1

Introduction

This section details the different materials studied throughout this thesis and the motivation for the studies undertaken. The experimental chapters which follow can be broadly categorised into those dealing with graphitic carbon materials (chapters 4-6) and a final chapter which primarily focusses on inorganic layered materials, specifically MoS_2 (chapter 7).

1.1 Graphitic Carbon Materials

It is well established that carbon can form materials with wildly different properties, depending on the bonding configuration. sp^3 hybridisation results in diamond; with each carbon atom tetrahedrally bonded to four other carbon atoms. sp^2 hybridised carbon forms layered graphitic sheets, with each atom bonded to three others and a p_z electron contributing to a delocalised electron cloud. This gives rise to van der Waals bonds between graphitic sheets to form a bulk layered structure. Diamond is extremely hard, transparent and electrically insulating as a result of the rigid bonding configuration. Graphitic carbon possesses strong bonds within the graphitic sheets, but weak interplane bonding causes the bulk material to be quite soft as the layers can slip past each other. Additionally, the delocalised electrons readily conduct electricity and interact with visible light, causing graphitic materials to appear black in colour. All carbon materials considered in this thesis are graphitic carbons with varying properties dependent on their microstructure. The bonding structure of diamond and graphite are shown in fig. 1.1.

Nanostructured carbon materials are often considered to be separate allotropes of carbon in their own right. Fullerenes, most famously Buckminsterfullerenes or "Bucky-balls", consist of carbon atoms arranged in spherical arrangements.[1] Fullerenes, consisting of sp^2 hybridised carbon, are considered a distinct carbon allotrope. The same is true of Carbon Nanotubes (CNTs)[2] and graphene,[3] the

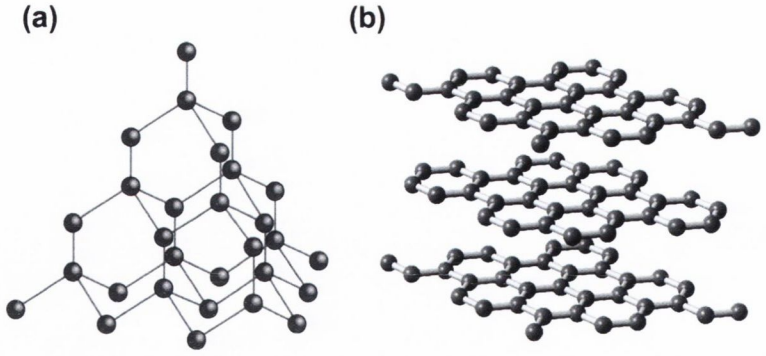

Fig. 1.1. Illustrations showing the bonding structures of ***(a)*** *diamond and* ***(b)*** *graphite.*

latter of which is considered in some detail later in this section.

1.1.1 Pyrolytic Carbon

Pyrolytic Carbon (PyC), also known as Pyrocarbon, is a polycrystalline graphitic material with very small crystallite sizes and turbostratic stacking. The crystallites of this material are arranged at random orientations to each other with some covalent bonding between them. PyC is formed via the pyrolysis of carbonaceous precursors which removes all other substances from the material to result in a nanocrystalline graphitic material. In this study, PyC was formed via pyrolysis of gas phase hydrocarbon precursors in a non-catalysed Chemical Vapour Deposition (CVD) process (more details of which are given in chapter 2). Depending on how growth parameters such as flow rate, temperature, substrate, chamber pressure and deposition time are varied, the orientation and stacking of the crystallites can change. An exhaustive study of the various parameters which influence the deposition of PyC culminated in a series of papers on the topic by Hüttinger and co-workers.[4–11] Originally the studies of the crystalline structure were performed using polarised optical techniques and electron microscopy, with the classification of PyC having its roots in these studies. Reznik and Hüttinger assessed the many classifications of PyC and concluded that the material can broadly be categorised as isotropic, with no overall orientation in the structure, or by virtue of the so-called orientation angle (OA).[12] This is illustrated in fig. 1.2.

Though the structure and physical properties of PyC have been thoroughly studied for decades, its physical, chemical and mechanical properties can yet be exploited for many modern applications. Despite the huge amounts of research and funding dedicated to more recently discovered nanostructured carbon materials such as CNTs and graphene, PyC can still be useful given it has several advantages over more exotic nanocarbons; such as the lack of catalyst required in its synthesis and ease of

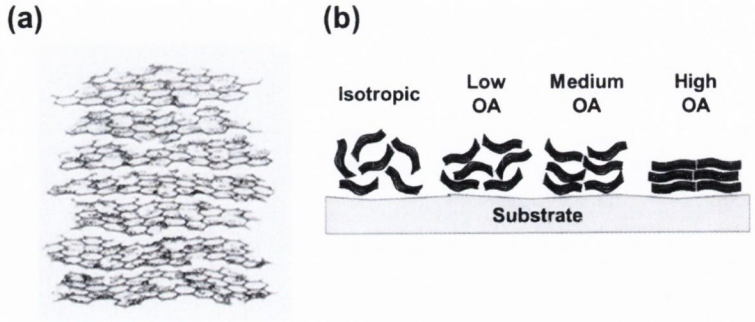

Fig. 1.2. ***(a)*** *Polycrystalline structure of PyC.* ***(b)*** *possible microscopic structural orientations of PyC. Adapted from Reznik & Hüttinger.*[12]

handling. Its excellent properties have lead to it being used as a coating for prosthesis such as heart valves[13] and small orthopaedic implants[14,15] (its bio-compatibility also being desirable for such applications), as a neutron moderator in pebble bed nuclear reactors,[16] in the nose cones of hypersonic vehicles[17] and as a friction material in clutch assemblies.[18] The aforementioned bio-compatibility of PyC has been separately demonstrated in several publications.[19,20] Conformal deposition on to structured substrates and infiltration into porous materials have also been demonstrated.

1.1.2 Graphene

Graphene, a single sheet of graphitic carbon, was first experimentally produced in 2004.[3] Prior to this it had been considered as a useful construct for theoretical studies but questions existed over its physical stability. Fig. 1.3 shows an illustration of an extended graphene sheet. This material exhibits the highest known electrical and thermal conductivities as well as exceptional in-plane mechanical strength. The high electrical conductivity coupled with the unique 2D geometry marks graphene as a material of high interest for electronic devices.[21–25] However, the immediate applicability of graphene to such devices, particularly Field Effect Transistors (FETs) is limited by the fact that graphene exhibits semi-metallic behaviour. Nonetheless, the unique combination of physical, chemical, electrical and structural properties of graphene have made it one of the most investigated materials over the last ten years, with a multitude of proposed and demonstrated applications.

The first production of graphene involved mechanically exfoliating flakes of the material from bulk graphite crystals via the so-called Scotch Tape method.[26] Since then, many more techniques have been developed which produce graphene and related materials of varying quality and yield. Top-down approaches involve removing individual graphene sheets from graphite crystals, while bottom-up

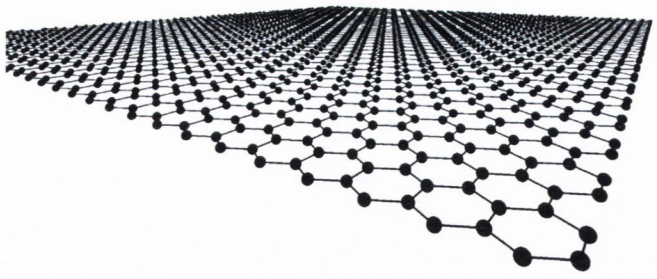

Fig. 1.3. Illustration showing the structure of a single graphene sheet.

approaches involve growing or depositing carbon to form graphene films directly.

Mechanical exfoliation generally produces the best samples in terms of sample cleanliness, crystallinity and monolayer proportion. However, this technique is not easily scalable and only produces isolated graphene flakes. Liquid phase exfoliation of graphene flakes into dispersions in appropriate organic solvents[27] or surfactant stabilised aqueous solutions[28] is carried out by supplying energy, in the form of ultrasonic energy or sheer forces,[29] to forcibly separate the bulk crystals into a liquid dispersion of graphene flakes. This may then be drop-cast or spray-coated onto a substrate and, with the evaporation of the solvent, isolated flakes or even continuous films of graphene result. This process presents a means of producing large scale graphene-based devices and structures; although some issues such as the small flake size, poor yield of monolayer flakes, difficulties controlling the distribution of the lateral flake dimensions and possibility of re-aggregation of flakes upon drying, remain. These two techniques are illustrated in fig. 1.4 (a) and (b), respectively.

Another route towards large scale production of graphene materials involves the exfoliation of graphite oxide flakes from graphite crystals.[30] The extensive coverage of this material with oxygen functional groups causes an expansion in the graphite layered structure and allows the materials to be readily exfoliated and dispersed in water and other polar solvents; facilitating liquid-based processing. Monolayers of this material are known as graphene oxide (GO). The subsequent reduction of GO flakes back to graphene through chemical,[31] thermal[32] and electrochemical[33] means (or combinations of these)[34] re-generates a graphene-like material. An illustration of this is shown in fig. 1.4 (c). This process, however, does not fully restore the GO back to a pure sp^2-hybridised carbon material; some oxygen groups and structural defects remain regardless of the reduction process. Consequently, the resultant material is more accurately referred to as reduced Graphene Oxide (rGO). The residual oxygen present in rGO negatively affects electrical and mechanical performance and limits its practical use in some graphene research and applications. However, certain applications require

large quantities of material rather than pristine quality. Indeed, certain applications, such as electrochemical catalysis, require structural defects in order to facilitate desired reactions. Processes such as liquid phase exfoliation and reduction of GO present suitable techniques to produce graphene or graphene-like material for these applications.

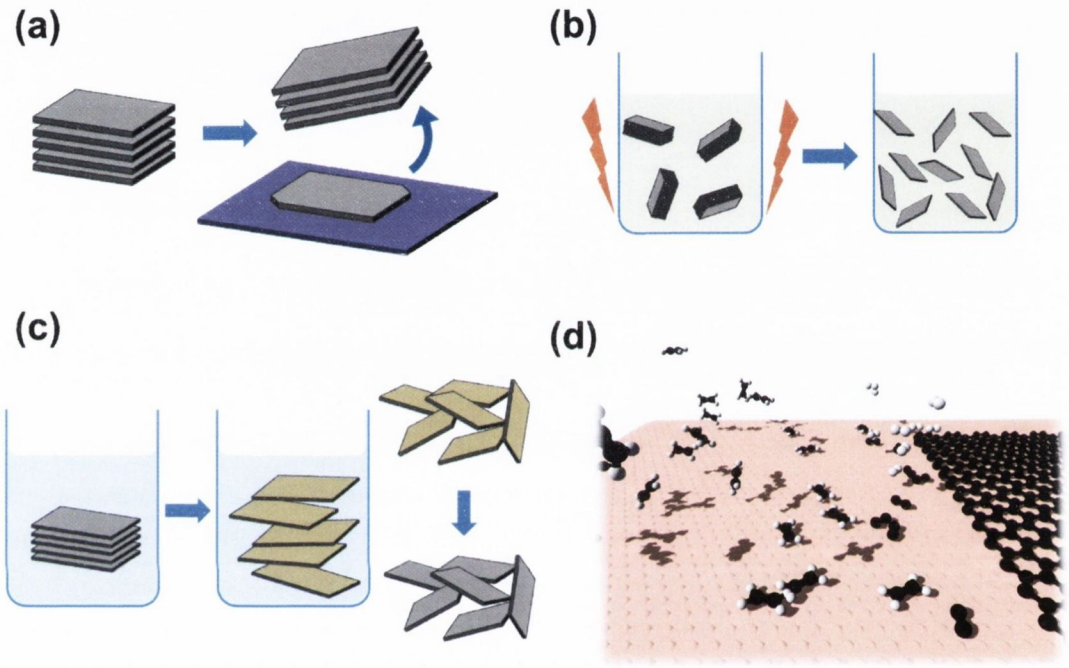

Fig. 1.4. A selection of routes towards the synthesis of graphene. ***(a)*** *Mechanical exfoliation of graphite,* ***(b)*** *liquid phase exfoliation of graphite,* ***(c)*** *reduction of graphene oxide and* ***(d)*** *chemical vapour deposition.*

Bottom-up processes include techniques such as CVD,[35,36] whereby graphene films are deposited directly on the substrate surface from gas phase carbon precursors (illustrated in fig. 1.4 (d)); and the thermal decomposition of SiC, in which annealing of SiC removes Si from the (001) surface and results in the epitaxial growth of graphene.[37] Both of these techniques boast a compromise between compatibility with industrial processing and yield and graphene quality. Other techniques involve joining together molecular assemblies of graphene-like molecules to form extensive graphitic molecular structures.[38] These approaches allow for precise control over the geometry of the molecules and the presence and extent of heteroatoms, but suffer from very low yields.

At this point in this treatise, a note must be made regarding the terminology of graphene. Strictly speaking, "graphene" refers to an idealised single sheet of sp^2-hybridised carbon, as illustrated in fig. 1.3; with all of the unique electronic, physical, chemical and mechanical properties that this structure entails. However,

practically, a much looser definition of this word is used in the literature. Generally speaking, graphene is understood to mean "graphene-like" and encompasses few layer graphene and heavily disordered graphitic materials. Indeed, some publications describe material as graphene, when it is patently structurally more like PyC or even graphite. In this document, care is taken to use appropriate and accurate names when discussing the materials studied. "Graphene" concerns monolayer films of the same, "few layer graphene" describes thin graphitic films with properties tending towards that of bulk graphite and, finally, "reduced graphene oxide" is used for rGO, even though rGO is often called graphene in the literature.

1.1.3 N-Doping of Graphitic Carbon

Doping of carbon with heteroatoms can significantly alter the physical, electronic, optical and chemical properties of these materials. In particular, Nitrogen doping (N-doping) of graphitic materials has been extensively studied as these materials possess tremendous potential for a myriad of applications ranging from energy[39,40] to sensing.[41–43] Incorporation of nitrogen in to the structure of graphitic materials can take place in a number of configurations. Direct substitution of a carbon atom for a nitrogen atom in the basal plane of a graphitic layer with no further crystalline rearranging is known as quaternary or graphitic nitrogen. In this case, the extra electron in the nitrogen contributes to the delocalised π-electron cloud; providing extra charge carriers. Should this substitution of nitrogen for carbon take place at the edge of a graphitic layer, this is known as pyridinic nitrogen. This configuration contributes two extra electrons to the π electronic system and, additionally, contributes to the increased reactivity of the edge plane regions of the material. Pyrrolic nitrogen occurs in five membered ring structures at edge plane sites, also contributing two electrons to the π system. Both quaternary and pyridinic nitrogen configurations are sp^2 hybridised, while pyrrolic nitrogen exhibits sp^3 character.[44] Nitrogen can also bond to the carbon lattice in an out of plane manner via the attachment of amine groups to the material. These configurations are illustrated in fig. 1.5.

The extra electrons donated by the nitrogen result in N-doped carbons showing *n*-type[45] charge carrier behaviour with increased charge carrier concentration but with lower carrier mobilities than for pristine graphitic materials.[46] Modulation of the extent of N-doping of graphene has been theoretically demonstrated to allow control of the electronic properties of graphene.[47] However, experimental work has only succeeded in opening a small band gap in size; too small for incorporation in to FET devices.[48] The greater chemical activity at N-dopant sites is of particular

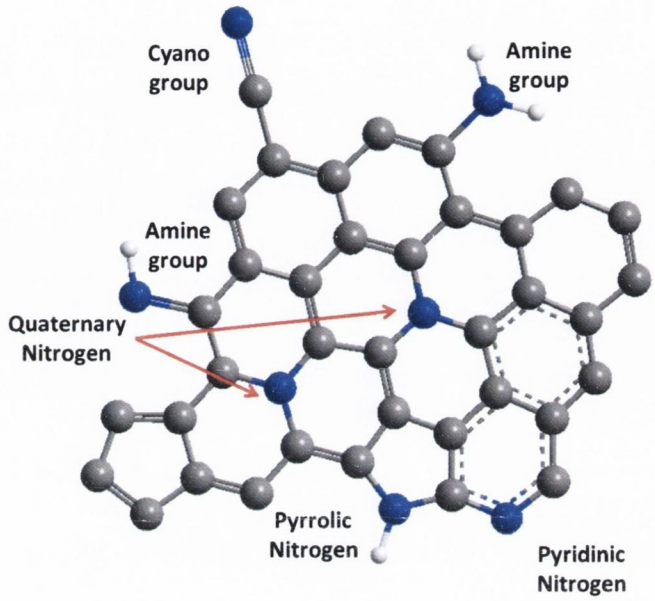

Fig. 1.5. Schematic illustrating different possible configurations on N-doping in a graphitic system; pyridinic, quaternary and pyrrolic Nitrogen. Also included are a number of possible Nitrogen functional groups such as cyano groups and amines (primary and secondary amines are illustrated here). Note that Hydrogen atoms terminating the graphitic lattice have been omitted for image clarity.

interest for electrocatalytic reactions; which are of great significance as an alternative to expensive noble metal catalysts for the Oxygen Reduction Reaction (ORR) in hydrogen fuel cells,[40,42,49,50] increased cycling stability in Li-ion batteries[39,51] and sensing.[43,52] Indeed, the biocompatibility of both CNTs and graphene has shown to be enhanced through N-doping[53], which has a bearing on the sensitivity of these materials compared to pure carbon materials.[41]

Although their fascinating properties endow them with great potential, the successful adoption of graphene based materials for useful applications also relies on factors such as cost, processability and mass production in addition to chemical requirements. Thus, the successful approach to N-doping of graphitic materials must satisfy a number of criteria for the technique to be useful beyond academic interest. Many works have dealt with various approaches to the functionalisation of CNTs[54] and graphene using methods both *in situ* during synthesis[45] and *ex situ* post-synthesis.[55] N-doping of less exotic carbon materials has also been investigated for various applications. N-doped activated carbon has been shown to improve the adsorption of SO_2 and NO gas for scrubbing of exhaust fumes.[56,57]

1.2 Inorganic Layered Materials

Recent trends in the research community have seen a dramatic rise in the interest in a family of layered 2D materials known as Transition Metal Dichalcogenides (TMDs).[58,59] The basic structure of these materials is MX_2, where M is a transition metal and X represents a chalcogen such as sulfur, selenium or tellurium. This is shown in fig. 1.6 (a). The huge number of combinations of transition metals and chalcogens which can exist results in a veritable plethora of possible TMDs. Fig. 1.6 (b) highlights a number of transition metals and chalcogens which are known to form compounds with a layered structure. The physical, chemical and electronic properties of these various TMDs vary wildly, which allows these materials to be exploited as required by different applications.

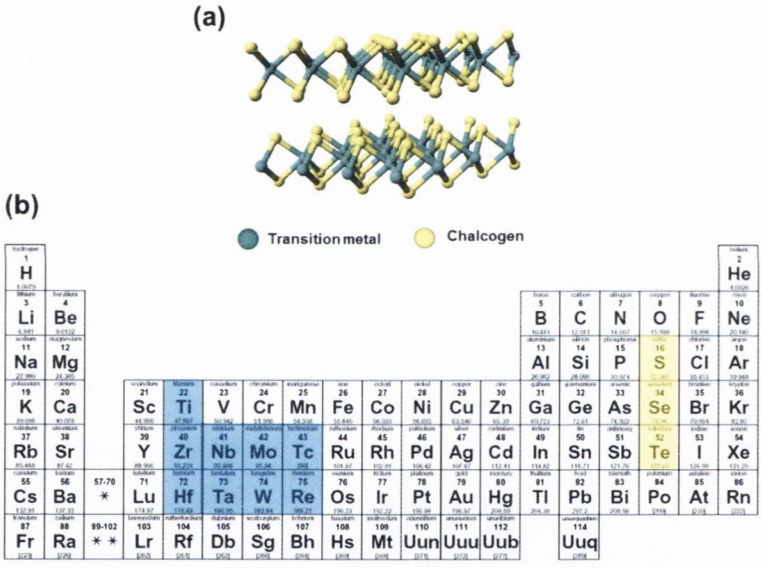

Fig. 1.6. ***(a)*** *Illustration showing the structure of a monolayer of a typical TMD.* ***(b)*** *Periodic table showing the various elements which can be combined to form layered TMDs.*

TMDs of the form MX_2 can exist in the so-called 2H phase, a trigonal prismatic structure, or 1T phase, an octahedral structure.[60] MoS_2, as an example, only occurs naturally in the semiconducting 2H polymorph, but can be converted to the metallic 1T phase *via* ion intercalation techniques.[61] Illustrations of these two solid phases for MoS_2 are shown in fig. 1.7.

The properties of the bulk crystalline forms of many TMDs (layered or otherwise) have been well known for many years. MoS_2 has been extensively used as a solid lubricant as the weak interlayer bonding facilitates sliding of adjacent layers to reduce friction in mechanical assemblies. The high temperature stability of MoS_2 has seen it employed as a dry lubricant over other layered materials such as

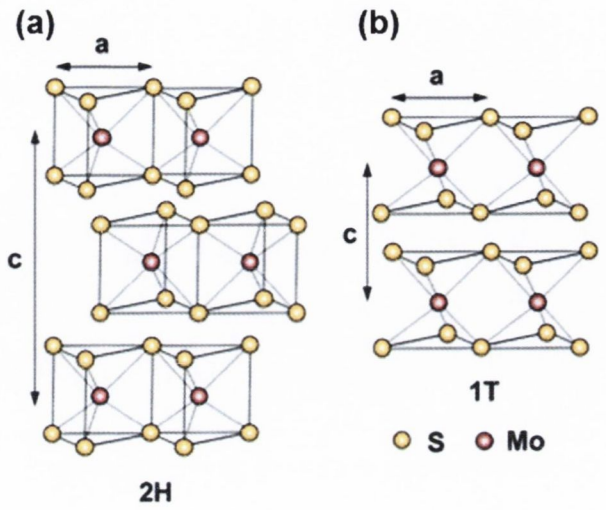

Fig. 1.7. ***(a)*** *2H and* ***(b)*** *1T structures of MoS_2. Reproduced from Huang et al.*[60]

graphite. While the properties of bulk quantities of many TMDs have been well established for some time, recent advances in graphene research have seen techniques used for isolation of monolayer materials applied to inorganic layered materials such as layered TMDs.[59] Isolation of monolayers of TMDs has shown that these materials exhibit radically different properties to their bulk form and, consequently, a vast number of applications have been proposed.

The semiconducting nature of certain layered TMDs is of particular interest for electronic applications. Bulk TMDs typically show an increase in the bandgap, E_g, upon reduction in dimensionality to monolayer, with an accompanying change from indirect to direct bandgap behaviour. For example, Splendiani *et al.* showed this for MoS_2 and related these changes in band structure to the emergence of photoluminescence in monolayer MoS_2.[62] The band structure calculated for bulk (E_g=1.29 eV), 4 layer, 2 layer and monolayer (E_g=1.9 eV) MoS_2 is shown in fig. 1.8. It has been proposed that further engineering of the electronic properties of MoS_2 may be performed via strain engineering of the films.[63,64] There are reports of logic applications with TMD FET devices with monolayer MoS_2 exhibiting n-tpye behaviour.[65,66]

The main application areas in which MoS_2 and other TMDs have been investigated are in catalysis and energy applications; with these two fields often related. TMDs have been demonstrated as useful in solar energy harvesting, both in photovoltaic devices[67] and as counter electrodes to boost the efficiency of Dye Sensitised Solar Cells (DSSCs).[68] These materials have also been used in electrocatalysis and photocatalysis as alternatives to established expensive noble metal catalysts, with the most well known example being the use of TMD electrodes

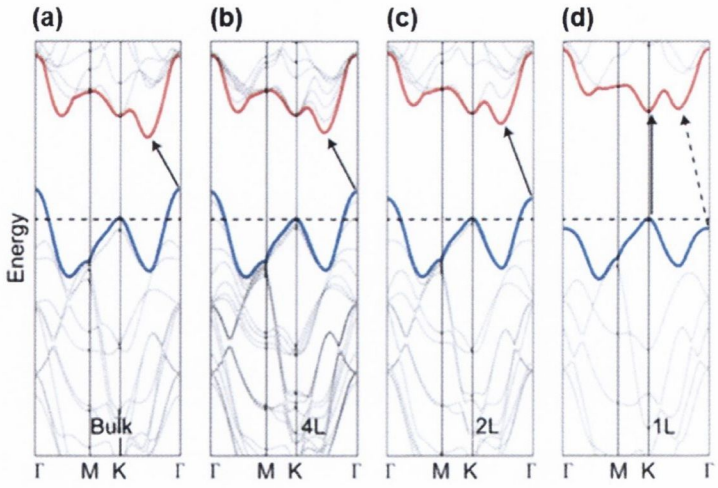

Fig. 1.8. Calculated band structure for (a) bulk, (b) 4 layer, (c) bilayer and (d) monolayer MoS_2. Reproduced from Splendiani et al.[62]

to catalyse the Hydrogen Evolution Reaction (HER).[69,70] This involves the production of H_2 gas from aqueous media *via* electrochemical means.

Hydrogen Evolution Reaction

Efficient and sustainable production of hydrogen is essential for a hydrogen-based economy to reduce our dependence on fossil fuel energy sources.[71] The electrochemical splitting of water *via* proton reduction in the HER provides a feasible route towards this without dependence on consumable resources. However, to date, the best HER performance has been achieved using prohibitively expensive platinum electrodes, severely limiting the practical applications of this technology. If the HER is to be exploited as a viable energy source, alternative electrocatalysts to Pt must be sought. TMD electrodes, among the wide range of investigated catalysis applications, have shown promising catalytic activity towards the HER.[70,72,73]

Thus far, MoS_2 has been the most heavily studied material in the context of HER catalysis, although studies on the HER behaviour of other materials such as $MoSe_2$, WS_2 and WSe_2 have recently emerged.[74–76] Depending on the synthesis route undertaken, HER activity has been attributed to different features of TMD layers. Where MoS_2 flakes have been exfoliated from bulk material *via* intercalation of Li-ions, it has been demonstrated that the HER activity is related to the presence of the 1T polymorph.[77,78] This is not found in bulk MoS_2, which consists solely of the 2H polymorph. Many other studies have attributed HER activity of MoS_2 to the presence of unsaturated sulfur atoms along molybdenum edges of the MoS_2 structure.[79,80] Furthermore, theoretical studies have shown that sulfur vacancies

catalyse various reactions at the MoS_2 surface.[81] These defects, in the otherwise catalytically inactive basal plane of the sulfur sub-lattice, act as catalytically active sites.

Evaluation of HER catalysts is carried out principally by assessing two key metrics; the onset potential and Tafel slope. The onset potential signifies the overpotential which must be applied to the working electrode before proton reduction takes place. The more efficient a material is in catalysing the HER, the lower the potential which must be applied to the electrode; a greater change in current for a given change in applied overpotential is observed. Hence, H_2 fuel can be generated with a lower total power input. Analysis of the Tafel slope for a particular catalyst provides an insight in to the mechanism by which the HER proceeds. Certain reaction mechanisms are more energetically favourable and, thus, it is desirable to engineer a catalyst to follow this reaction route. Details concerning the analysis of the electrochemical data for HER are given in chapter 2.

1.3 Thesis Aims and Objectives

The work presented in this thesis is primarily concerned with the preparation of various electrode materials and understanding the electrochemical performance of these materials *via* thorough physical and chemical characterisation. In chapters 4 and 5 plasma treatment of graphitic films is used to change their surface chemistry and, hence, modify electrochemical processes at the surfaces. The motivation for this is towards the production of inexpensive electrochemical sensing platforms. Chapter 6 aims to produce gram scale of materials for electrochemical energy applications using a novel technique for the simultaneous reduction and N-doping of GO. Finally, TMDs are considered for further energy conversion and storage applications in chapter 7. In particular, efforts were made to improve the catalytic performance of MoS_2 films. In all the works presented, achieving final goals was predicated on thorough characterisation of the studied materials to fully understand the electrochemical processes occurring at the surfaces of these materials.

Chapter 2

Theory and Background

This chapter explains the theory underpinning the various techniques utilized throughout this thesis. Firstly, the understanding behind techniques used to produce and modify the materials are dealt with; then characterisation techniques are explained so as to provide an understanding of the results presented in chapters 4-7. Specifics pertaining to equipment and processes used are briefly dealt with in chapter 3.

2.1 Chemical Vapour Deposition

Deposition of materials *via* CVD occurs whereby precursor compounds in the vapour phase react or decompose over a sample surface, resulting in deposition of the desired material. CVD is highly versatile and, as such, is used across a wide range of industries and fields of science as it allows the deposition of uniform films with good control over properties such as thickness, chemical composition, crystalline structure and conformality. The technique is scalable, making it attractive to industries and processes which call for large scale production of material with uniform properties. Many variations on the basic technique exist to further control or optimise the process, depending on the desired results. These include Low Pressure CVD (LPCVD), in which all processes are carried out below atmospheric pressure; and Plasma Enhanced CVD (PECVD), where energy is imparted to the precursor compounds by plasma in addition to or as an alternative to more usual thermal energy sources. Another CVD variant is Atomic Layer Deposition (ALD) which uses a two-step self-limiting deposition to form compounds in a layer-by-layer manner. This is particularly useful for depositing extremely thin, but uniform, films such as gate dielectrics in the semiconductor industry. All CVD processes involved in the various studies in this work can be classified as LPCVD as all deposition/processing takes place at pressures of the order of 1 Torr.

Typically, precursors consist of volatile gases which undergo chemical reactions or thermal decomposition to form reactive intermediate species which then interact with the sample surface. After physisorption on to the sample surface, these species can undergo a number of subsequent steps such as desorb back into the gas phase or diffuse along the substrate surface. These mobile adsorbates can then react with defects or features in the substrate surface or with further adsorbed species. The latter results in the nucleation into clusters which ultimately grow as further adsorbed species react and join up with the nucleating cluster. In some cases, precursor species can adsorb directly on to clusters out of the gas phase without first interacting with the substrate surface. Fig. 2.1 illustrates some common surface processes involving adsorbed species.

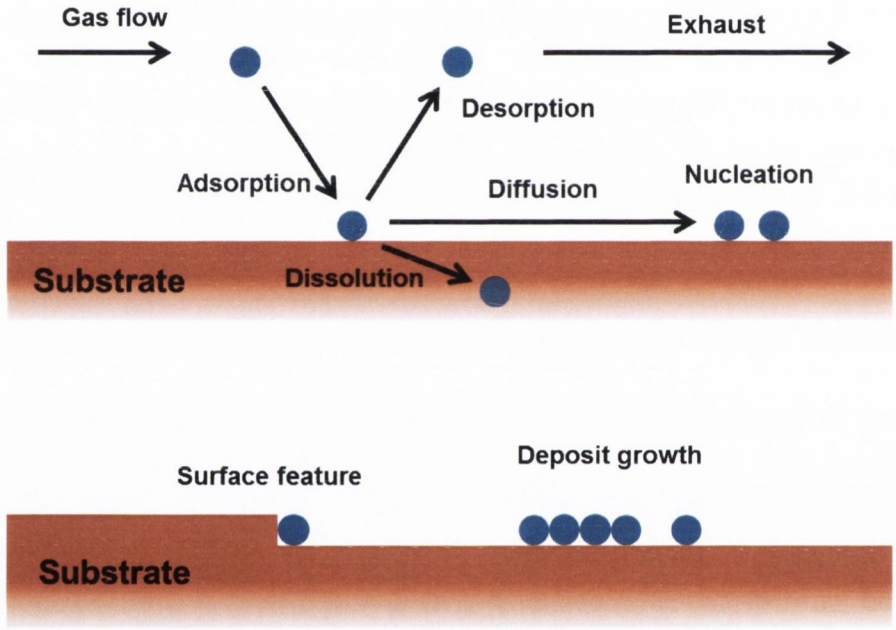

Fig. 2.1. Schematic representing the possible interactions which can occur between a reactive species (blue) with a substrate (orange).

The nature of the substrate plays a key role in determining the nature of the final deposit as the interaction between the substrate surface and the deposit determines the deposition regime which occurs. When the adsorbates and nucleating crystals are more strongly bound to each other than the substrate, islands of growth occur. This is known as the Volmer-Weber growth mode. When there is a strong interaction between the substrate and the deposit, the Frank-van der Merve growth mode is preferred, where complete layers of the deposit grow before subsequent layers form. In some cases, another growth mode occurs when initially layer by layer growth is favoured, but, after the completion of one entire layer, subsequent layer growth is unfavourable and islands form atop the initial layer. This is known as the Stanski-

Krastanov mode. A schematic of these growth modes is shown in fig. 2.2. These growth mechanisms are explained in greater detail by Venebals *et al.*[82] In CVD of carbon materials, control of the growth substrate allows one to readily control the nature of the deposited film to favour highly crystalline layered materials such as graphene or randomly arrayed polycrystalline films such as PyC.

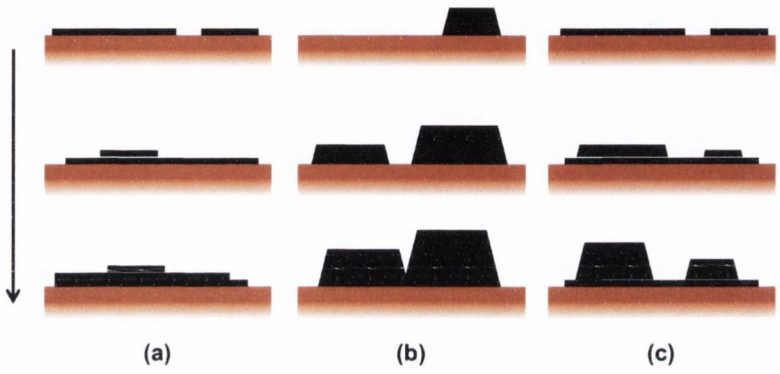

Fig. 2.2. Schematic representing different crystal growth modes during deposition. ***(a)*** *Volmer-Weber,* ***(b)*** *Frank-vander Merve and* ***(c)*** *Stranski-Krastanov. The arrow on the left hand side represents increasing deposition of material.*

2.1.1 CVD of Pyrocarbons

All CVD of carbon materials in this work was performed via the thermal decomposition of hydrocarbons over appropriate substrates. CVD of carbon materials is a highly complex process as there are a great many possible reaction pathways involving the competition of heterogeneous and homogeneous reactions in the gas phase. Some heterogeneous reactions involve the nucleation of carbon from the vapour phase forming soot. These reactions can be minimised by ensuring low hydrocarbon partial pressure and residence time in the reactor. The nature of the homogeneous reactions which occur via thermal decomposition before deposition onto the substrate are explained in some detail by Benzinger *et al.*[4] These reactions involve dehydrogenation and cracking of C-C bonds. Possible reaction pathways are shown in fig. 2.3, which shows an example of a heterogeneous surface reaction where methane interacts with a surface adsorption site, or various homogeneous vapour phase reactions where various hydrocarbon species and intermediates can be formed from methane.

The choice of precursor hydrocarbon has been shown to have an effect on the reaction pathway involved in the deposition of PyC by virtue of the various carbon radicals formed during the CVD process. This is thoroughly dealt with by Becker and Hüttinger where it is shown how hydrocarbons with varying carbon content

(a) $CH_4 + 2S() \rightarrow S(CH_3) + S(C)$

(b)
$CH_4 + H \rightarrow CH_3 + H_2$
$CH_3 + CH_4 \rightarrow C_2H_5 + H_2$
$C_4H_6 \rightarrow + C_4H_4 + H_2$
$C_2H_5 \rightarrow C_2H_4 + H$
$C_2H_4 + CH_3 \rightarrow C_2H_3 + CH_4$
$C_2H_3 \rightarrow C_2H_2 + H$

(c)
$C_2H_2 + C_2H_2 \bullet \rightarrow C_4H_4 \bullet$
$C_4H_4 \bullet + C_2H_2 \rightarrow C_6H_6 \bullet$
$C_6H_6 \bullet + M \rightarrow C_6H_6 + M \bullet$

Fig. 2.3. ***(a)*** *A possible interaction between methane and free surface sites on substrate, S().* ***(b)*** *Formation of acetylene from methane.* ***(c)*** *Formation of benzene from acetylene with a non hydrocarbon molecule; • Indicates excited molecule. All reproduced from Hüttinger and co-workers.*[4]

affects the deposition of PyC.[6–8] The reactor design[8] and growth temperature[9] and pressure[11] are also extremely important for CVD processes. Substrate choice affects the nature and rate of deposition as the number and layout of active surface adsorption sites influences the kinetics and rate of carbon deposition. Delhaes showed how changing the growth temperature, carbon partial pressure or residence time of the carbon species can change the microstructure of CVD grown PyC films.[83] Phase diagrams illustrating the different deposition regimes are shown in fig. 2.4.

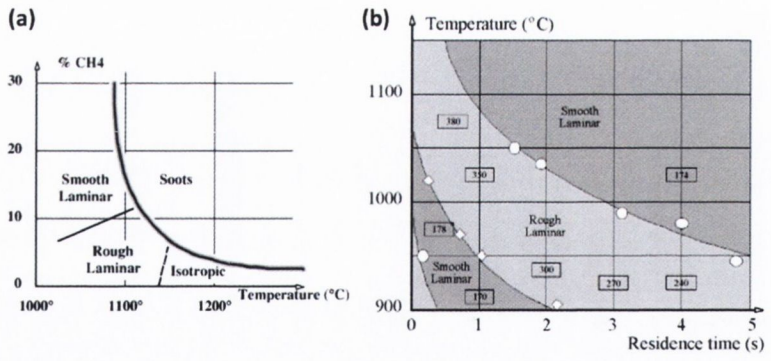

Fig. 2.4. (a) Carbon concentration-temperature and (b) temperature-residence time phase diagrams for the different PyC microstructures obtained via CVD of methane. Reproduced from Delhaes.[83]

Growth of carbon deposits *via* CVD can proceed by two differing mechanisms which ultimately governs the microstructure of the resultant film. Balancing various reaction parameters such as richness of the hydrocarbon source, temperature, residence time etc allows the different regimes to dominate. Carbon species can chemisorb on to edge plane carbon sites on existing deposits, leading to growth of existing graphitic crystals; or physisorb on to basal planes leading to nucleation of

new graphitic crystals. The former is known as the "growth mechanism", whilst the latter is known as the "nucleation mechanism". These mechanisms are discussed in detail by Hu and Hüttinger.[84] These growth mechanisms are illustrated in fig. 2.5.

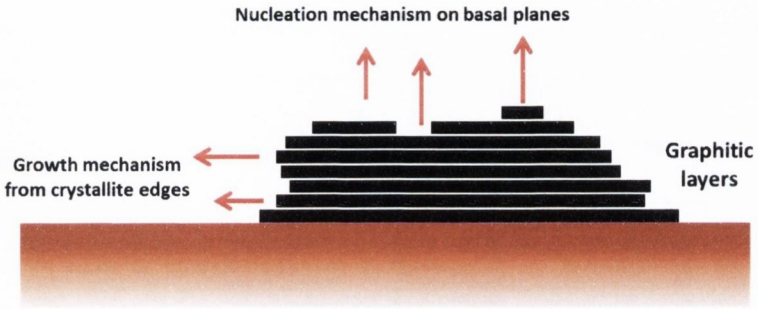

Fig. 2.5. Illustration of the nucleation and growth mechanisms of carbon growth as discussed by Hu and Hüttinger.[84]

PyC Deposition

As illustrated in fig. 2.3, hydrocarbons which undergo thermal decomposition can then undergo vapour phase reaction to form various carbon species including aromatics or Poly Aromatic Hydrocarbons (PAHs). Larger molecules favour physisorption on graphitic basal planes and, consequently, the growth of polycrystalline deposits such as PyC. Furthermore, the interaction between the deposit and growth substrate heavily influences the microstructure of the deposit. This is dealt with in detail by Hüttinger.[85] The high interfacial energy between SiO_2 and carbon deposits and the very different crystalline structures of the two materials, coupled with the poor mobility of carbon physisorbed on SiO_2, results in the formation of PyC when this growth substrate is used. Physisorption of carbon species on either the substrate or existing graphitic deposits is not favoured and little to no re-organisation of adsorbates results in randomly oriented crystallites with small lateral dimensions. Some control of the crystallite size and PyC microstructure can be achieved by varying reaction parameters such as temperature, residence time and hydrocarbon source, as outlined in the previously cited papers in this section. Additionally, introducing further gaseous species, such as hydrogen, into the vapour mixture can have a large influence on the nature of the resultant deposit *via* competition with carbon radicals for surface adsorption sites.[86]

Graphene Growth

The use of certain transition metals as growth substrate dramatically changes the microstructure of the graphitic deposit. In the case of Ni substrates, the lattice

mismatch between graphitic planes and the Ni(111) plane is rather low with a low interfacial energy.[87] Carbon adsorbates on this surface are significantly more mobile than in the case on SiO_2 and, thus, these adsorbates are capable of diffusing across the substrate surface until chemisorbing on to edge plane sites of nucleation sites/crystallites, resulting in further growth of these crystallites. This follows the aforementioned growth mechanism. Additionally, Ni acts as a catalyst for the reactions which break hydrocarbons into constituent carbon and hydrogen. The growth mechanism has been shown to dominate with smaller light hydrocarbons and, thus, favour more ordered graphitic growth. Step edges in the Ni surface and other crystalline defects also act as chemisorption sites for carbon species, which increases the deposition rate further.[88,89] The different grains of Ni a typical polycrystalline Ni film present different crystalline facets to the surface resulting in different growth rates on different parts of the Ni film.[90] In addition to vapour phase deposition of graphitic material directly on the Ni surface, a secondary mechanism occurs whereby carbon dissolves into the bulk Ni at high temperatures and segregates to the surface under cooling.[91] This has been observed for isotope labelled carbon by the group of Ruoff.[92] As a result, growth on Ni results in rather thick graphitic deposits which is problematic for the deposition of monolayer graphene.

Cu was first used for the growth of large area monolayer graphene by Li *et al.* of the Ruoff group in 2009.[93] The Cu(111) surface has a very low lattice mismatch with graphitic layers, but the extremely low solubility of carbon in Cu precludes the secondary precipitation mechanism during growth of the graphitic deposit. In addition to this, the differences in electronic structure between Cu and Ni means that the energy barrier of chemisorption of carbon species on to Cu is approximately four times that of Ni.[94] As a result, these species have a sticking coefficient on Cu five orders of magnitude less than on Ni.[95] Consequently, growth of graphitic layers on Cu with CH_4 is mostly limited to monolayered graphene. In the graphene studies presented in this work, both monolayer and few-layer graphene were grown on Cu and Ni foils, respectively.

2.2 Plasma Treatments

Plasma is a gaseous-like state whereby a portion of the atoms or molecules are ionised. Plasma is considered to be a distinct state of matter owing to its unique material properties. The laws governing the motion of particles in plasma are established by the forces between near-neighbours.[96,97] Plasmas are generated in laboratory environments by imparting energy into a gas via electric current (glow discharge

diode) or radio waves (inductively coupled plasmas); electrons absorb this energy and particles become ionised. Owing to the fact that the electrons absorb most of the applied energy in generated plasmas, separate parameters describing the temperature (energy) of the electron, T_e, and the temperature of the ion, T_i, are used. These parameters are used to categorise plasma types.

Species present in plasma can interact with other "normal" matter in a number of ways. Plasma ions and radicals can in turn radicalise gaseous particles and etch solid materials through kinetic and chemical reactive interactions. The plasma treatment techniques used throughout this work exploited the reactive nature of the plasma radicals in interactions with various materials.

2.3 Raman Spectroscopy

Raman spectroscopy is an extremely powerful characterisation technique which probes the vibrational energy levels of a material and can reveal a wealth of information about a material's crystalline structure. This phenomenon was first observed by Sir C.V. Raman and K.S. Krishnanin 1928,[98] for which Raman received the Nobel prize in physics in 1930.

Upon irradiation of a sample with light, an excitation of an electron promotes it from its ground state to a virtual level. Typically, recombination occurs as the electron relaxes back to its initial state with a corresponding photon emission of equal energy to the incident photon. This is known as Rayleigh Scattering. However, a small portion of the excited electrons (1 in 10^7) undergo inelastic scattering involving phonon interactions prior to relaxation back to its original state. This is illustrated in fig. 2.6. Relaxation back to a higher energy than the initial energy results from the electron having lost energy. The emitted photon will have a longer wavelength (or higher energy) than the incident light. This is known as Stokes Raman scattering. The opposite of this scenario, where the emitted photon has a shorter wavelength (or higher energy) than the incident light, is known as Anti-Stokes Raman scattering. The relative intensity of Stokes scattered light is much higher than that of Anti-Stokes scattered light.[99,100] This is due to the fact that, at room temperature, the majority of molecular vibrational modes are in the ground state, as governed by the Boltzmann distribution. The relative intensity of Stokes scattering is related to the number of vibrational modes in the ground state, while Anti-Stokes scattering arises from the number of vibrational modes in the next highest excited state. Where the excitation energy is close to that of an electronic transition, resonant Raman scattering occurs. This greatly increases the intensity of the Raman process.

The polarisability of a molecule has an important bearing on the strength of the

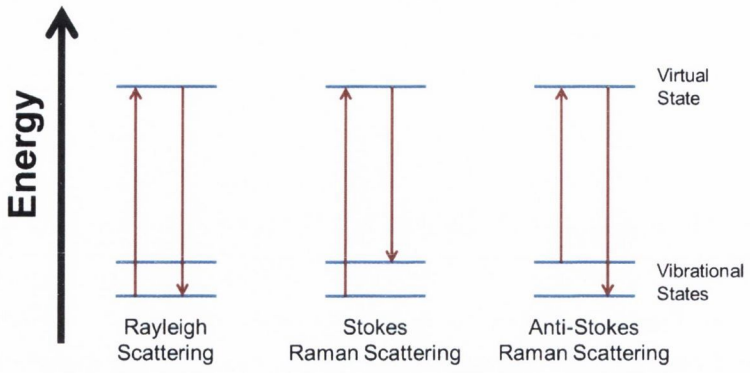

Fig. 2.6. Illustration of different elastic and inelastic scattering processes resulting from irradiation of a sample with light.

interaction between the incident photon and the molecule's electron cloud. If the polarisability of a material changes upon interaction with an incident photon (or other external field), the material is said to be Raman active. Distributed electron clouds such as the π-clouds in graphitic materials are easily polarised and, as such, exhibit very a strong Raman effect. Thus, this technique is highly suited to the characterisation of graphitic carbons.

To generate a Raman spectrum, the scattered light is gathered and passed through a monochromator before being detected. Most of the Rayleigh scattered light is filtered out and only the Raman scattered light is analysed. A series of peaks are observed on the resultant spectrum which correspond to specific photon-phonon interactions within the sample material.

2.3.1 *Raman Spectrum of Graphitic Materials*

The Raman spectrum of graphitic materials is well established and has been used to analyse materials such as graphite,[101] amorphous carbon[102] and fullerenes.[103] Recent years have seen great interest in the Raman spectrum of graphitic materials corresponding to the level of interest in graphene in the research community.[104] The primary features of the Raman spectrum for graphitic materials are peaks which appear at Raman shifts of ~1340 cm^{-1}, ~1580 cm^{-1} and ~2700 cm^{-1}. These are known as the D, G and 2D bands, respectively. Visible excitation resonates with the π-states of graphitic or sp^2 hybridised carbon and, thus, the Raman spectra for graphitic carbon dominates even in amorphous carbons with a high sp^3 content. The G band arises due to in-plane vibrations with E_{2g} symmetry and is present in all graphitic systems, while the D band is related to structural defects in the crystalline structure. The D band is related to breathing mode vibrations of A_{1g} symmetry, which

requires ring structure defects to be present in the system. This mode is forbidden in defect free graphitic structures.

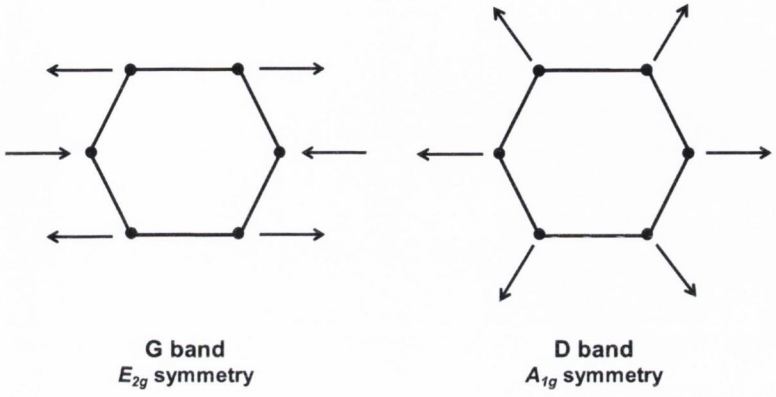

Fig. 2.7. Illustration of E_{2g} and A_{1g} vibrational modes related to G and D bands, respectively.

The D band is a single phonon process of which the 2D band is the two-phonon overtone of the transition. Both the D and 2D bands involved resonantly enhanced scattering processes, which results in an intensity comparable to that of the G band. Fig. 2.8 shows a schematic of double resonant Raman scattering. An incident photon causes an electron to be excited to a state marked by *a*. Double resonant scattering occurs if the electron is scattered from here to another electronic state, *b*. Interaction with a second phonon or lattice defect can scatter the electron to state *c*, from where it recombines with a hole to relax back to *d*, its original state. This gives rise to the D band, while the second order of this interaction with zone boundary phonons gives rise to the 2D band.

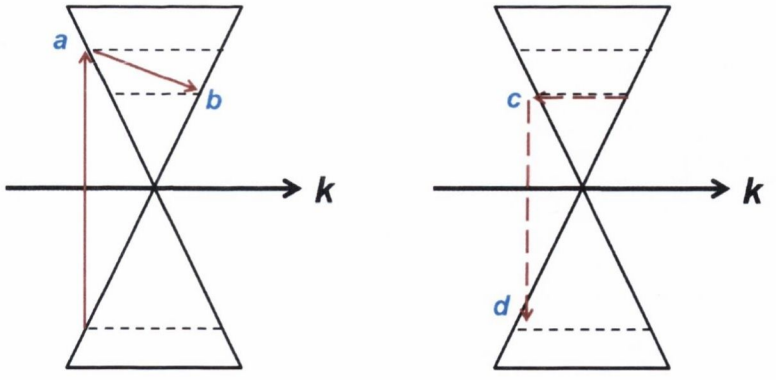

Fig. 2.8. Double resonant scattering mechanism. Electron is excited to a by an incident photon, the electron is scattered to b by a phonon interaction before further scattering to c and finally recombination back to initial state, d. This mechanism accounts for the D' band.

The D band arises due to so-called inter-valley scattering of electrons between the K and K' positions in the graphene Brillouin Zone. This is illustrated in fig. 2.9.

The scattering process shown in fig. 2.8 is known as intra-valley scattering, where the entire scattering process occurs at a single K position. In addition to the D band, another defect-related peak arises due to intra-valley scattering and is known as the D' band. This manifests as a peak at ~1620 cm^{-1}. The D' band typically appears as a shoulder on the G band.[105] In graphitic systems where a wide range of defect sizes exist, an increase in the width of the D' and G bands occurs which causes these two features to merge.

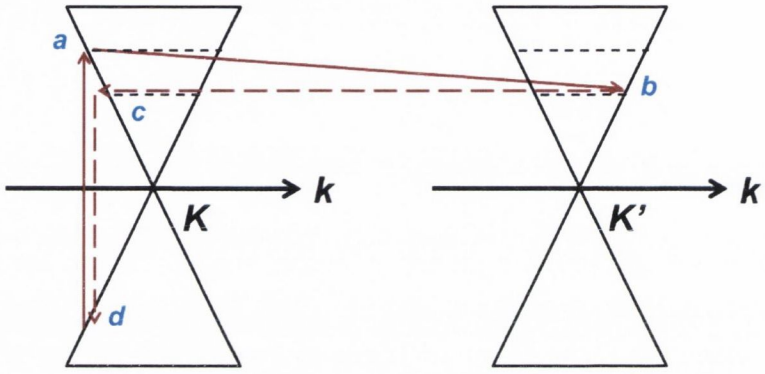

Fig. 2.9. Double resonant inter-valley scattering mechanism. Electron is excited to a by an incident photon at K position, the electron is scattered to b at the K' position by a phonon interaction before further scattering to c and finally recombination back to initial state, d. This mechanism accounts for the D band.

The Raman spectrum of graphite and single layer graphene is presented in fig. 2.10 (a), clearly evident are the G and 2D bands. The lack of a D band is due to the lack of defects or crystalline boundaries present in the samples. The effect of number of graphitic layers on the spectrum is dealt with in section 2.3.3. Fig. 2.10 (b) compares the spectra of graphite and PyC. The small D band present in the graphite spectrum is due to the presence of crystalline boundaries as the spectrum here is for powdered graphite. The PyC displays a spectrum typical of highly defective or nanocrystalline graphitic materials with very broad D and G bands merged together. The heavily suppressed 2D band is indicative of a lack of long range ordering in the sample; suggesting a very small average graphitic crystallite size. The spectral region around the D and G bands is heavily populated with further Raman peaks only present in heavily defective graphitic materials. These are shown in fig. 2.10 (c). In addition to the already mentioned D, D' and G bands are the I peak which is linked with graphitic disorder, sp^2-sp^3 bonds and polyenes;[106,107] and the D" band, which is associated with the presence of amorphous carbon.[108]

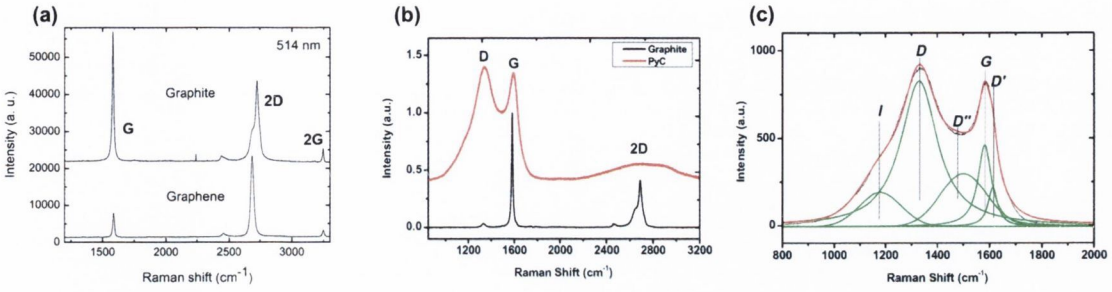

Fig. 2.10. Raman spectra for **(a)** *bulk graphite and monolayer graphene and* **(b)** *graphite powder and PyC.* **(c)** *shows the D and G band region for PyC with various deconvoluted spectral contributions marked.* **(a)** *Reproduced from Ferrari et al.*[109]

2.3.2 *Average Crystallite Size*

Analysis of the intensity ratio of the D and G bands, I_D/I_G, allows the average size of graphitic crystallites, L_a to be measured according to the formula by Tuinstra and Koenig,[101] presented in equation 2.1 below.

$$\frac{I_D}{I_G} = \frac{C(\lambda)}{L_a} \tag{2.1}$$

The term $C(\lambda)$ is dependent on the excitation wavelength of the incident laser. Increasing levels of defects in graphitic samples will cause a broadening of the D and G bands and, thus, it is more accurate to consider the relative integrated area under the D and G bands rather just their relative intensities when calculating L_a. Cancado *et al.* proposed such a formula shown in equation 2.2.[110]

$$\mathrm{L}_a(nm) = \frac{560}{E_t^4}\,\frac{A_D}{A_G} \tag{2.2}$$

E_t is the excitation energy of the incident laser and A_D/A_G is area ratio for the D and G peaks. This formula can be re-written in terms of the wavelength of the excitation laser in nm, λ_t^4; as shown in equation 2.3.

$$\mathrm{L}_a(nm) = (2.4x10^{-10})(\lambda_t^4)\frac{A_D}{A_G} \tag{2.3}$$

Calculation of L_a by analysing the D and G band ratios or areas breaks down as graphitic materials become heavily defective. One feature which must be considered is that as graphitic materials become more defective, the broadening of peaks causes peaks to merge. In particular, the merging of the D' with the G causes an increase in the intensity of the apparent G band peak.[111] If one is to calculate L_a, the different components of the spectrum must be deconvoluted such as in fig. 2.10 (c) in order to accurately measure I_D/I_G or A_D/A_G. Ferrari and Roberston propose their so-called Amorphisation Trajectory for graphitic carbon systems where the position of the G band and I_D/I_G are tracked with respect to defect levels/sp_3 content from graphitic carbon through to Diamond Like Carbon (DLC).[102] As defects are introduced to graphite the material becomes nanocrystalline graphite, (NC-graphite), then amorphous carbon (a-C) and, ultimately, Diamond Like Carbon (DLC). The influence of defects in graphitic carbon can cause the D and G band positions and intensities to change as illustrated in fig. 2.11 (a). The amorphisation trajectory is shown in fig. 2.11 (b), where it can be seen that while I_D/I_G initially increases with increasing defects, after a certain defect level has been reached the ratio starts to drop again.

2.3.3 Influence of Number of Graphene Layers

While Raman spectroscopy allows details about the crystallite sizes and defect distributions in graphitic carbon to be probed, one can also determine information about the number of graphene layers present. This is achieved due to a very specific evolution of the 2D peak.[109] The ratio of the G band to 2D band (I_{2D}/I_G) generally follows predictable behaviour depending on the number of graphene layers present. For monolayer graphene on a substrate of SiO_2, I_{2D}/I_G=3-4. As the number of

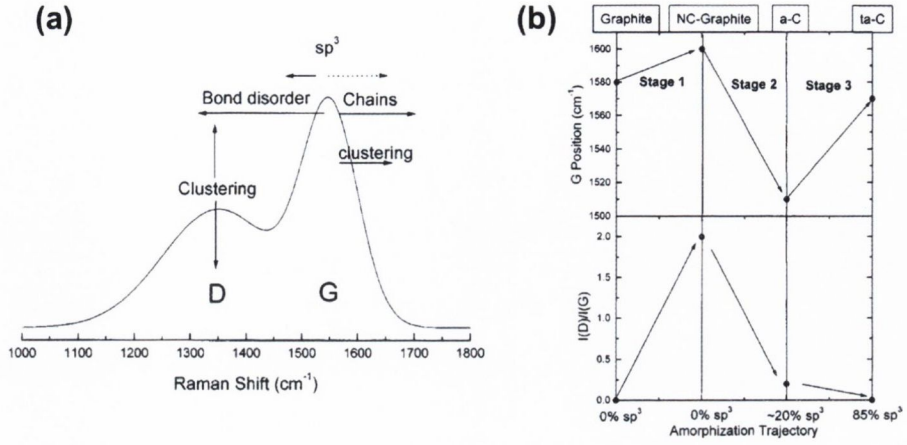

Fig. 2.11. ***(a)*** *Factors influencing the D and G band region of the Raman spectrum for graphitic carbons.* ***(b)*** *Amorphisation Trajectory showing G band position and I_D/I_G from graphitic carbon to DLC. Reproduced from Ferrari and Robertson.* [102]

layers increases, I_{2D}/I_G decreases towards that of bulk graphite; where the 2D band is considerably less intense than the G band. The choice of substrate,among other factors, will influence I_2D/I_G, meaning that this technique is ultimately unsuitable for accurately determining the number of graphene layers. Analysis of the 2D peak profile offers a more accurate method for this.

For single layer graphene, the 2D peak consists of a single sharp Lorentzian peak of FWHM=~26 cm^{-1}. The addition of a second graphene layer modifies the electronic states at the Dirac point. This modification of the electronic structure causes the π and π^* bands to split into four bands. This results in the 2D band splitting into four component peaks, reflecting the four different electron-phonon interactions which can now take place.[105,109] The 2D band for bilayer graphene has a FWHM=~50 cm^{-1} and is upshifted by approximately 20 cm^{-1} compared to monolayer graphene. Addition of more graphene layers modifies the electronic structure further. The spectrum for bulk graphite is observed for upwards of 5 graphene layers. Measured data for the evolution of the 2D band with number of layers for different excitation wavelengths is shown in fig. 2.12 (a) and (b). Fig. 2.12 (c) shows the deconvoluted contributions to the 2D band for two excitation wavelengths in bilayer graphene.

Analysis of the shape of the 2D peak allows one to garner some insight into the number of layers of graphene in a given sample. A good fit of a Lorentzian peak with FWHM=30 cm^{-1} to the 2D band will indicate monolayer graphene. Additional layers will reduce the quality of fit and increase the FWHM. Fig. 2.13 shows data for the Raman spectrum of a mechanically exfoliated flake of graphene. This sample was analysed as part of a study on the mechanical properties of graphene with James

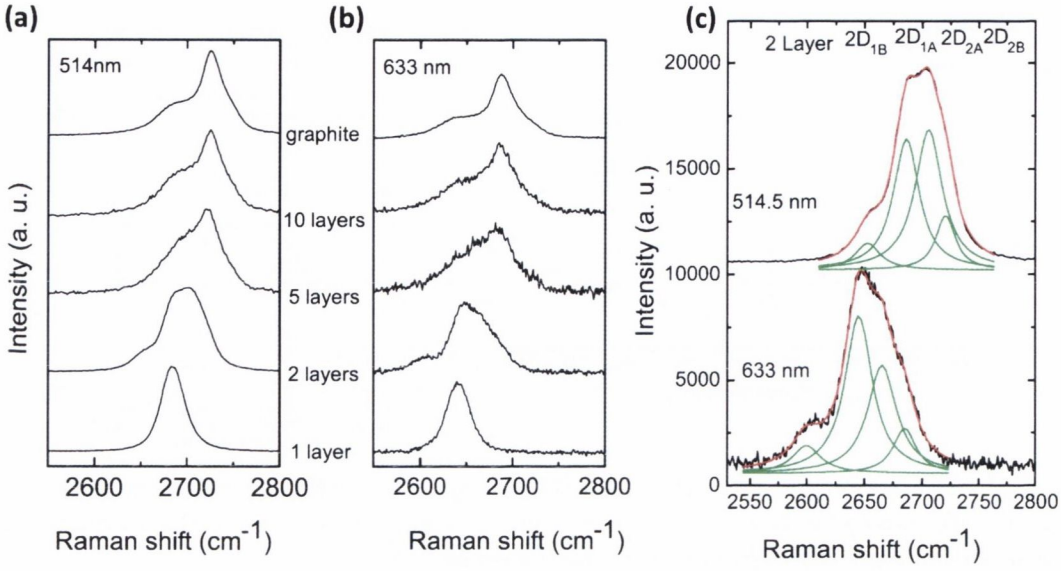

Fig. 2.12. Variation of Raman 2D peak with number of graphitic layers for laser excitation length of ***(a)*** *514 nm and* ***(b)*** *633 nm.* ***(c)*** *Deconvoluted contributions to the 2D peak in bilayer graphene for 514 nm and 633 nm laser excitation. Reproduced from Ferrari et al.* [109]

Annett, who produced the flake. This flake consists of regions of different layer numbers, as seen by the areas of different contrast in the optical microscope image in panel (a). Area 1 corresponds to a monolayer region, area 2 to a bilayer region and area 3 to a few or multilayer region. Scanning Raman spectroscopy which measures multiple spectra over and area was performed; in this case Raman spectra were measured over the area marked by the red box with approximately 10,000 spectra recorded. From this data the average spectrum for each region is shown in panel (b). Panel (c) shows maps representing the intensities of the D, G and 2D peaks, as well as the width of the 2D band as calculated for a fitted single Lorentzian peak. The intensities of the G and 2D bands follow the expected trend for increasing layer number while the D band is only observed at the edge of the regions on the flake. The 2D FWHM also trends as expected with increasing layer number, with the values included with the corresponding spectra in panel (c).

2.4 X-ray Photoelectron Spectroscopy

X-ray Photoelectron Spectroscopy (XPS) is a surface sensitive spectroscopic technique which exploits the photoelectric effect to obtain quantitative chemical information about samples. The photoelectric effect, first reported in 1887[112] by Hertz and finally fully explained in terms of quantum interactions by Einstein in 1905,[113] is the phenomenon whereby photons with sufficient energy incident on a material

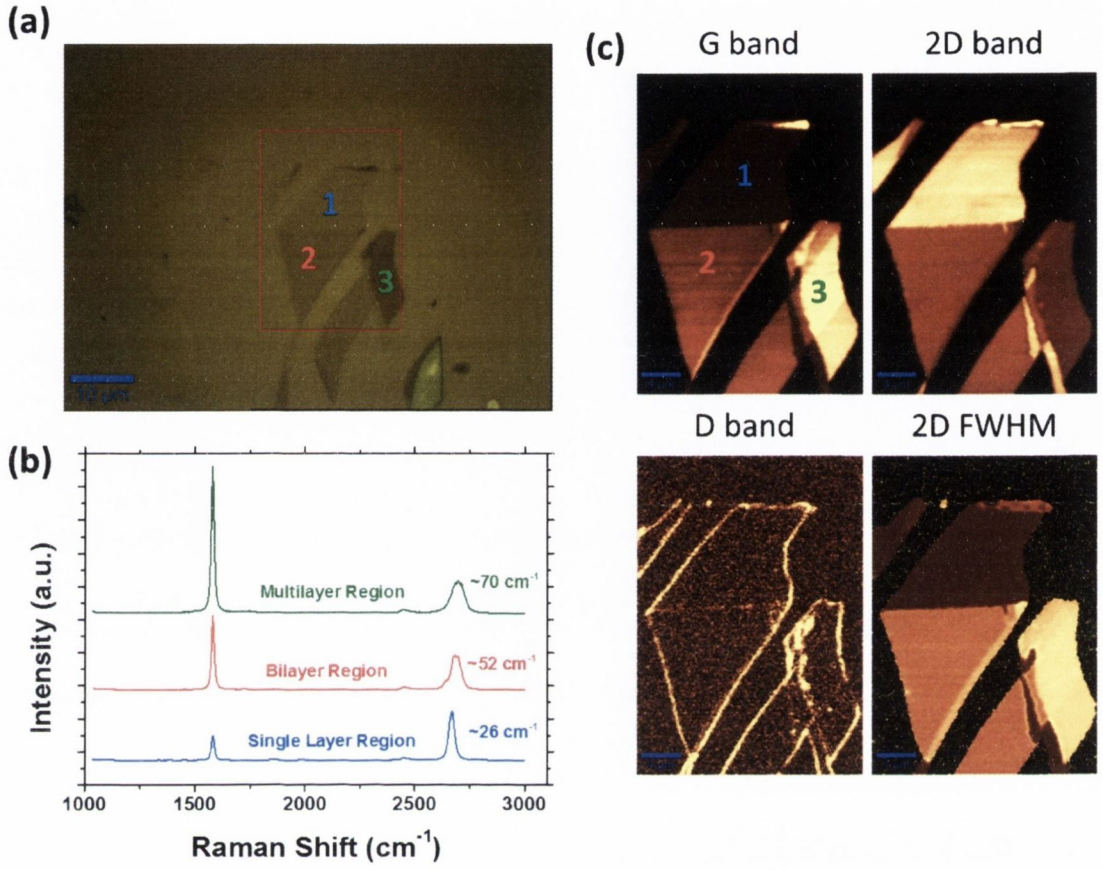

Fig. 2.13. ***(a)*** *Optical image of exfoliated graphene flake showing regions of different number of layers.* ***(b)*** *Raman spectra corresponding to each region, 2D FWHM values are included for each.* ***(c)*** *Intensity profile maps for G, 2D and D bands and 2D FHWM map for a fitted Lorentzian peak.*

causes the emission of electrons from the material. The information in the following section draws from the introductory surface physics textbooks by Prutton[114] and Woodruff and Delchar.[115]

The kinetic energy of the emitted photoelectron, E_K, is described by the following equation.

$$E_K = h\nu - \phi \tag{2.4}$$

$h\nu$ is the energy of the incident photon and ϕ is the work function of the irradiated material, the energy required to remove an electron from the surface of the material. The work function can be further expressed in terms of the binding energy of the electrons, E_B and the Fermi level and vacuum level of the material, E_F and E_{vac}, respectively. Thus, the kinetic energy of the emitted photoelectron can be expressed

as follows.

$$E_K = h\nu - E_B - (E_F - E_{vac}) \tag{2.5}$$

Knowing the energy of the incident photon and then measuring the kinetic energy of the emitted photoelectron allows one to determine the binding energy of the photoelectron prior to it being emitted. This allows one to determine which chemical species are present in the measured sample in a quantifiable manner. Generally speaking, the emission of a photoelectron is modelled as a one-electron system for the sake of simplicity. This allows one to neglect the terms E_F and E_{vac} in the equation and simplify the expression to the following for a simple measurement of E_B of the material being analysed.

$$E_K = h\nu - E_B \tag{2.6}$$

Electrons with an kinetic energy of 200-1500 eV have a mean free path of 10-20 Å, corresponding to a general minimum of the mean free path as a function of electron energy centred about 40 eV. This, essentially, is the sampling depth of the technique; emitted electrons which kinetic energies greater or less than this will not reach the surface to escape the material and, hence, will not be detected. The use of higher energy X-ray (XPS) rather than Ultra Violet (UV) photons (UPS) results in core electrons being ejected rather than valence ones. Fig. 2.14 depicts the processes involved in photoemission due to both UV and X-ray irradiation. As a result of these features, XPS is a surface sensitive technique which probes the core electronic structure. This allows for highly accurate elemental and chemical analysis of surfaces.

XPS data is presented as electron count as a function of binding energy. Peaks occur at specific binding energies corresponding to the electronic structure of the elements present in the measured sample. These are used to identify the species present. The width of these peaks is dependent on many factors, including the geometry of the experimental set-up and ensuring irradiation the sample with monochromatic x-rays. To this end, high resolution systems employ beam monochromators on the incident x-ray beam. Fitting of spectral components to high resolution measured data reveals detailed information about the various chemical species and functional groups present.

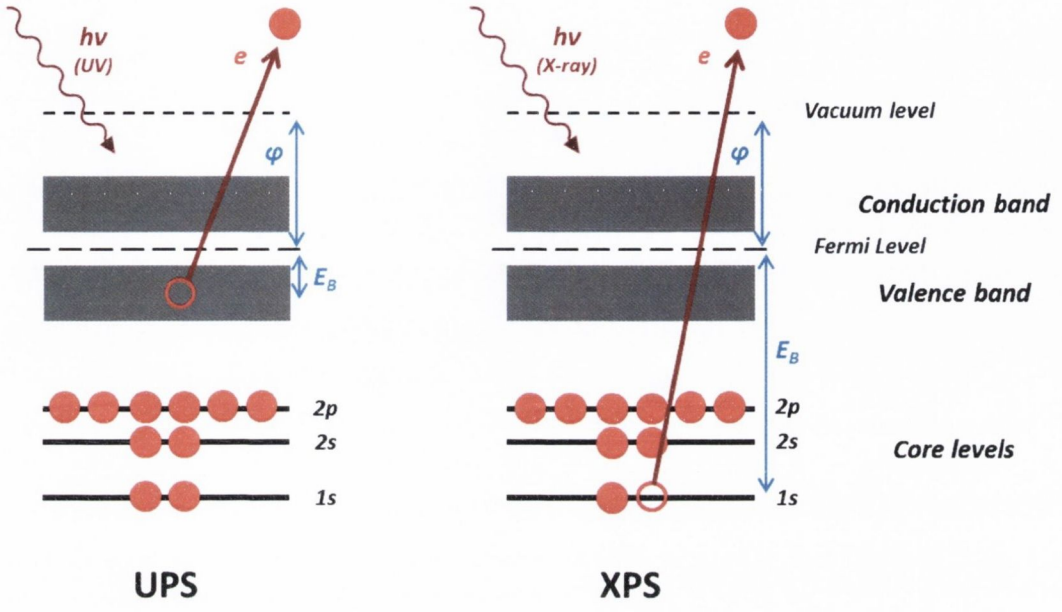

Fig. 2.14. Photoemission process for UV irradiation (UPS) and X-ray irradiation (XPS). ϕ is the work function of the material, E_B is the binding energy of the emitted photoelectron.

An important feature of XPS spectra is the "chemical shift" where a core peak is shifted up or down in energy in correspondence to the addition of chemical bonds. As electrons are added or removed from the atom, the core potential is decreased or increased respectively. This in turn will affect the binding energy of emitted electrons and, hence, the emission energy peak on the spectrum will change. Chemical shift can reveal important information such as the oxidation states of metals by virtue of the magnitude of the observed chemical shift. Emitted electrons may lose their energy through a range of interactions which must be considered so as to interpret the emission spectrum. These include, in order of increasing energy loss; phonon interactions, electron-electron or plasmon interactions, and single or double particle excitations and generation of Auger electrons.

2.5 Electrochemical Techniques

A variety of electrochemical techniques and experimental set-ups were used throughout the experiments in this thesis. These measurements probed the chemistry and catalytic activity of the surfaces studied. Employing the material under investigation as the working electrode in various measurements allowed characterisation of the interface between the electrode and liquid electrolyte. The electrochemical theory explained here is adapted from textbooks by Fisher,[116]

Compton and Banks[117] and the Southampton Electrochemistry Group.[118]

2.5.1 Electrode-Electrolyte Interface

A thorough understanding of the interface between the solid electrode and liquid electrolyte is of crucial importance if electrochemical data is to be accurately interpreted. Several means of segregation of the positive and negative ions in solution at this interface exist. This charge segregation is known as the electrical double layer and the charge distribution and potential fields associated with it are important to understand to fully explain the dynamics at electrode surfaces. Application of an external electrical potential to the electrode directly manipulates the double layer as charged species are attracted or repelled from the surface, depending on the polarity of the applied potential.

Several successive models of the electrical double layer have been developed ranging from the first simple Helmholtz model, the modified Gouy-Chapman model which accounted for diffuse elements, the Stern model which incorporated elements of the previous works, through to Grahame's model which accounted for specifically adsorbed ions. Modifications to and improved understanding of the electrical double layer continue to this day.

2.5.2 Electron Transfer

When redox active species are present in the electrolyte, electron transfer (ET) events take place whereby electrons are exchanged between the electrode and electrolyte species. The chemical reaction that takes place in the electrolyte at the electrode surface can be represented by the following reaction scheme.

$$R \rightleftharpoons O + ne^- \tag{2.7}$$

R and O are the reduced and oxidised form of the redox active species, respectively; while ne^- represents the number, n, of electrons, e^- involved in the reaction. Redox processes, such as the general one outlined above, are driven by an energy difference between the Fermi level of the electrode and the molecular orbitals of the electrolyte species. A dynamic equilibrium is reached whereby the molecular orbitals of the redox active species and the electrode Fermi level are at the same energy and no net charge transfer occurs. Application of an external

potential on the electrode manipulates the Fermi level in the electrode and, so, ET between the redox species and electrode can, in turn, be manipulated. In an electrochemical cell where no reaction direction is favoured and no net current flows through the cell, the potential of the working electrode, E, is given by the Nernst equation.

$$E = E^0 + \frac{RT}{nF} ln \frac{c_O^\infty}{c_R^\infty} \tag{2.8}$$

E^0 is a constant known as the standard cell potential and is a feature of the redox couple in the system. R, T and F represent their usual thermodynamic variables of the universal gas constant, temperature and Faraday's constant, respectively. n is the number of electrons involved in the redox reaction. c_O^∞ and c_R^∞ are the bulk concentrations of the species O and R, respectively.

The influence of the Fermi level on ET behaviour is illustrated in fig. 2.15. In the first scenario shown, no external potential is being applied to the electrode and its Fermi level has reached the same level as the Highest Occupied Molecular Orbital (HOMO) of the redox species; establishing a dynamic equilibrium where ET is not favoured in either direction. Application of a negative potential to the electrode raises the Fermi level, resulting in ET from the electrode to the Lowest Unoccupied Molecular Orbital (LUMO) of the redox probe. Conversely, applying a positive electrode potential lowers the Fermi level and ET occurs from the HOMO of the redox species to the electrode. Scenarios (b) and (c) in fig. 2.15 represent reduction and oxidation of the redox species, respectively.

Electrodes

Throughout this thesis, all materials characterised by electrochemical means are employed as the working electrode. This is the electrode at which electrochemical processes occur and are monitored. The potential is applied between this electrode and the reference electrode. A third electrode, the counter electrode, completes the electrical circuit such that the opposite of any ET processes which occur at the working electrode occur at the counter electrode. The reference electrode is a system with a stable electrochemical potential against which the potential of a complete electrochemical system can be measured. The reference and counter electrode types used in various measurements in this thesis are specified for each section.

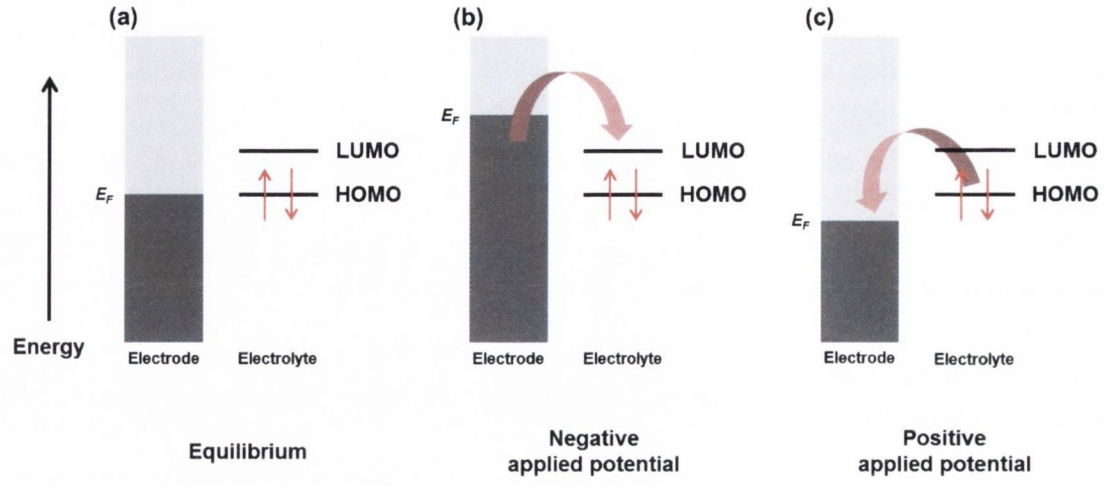

Fig. 2.15. Relationship between electrode Fermi level (E_F) and molecular orbitals of the redox probe in solution in relation to ET behaviour. Scenario ***(a)*** *represents no applied electrode potential with the system at equilibrium,* ***(b)*** *negative applied potential with reduction of redox probe,* ***(c)*** *shows a positive applied potential with oxidation of the redox probe.*

2.5.3 Cyclic Voltammetry

Cyclic Voltammetry (CV) is a dynamic technique which involves sweeping the cell potential linearly from a set-point to another and back again ; the rate of change of potential with time is known as the scan rate, ν. The potential-time profile of a CV measurement with a scan rate of 100 mV s^{-1} is shown in fig. 2.16 (a). The voltammetric data is presented on a voltammogram with the current response presented as a function of applied potential. In redox systems where Faradaic processes occur at the electrode surface, peaks are observed on the resultant cyclic voltammogram which correspond to oxidation and reduction events. For reversible processes (only ideal systems, no real system is totally reversible) the peaks for the oxidative and reductive sweeps on the voltammogram are mirror images of each other. An example of a typical cyclic voltammogram is shown in fig. 2.16 (b), including some standard parameters which are recorded for analysis

The profile of the redox peaks in CV are the result of several processes at the electrode. For the oxidative peak, as the applied potential moves towards E^0, more oxidised species, O, are created at the electrode. The resulting concentration gradient causes mass transport in the electrolyte near the electrode as O diffuses away from the electrode surface and R diffuses towards it. The current flow due to oxidation of R increases as the potential increases. This Faradaic current reaches its maximum at the oxidation peak; at potentials beyond this the diffusion of fresh R to the electrode limits the creation of O. This causes the current to reduce and stabilise at a constant level dictated by the mass transport regime which replenishes

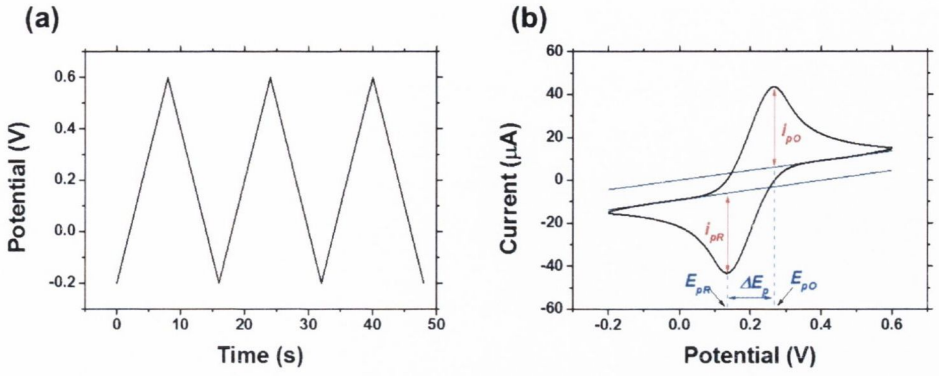

Fig. 2.16. ***(a)*** *Typical potential-time profile for CV showing repeated cycles between potentials of 0.1 and 0.9 V.* ***(b)*** *Typical voltammogram for CV. Peak currents are indicated by red arrows and labelled as i_{pO} (peak oxidative current) and i_{pR} (peak reductive current); corresponding peak potentials are marked by dashed blue lines as labelled E_{pO} (peak oxidative potential) and E_{pR} (peak reductive potential). ΔE_p represents the peak to peak separation, in V, of the two redox peaks.*

analyte at the electrode. The diffusion coefficient, D, of the analyte governs this in the absence of any other factors. Use of stirring systems or rotating disc electrodes increases the mass transport rate significantly so that the ET kinetics are the major limiting factor in redox processes at the electrode. The opposite occurs during the reductive sweep, where fresh O diffuses to the electrode surface. At higher scan rates the species close to the electrode are consumed quickly, resulting in larger peak currents with increasing scan rates.

For simplicity, the diffusion of analyte to the electrode can be considered semi-infinite linear in nature, allowing the peak current of a system to be described by the Randles-Sevcik equation. The following form of the equation (equation 2.9) arises when Fick's second law of diffusion is solved for an ideal system.

$$i_p = 0.4463nFA\sqrt{\frac{nF}{RT}}c^{\infty}\sqrt{D\nu} \tag{2.9}$$

i_p is the peak current, n is the number of electrons involved in the redox process, F is Faraday's constant, A is the electrochemical surface area of the electrode, R is the universal gas constant, T is absolute temperature, c^{∞} is the bulk concentration of the analyte, D is the diffusion coefficient of the analyte and ν is the scan rate.

For diffusion controlled systems a linear relationship should exist between i_p and $\sqrt{\nu}$.[119,120] Faradaic processes for redox active species adsorbed on to the electrode surface exhibit a linear relationship i_p and ν. For ideal single electron processes, the peak separation, ΔE_p, should equal 59 mV and be independent of scan rate.

Realistically this is not the case as perfectly real systems deviate from this ideal. The heterogeneous ET rate constant, k^0, provides a quantitative measure of the rate of charge transfer for Faradaic processes. Its absolute value and physical significance is open to some discussion, but provides a means of comparing the performance of different electrodes. This value can be determined from ΔE_p. Electrodes which display a smaller ΔE_p in a given redox probe exhibit higher values of k^0, signifying more facile ET kinetics than a system with a larger ΔE_p.

2.5.4 Electrochemical Impedance Spectroscopy

Electrochemical Impedance Spectroscopy EIS is a technique where the cell potential is set to a Direct Current (DC) value and small perturbations are applied to this (5 to 10 mV) to generate an Alternating Current (AC). The perturbation frequency is varied over time and the response of the system to this is measured as a function of this frequency. Interpretation of measured EIS data is aided by modelling the electrode/electrolyte interface as a simple electronic circuit with different components of the circuit representing processes that occur at the interface. Such a circuit model is known as a Randles equivalent circuit as proposed by John Edward Brough Randles.[121]

The Randles equivalent circuit for a solid/liquid electrode/electrolyte interface is shown in fig. 2.17 (a). R_{ct} is the resistance to charge transfer, R_s is the solution resistance while C_{dl} represents the double layer capacitance arising from the electrical double layer at the electrode/electrolyte interface. The final component of the circuit is the Warburg impedance which arises due to diffusion of analyte to the electrode. At higher frequencies the Warburg impedance is small as reactants do not need to diffuse far whereas in the low frequency domain reactants diffuse further; thereby increasing the contribution of the Warburg impedance. It should be noted that in all the EIS measurements in the experiments which follow in later chapters, that all charge transfer processes involve ET.

Presentation and subsequent interpretation of the EIS data is carried out on a Nyquist plot. A Nyquist plot typical of the systems studied in this thesis is presented in fig. 2.17 (b) with the various features marked. Impedance is the AC equivalent of resistance and, as such, can be expressed as a complex number. Consequently, impedance may be plotted on a complex plane with the real component, Z', appearing on the x-axis and the imaginary component, Z'', appearing on the y-axis. The high frequency portion of the plot (towards the origin) displays a semi-circular shape which is characteristic of a kinetics controlled system. Here the impedance is dominated by double layer charging and charge transfer processes. In the low

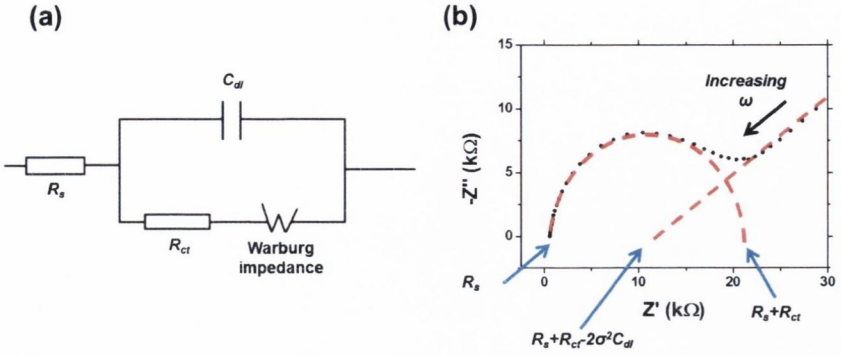

Fig. 2.17. ***(a)*** *Randles equivalent circuit for the electrode/electrolyte interface.* ***(b)*** *Typical Nyquist plot showing semi-circular kinetic controlled region and linear diffusion controlled region. R_s is solution resistance, R_{ct} is resistance to charge transfer, C_{dl} is the double layer capacitance. ω represents the frequency of the applied AC perturbation.*

frequency region diffusion is the controlling factor and a linear relationship is observed between the real and imaginary components of the impedance. The diameter of the semi-circular region of the Nyquist plot is equal in magnitude to R_{ct}. Thus, an easy measure of this value can be carried out by analysing Nyquist plots which allows for a quantitative comparison between the ET kinetics of redox systems.

2.5.5 *Tafel Analysis*

Electrochemical analysis of HER catalysts in chapter 7 involves Tafel analysis of voltammetric data. The Butler-Volmer equation describes the current, I, as a function of overpotential, η, in dynamic electrochemical systems of the general reaction described in equation 2.10. Solving the Butler-Volmer equation for general cases where the applied potential is far away from the formal potential for the system in question results in regions of linear relationships between η and $\ln|I|$, which are themselves described by the Tafel equation, which is expressed below.

$$\eta = b log j + a \tag{2.10}$$

Here η is the applied overpotential, b is the Tafel slope, j is the current density and a captures several thermodynamic constants. The slope of the linear portion of a Tafel plot gives information about the transfer coefficients of a given reaction and, hence, reveals details regarding the kinetics of the reaction. Tafel analysis in this

thesis was carried by performing Linear Sweep Voltammetry (LSV) and plotting the resultant voltammetric data as η versus $\ln|I|$. LSV is essentially the same technique as CV, but the potential is simply scanned from one value to another once as opposed to the cyclically as in CV. Fitting a straight line to the linear portion of the resultant plot revealed information about the reaction mechanism at different electrodes.

Progress of the HER in acidic media involves an initial step whereby a proton in solution is reduced electrochemically followed by adsorption of an intermediate, H_{ads}, to the electrode surface as follows.

$$H_3O^+ + e^- \rightarrow H_{ads} + H_2O \tag{2.11}$$

This is known as the Volmer reaction and is associated with a Tafel slope of 120 mV decade^{-1}. This is followed by desorption of H_2 *via* either of the following reactions.

$$H_{ads} + H_3O^+ + e^- \rightarrow H_2 + H_2O \tag{2.12}$$

or

$$H_{ads} + H_{ads} \rightarrow H_2 \tag{2.13}$$

The reaction given in equation 2.12 is known as the Heyrovsky reaction, with that in equation 2.13 known as the Tafel reaction. The Tafel reaction exhibits a Tafel slope of approximately 30 mV decade^{-1}. In cases of low coverage of H_{ads}, the Heyrovsky reaction has a slope of about 120 mV decade^{-1}; in cases of higher H_{ads} coverage this reduces to 40 mV decade^{-1}. The change in the Tafel slope here is caused by different mechanisms dominating at different values of H_{ads}. Simply considering the observed Tafel slope for different HER electrocatalysts gives one an insight in to the dominant reaction mechanism at the electrode. HER at Pt electrodes is known to

proceed *via* the Volmer-Tafel mechanism with a Tafel slope of 30 mV decade^{-1}. As Pt represents the material with the best performance as catalyst for the HER, alternative electrocatalysts should exhibit a Tafel slope equal or as close to this as possible. The extremely high surface coverage of H_{ads} on Pt electrodes is a central reason for the excellent HER catalysis on this material.

2.6 Electron Microscopy

Electron microscopy was widely employed throughout this thesis to image and characterise the surfaces of the various materials studied.

2.6.1 Scanning Electron Microscopy

Scanning Electron Microscopy (SEM) was extensively used, particularly for studies of continuous films. Electron microscopy allows much higher imaging resolution be achieved than is possible with optical techniques. The de Broglie wavelength of electrons is considerably shorter than for short wavelength visible light and, thus, allows for resolution many orders of magnitude greater.[122] In brief, a beam of electrons is emitted from an electron source, accelerated using high voltages and focused on a sample through the use of magnetic lenses. This beam is scattered by the electron clouds and nuclei of atoms present in the sample and scattered electrons may be detected. In SEM, the electron beam is scanned, or rastered, back and forth across the sample surface to generate an image of the surface. Depending on the interaction between the electron beam and the sample, different types of scattered electrons can be detected and different characteristic information about the sample determined. Typically backscattered and secondary electrons are used to generate images. Detection of Auger electrons and characteristic X-rays can also be used to determine structural and chemical details.

2.6.2 Transmission Electron Microscopy

Transmission Electron Microscopy (TEM) involves passing a high energy electron beam through an atomically thin sample and detecting the transmitted electrons to generate an image of the material. As electrons pass through the thin sample, interactions with the nuclei and electron clouds of the sample atoms cause the transmitted electrons to be scattered. The interference patterns that result from these scattered electrons can be used to image the atomic structure of the sample. High Resolution TEM (HRTEM) involves passing a broad parallel electron beam through the sample and generating an image from many overlapping signals.

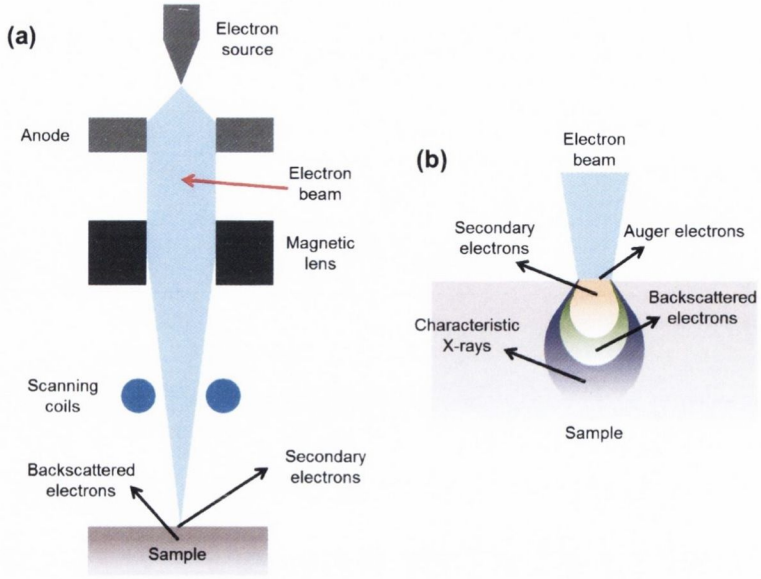

Fig. 2.18. (a) Schematic of a typical SEM apparatus. (b) Various emissions upon interaction of the electron beam with the sample.

Scanning TEM (STEM) requires that the electron beam be focussed to a sharp point at the sample. This is then scanned across the sample surface to generate an image of the sample. Both imaging techniques were employed in the characterisation of various materials in this thesis.

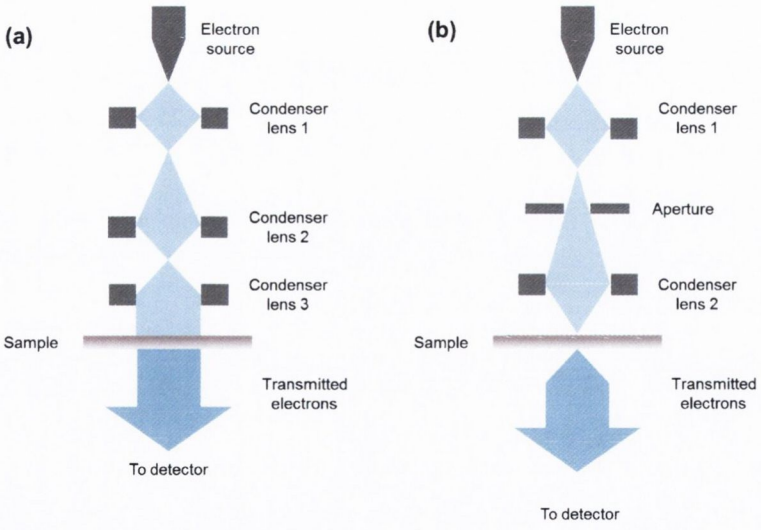

Fig. 2.19. Schematic of a typical TEM in (a) parallel beam and (b) convergent beam modes.

2.7 Miscellaneous Surface Characterisation Techniques

2.7.1 Atomic Force Microscopy

Atomic Force Microscopy (AFM) is a variant of scanning probe microscopy whereby a physical probe scans across the surface of a sample and topographical information about the surface is gathered. In AFM a very fine tip on the end of a cantilever is rastered across the sample and piezoelectric motors allow minute changes in the position of the tip to be completed. The tip and sample surface interact through a variety of forces such as van der Waals, capillary, electrostatic, chemical bonding and mechanical contact forces; which gives rise to a deflection of the cantilever. The AFM tip may be dragged gently across the surface in contact mode or used in a non-contact tapping mode.

In tapping mode the cantilever is driven at an oscillation just above or below its resonant frequency and long range forces which extend beyond the sample surface interact with the tip and dampen the cantilever oscillation. The oscillation frequency is maintained by moving the tip closer to or further away from the surface (z-position) by means of piezoelectric motors. The z-position of the tip is correlated with the x-y plane in which the scan took place and a topographical map of the surface may be generated. The deflection of the AFM tip is measured by reflecting a diode laser on to the back of the cantilever where it is reflected on to a photodiode array. As the cantilever oscillates the position of the reflected laser beam on the diode array changes and is monitored by the controlling system. Fig. 2.20 shows a simple schematic of an AFM system in tapping mode.

2.7.2 Contact Angle

This very simple technique gives valuable insight into the nature of the surface chemistry of samples. A drop of liquid placed on a smooth solid surface will form a particular shape dependent on the wettability of the surface for a given liquid. The shape of the droplet is reflected in the contact angle with the surface, as shown in fig. 2.21. This contact angle is a product of the liquid surface tension and the interfacial tension at the solid/liquid interface, which arises from various intermolecular forces such as van der Walls, hydrogen bonding, polar interactions etc. The use of different liquids which are known to exhibit certain of these forces can give an indication of the nature of the interaction between the two materials at the interface. Highly polar liquids, such as water, exhibit a very clear distinction between hydrophobic and hydrophilic materials by virtue of the contact angle. A pure carbon surface, for example, shows typical hydrophobic character whereas a

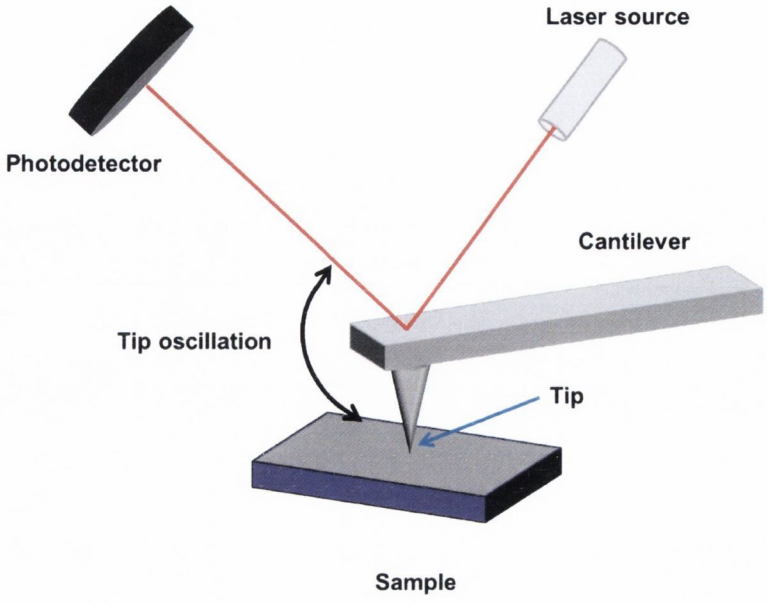

Fig. 2.20. Schematic of a typical AFM apparatus in tapping mode.

functionalised surface will bear electrostatic dipoles with which water molecules can create hydrogen and polar bonds; creating a hydrophilic surface.

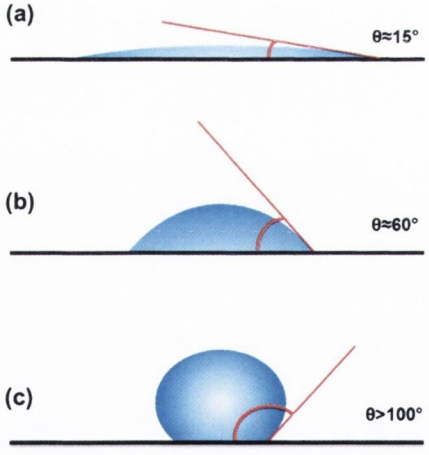

Fig. 2.21. Diagram showing the behaviour of water droplets on various surfaces. (a) Hydrophilic surface, excellent wetting; (b) typical surface showing less wetting of the surface; (c) hydrophobic surface, poor wetting of the surface

Chapter 3

Experimental Techniques

This chapter details the specifics of the various techniques and instruments used throughout this thesis. The theory and explanation behind various techniques is dealt with in chapter 2.

3.1 General Materials

All chemicals were purchased from Sigma-Aldrich and used as-received. Any aqueous solutions were made using purified water (18 MΩ) from a Barnstead Nanopure system. All SiO_2 substrate wafers were purchased from Si-Mat and Dasom RMS and consisted of 300 nm dry thermal oxide on Si(100). Acetylene (98.5%), methane (98%), oxygen (99%), ammonia (99.98%) and argon (99.99%) gases were supplied by BOC Gases. Nitrogen and hydrogen gas were generated on-site using DALCO N_2 and Schmidlin PG-250 H_2 generators, respectively. Cu foils (25.5 μm, 99.99%) were purchased from Gould GmbH and Ni foils (25 μm, 99.99%) were purchased from Advent Research Materials Ltd.

3.2 Deposition Tools

3.2.1 CVD systems

PyC was grown using a hot wall quartz tube furnace manufactured by Gero GmbH with a tube diameter of 10 cm. Acetylene (C_2H_2) was passed over SiO_2 wafers at a temperature of 950° C at a flow rate of approximately 180 sccm. Growth was carried out at a pressure of 20 torr for 30 minutes, yielding a PyC film of approximately 400 nm in thickness. The effect of the various growth parameters is discussed in detail by McEvoy *et al.*[123] Films were cooled to room temperature under Ar flow. Gas flow rates were set using mechanical needle valves and the chamber pressure

was regulated with an angle valve from MKS connected to the pressure sensor.

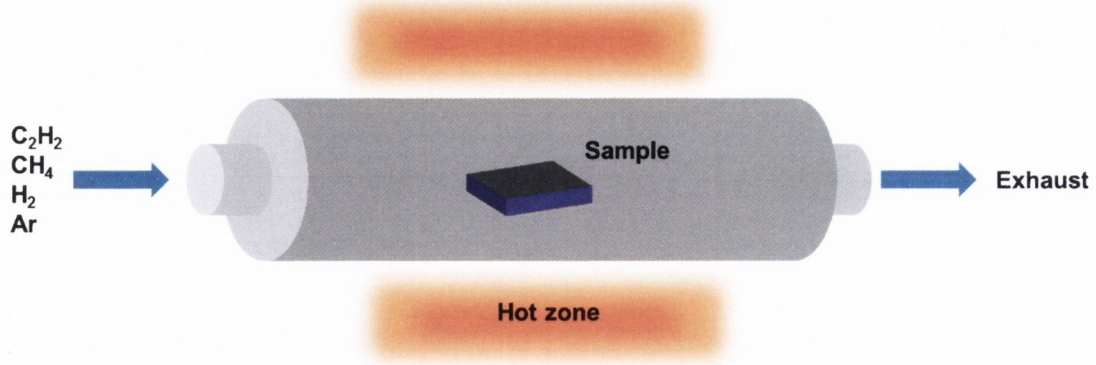

Fig. 3.1. Typical set-up of the both the Gero and Carbolite CVD furnace systems used for growth of various carbon films.

Monolayer graphene was grown in a Carbolite hot wall quartz tube furnace with a 38 mm diameter tube. Cu foils were immersed in dilute acetic acid and rinsed with water to remove surface oxides. The foils were then introduced to the furnace at room temperature and ramped to 1035° C under H_2 flow (80 sccm, pressure ~0.2 Torr). The Cu was annealed at this temperature for 20 minutes to remove any oxides and increase the Cu grain size. Graphene growth was performed by flowing mixture of CH_4 (10 sccm) and H_2 (2.5 sccm) for 20 minutes at a pressure of 0.07 Torr, after which the CH_4 flow was switched off and the samples cooled to room temperature under H_2 flow. Gas flow was regulated with electronic Mass Flow Controllers (MFCs) while a butterfly valve controlled the exhaust pumping rate. Growth of monolayer graphene within the research group was previously reported by Kumar *et al.*[91]

Few layer graphene was grown in the Gero furnace system on Ni foils. The foils were rinsed in dilute acetic acid and rinsed with water prior to loading into the furnace at room temperature. The furnace was ramped to 850° C under H_2 flow (20 sccm, 1.5 torr) and annealed at this temperature for 30 minutes. Growth was carried out with a gas flow mixture of H_2 flow (20 sccm) and C_2H_2 (60 sccm) for just 2 minutes. The chamber pressure was maintained at 1.5 torr during growth. Samples were then cooled to room temperature under Ar flow before removal. Fig. 3.1 shows the basic set-up for both the Gero and Carbolite CVD systems.

3.2.2 Sythesis of TMD films

Metal Deposition

Controlled deposition of metal films on SiO_2 and PyC was achieved with a Temescal FC-2000 electron beam evaporation system. This system boasts a throw distance of about 1 metre, ensuring a normal uniform flux of material on the wafer. Nominal thickness of the metal films was monitored with a Quartz Crystal Microbalance (QCM) and later accurately measured using Spectroscopic Ellipsometry (see below). A deposition rate of approximately 1 Å s^{-1} was maintained.

Vapour Phase Sulfurisation

Mo films on both PyC and SiO_2 substrates were converted to MoS_2 using a widely reported technique. PyC substrates such as those discussed in chapter 4 were used to grow the MoS_2/PyC hybrid electrodes reported in chapter 7, while MoS_2 films grown directly in SiO_2 were used to measure film thicknesses. Mo samples were placed in a two-zone hot wall quartz tube furnace (tube diameter of 35 mm) and heated to 750° C under Ar flow (150 sccm). Sulfur powder was thermally sublimed upstream of the samples at a temperature of 120° C and sulfurisation of the Mo took place in the higher temperature region under S vapour. Samples were then cooled to room temperature under Ar flow for removal. The set-up for this furnace system is illustrated in fig. 3.2. The high temperature region was achieved with a Lindberg furnace system, while the lower temperature hot zone was controlled by a home-made radial heating system which used tungsten filament light bulbs.

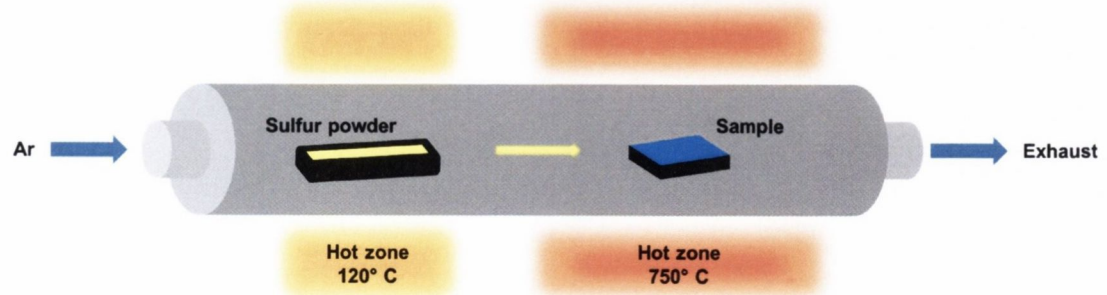

Fig. 3.2. Illustration of the two-zone furnace system used for vapour phase sulfurisation of metallic Mo films. Sulfur is thermally sublimed upstream of the Mo film, which is sulfurised in the higher temperature zone.

3.3 Graphene Transfer

In order to carry out measurements and further processing of graphene, it is necessary to transfer graphene from the metal growth substrate to insulating substrates. To this end, a widely used technique was employed whereby a polymer intermediate support layer is used. Poly(methyl methacrylate) (PMMA) was spin-coated on to the graphene side of a graphene/Cu foil after growth. This film was then placed on the surface of a solution of ammonium persulfate (APS) etchant, floating Cu face down, to etch the Cu foil. After removal of Cu, the resulting PMMA/graphene film was fished from the APS with a glass slide and transferred to water. This was repeated in order to completely remove any traces of etchant. The desired final substrate was used to fish the film from the water and allowed to dry under reduced pressure in a desiccator. Finally, the PMMA support layer was dissolved using HPLC acetone and rinsed with IPA. The process flow is illustrated in fig 3.3. This process was not required for few layered graphene samples as these films were sufficiently mechanically robust to withstand the handling involved without a PMMA support layer.

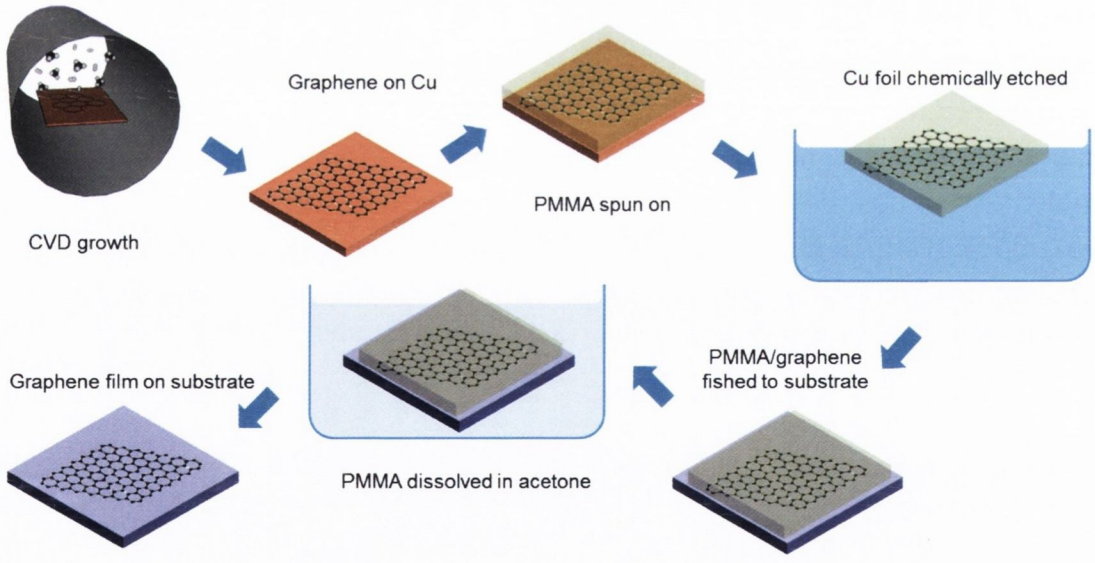

Fig. 3.3. Schematic of the graphene transfer process whereby PMMA is used to transfer graphene to arbitrary substrates.

3.4 Plasma Treatments

All plasma treatments presented in this thesis were performed using a R^3T TWR-2000T microwave radical generator (2.45 GHz) connected to a low pressure downstream plasma configuration assembly such that plasma was ignited a short

distance (~15 cm) away from the sample to be treated. Gas flow through the system ensured that plasma radicals interacted with the samples in a manner where the radicals and ions were kinetically relaxed upon interaction with the sample. Minimal kinetic damage due to collisions between accelerated species took place.

Gas flows of 100 sccm, controlled by MFCs, were used at a plasma power of 1 kW. The chamber pressure was maintained at 1 torr at a given gas flow rate by means of a manual variable exhaust valve. Two plasma types were used as follows. O_2 plasma treatments were carried out at a flow rate of 100 sccm pure O_2 while NH_3 treatments consisted of a gas mixture of NH_3 and H_2 with a flow rate of 50 sccm each. Throughout this thesis, all references to NH_3 plasma treatments imply this NH_3/H_2 gas mixture. The exposure times for various experiments are specified in each chapter. Fig. 3.4 shows a schematic of the system used for all plasma treatments.

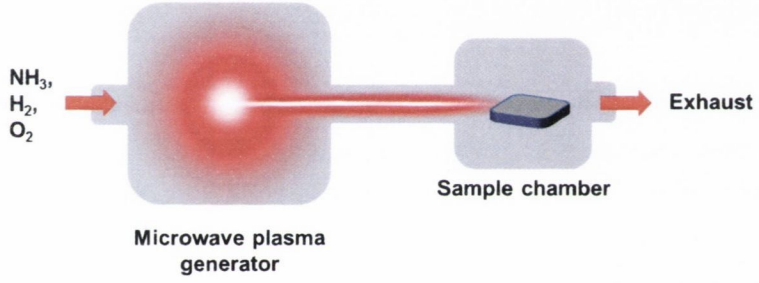

Fig. 3.4. Schematic of the plasma treatment chamber used throughout the experiments in this thesis.

For graphene films grown via CVD on metal foils, plasma treatments were carried out both directly on the growth substrate or after transfer to SiO_2 substrates. The characterisation method to be employed dictated whether the graphene film was transferred or left on the growth substrate for the plasma exposure. XPS is more easily performed when samples are conductive, so films were left on the growth foils for this analysis technique.

3.5 Raman Spectroscopy

Raman spectroscopic measurements were carried out with a Witec alpha 300 R confocal Raman spectroscopy microscope. A 532 nm diode laser was used to irradiate samples. For the carbon materials in chapters 4-6 an approximate 20 mW laser power was used. In chapter 7, a laser power of 0.5 mW was necessary to ensure no burning of the sample or any influence of sample heating in the spectral response. The majority of measurements were recorded with a spectrometer

grating of 600 lines mm^{-1} but high spectral resolution scans required the use of a 1800 lines mm^{-1} grating.

Scanning Raman spectroscopy involved piezoelectric motors scanning the sample stage in the x and y directions and measuring multiple discrete spectra across the surface. An effective spatial resolution of approximately 300 nm is achieved in this mode, according to the manufacturers. Typically, regions of a sample measuring 30x30 μm were scanned measured with 120x120 spectra.

3.6 XPS

Two XPS systems were used to acquire the spectra presented in this thesis. For functionalised carbon materials in chapters 4-6, XPS data was recorded using an Omicron ESCA system with a EA 125 analyser and XM1000MK II monochromated Al Kα X-ray source (1486.7 eV). Samples were irradiated with a spot size of roughly 2 mm, meaning that all XPS data is representative of large areas of the sample surface. For survey scans an analyser pass energy of 50 eV was used. High resolution scans of specific core level peaks were measured with a pass energy of 20 eV, resulting in a spectral resolution of approximately 0.55 eV for the instrument.

Measurements of MoS_2/PyC hybrid electrodes in chapter 7 were carried out using a VG Scientific ESCAlab MKII system. Although this used the same X-ray source as in the other system, the emitted X-rays were not monochromated; resulting in a slightly wider energy dispersion in the X-rays incident on the samples. The net result was a slightly lower spectral resolution than could be achieved on the Omicron system. The same pass energy settings were used as on the previous system.

During data analysis, fitting of spectral contributions to high resolution core level peaks was performed. For fitting of the C 1s level all contributions were fitted as individual Gaussian peaks over a Shirley background function using CASA XPS software. Fitting of S 2p and Mo 3d levels in chapter 7 was performed using Unifit software. A series of doublet peaks with Gaussian and Lorentzian character were fitted following the subtraction of a Shirley background function.

3.7 Electrochemical Measurements

All electrochemical characterisation was performed using a Gamry Reference 600 potentiostat with a three electrode cell configuration. Characterisation of carbon materials in chapters 4-6 was performed by employing the material in question as the working electrode with a Pt wire counter electrode and Ag/AgCl reference electrode. For characterisation of MoS_2/PyC hybrid electrodes in chapter 7, a graphite counter

electrode and a Reference Hydrogen Electrode (RHE) were used.

PyC was employed as the working electrode by encasing it in a custom-built holder which exposed a circular region of the sample (1 mm radius) to the electrolyte. Graphene films were investigated using a plate material cell from ALS, Japan, which exposed a 0.45 cm^2 region of the film to the electrolyte. For monolayer graphene, Au was sputter-coated on to the periphery of the graphene film and contacted with a mechanical crocodile clip. Few layer graphene films were contacted directly using a crocodile clip as these films had enough mechanical robustness to withstand such crude contacting techniques.

For ORR measurements in chapter 6, N-rGO material was deposited on a GC electrode and used with a Modulated Speed Rotating Electrode from Pine Instruments in conjunction with an Autolab N-series potentiostat.

3.8 Electron Microscopy

3.8.1 Scanning Electron Microscopy

SEM images were taken using a Zeiss Ultra field emission SEM with low accelerating voltages (1-5 kV) in order to ensure that the surface of all studied materials was imaged. Both in-lens and secondary electron detectors were used. The relevant details accompany any SEM images presented.

3.8.2 Transmission Electron Microscopy

TEM imaging was done using an FEI Titan TEM at an accelerating voltage of 300 kV. Cross-sections of MoS_2/PyC films were fabricated by Focussed Ion Beam (FIB) milling using Ga ions and mounted on viewing grids for imaging. Top-down TEM imaging os MoS_2 was completed by transferring the films on to Cu TEM support grids using PMMA assisted transfer.

3.9 Miscellaneous Techniques

3.9.1 Atomic Force Microscopy

AFM was performed using an Asylum MFP-3D AFM in tapping mode with Si tips with a tip radius of 50 nm and a resonant frequency of 300 Hz.

Profilometry

This technique is analogous to AFM in that a physical probe measures surface morphology but only along a linescan and with lower sensitivity. A Dektak 6M profilometer by Veeco Instruments was used for this.

3.9.2 Contact Angle

The contact angle was measured by dropping a small amount of water (a few /*mu*l) on to a sample and photographing the droplet side-on. The opensource image processing software, ImageJ, was used to measure the contact angle using the "dropsnake" measurement package.

3.9.3 Spectroscopic Ellipsometry

Thicknesses of Mo and MoS_2 films were accurately measured by Spectroscopic Ellipsometry (SE) performed using an Alpha SE tool from J.A. Woollam Co., Inc. operating in the wavelength range of 380-900 nm at an angle of incidence of 70°. Measurements were performed on films grown on SiO_2 which were deposited in the same deposition runs as those films deposited on PyC in order to accurately gauge the thickness of the hybrid electrodes.

Chapter 4

Plasma Treated Pyrolytic Carbon

4.1 Introduction

There exists in the literature a wealth of information regarding electrochemistry at carbon electrodes. Features such as the wide potential window, chemical, mechanical and thermal stability and good electrical conductivity make graphitic carbon materials particularly suited to many electrochemical applications. In particular, nanostructured carbon materials such as fullerenes, CNTs and graphene have enjoyed a huge interest within the research community in the last 15-20 years and these materials have been incorporated into many electrochemical applications. While the attraction of these more exotic and novel nanocarbons has seen them dominate research into carbon electrochemistry, other nanostructured graphitic materials such Pyrolised Photoresist Films (PPF) have been widely investigated. PPF is structurally similar to PyC but is formed *via* the pyrolysis of polymer films *in situ* on substrate surfaces. Typically, photoresist polymers are spin-coated on a substrate and annealed to leave a nanocrystalline graphitic film. Unlike PyC, which consists of many randomly oriented crystallites, PPF typically consists of interwoven graphitic ribbons which result from the interwoven polymer in the photoresist film prior to pyrolysis. In this sense, PPF can be considered analogous to glassy carbon. The ease of preparation of this material has seen extensive work carried out on PPF electrodes.[124][125][126] Details regarding the formation of PPF are discussed by Schreiber et al.[127] Given the extensive body of knowledge that exists within the literature regarding PPF, it is easy to relate the electrochemical performance of PyC to this. Interpretation of surface chemistry and influences on redox process at the electrode as understood in studies on PPF are applicable for PyC.

Despite its properties such as electrical conductivity, chemical stability and wide potential window being well suited to electrochemical processes, PyC exhibits rather sluggish ET behaviour, limiting its use in certain areas of electrochemical

sensing. In spite of this, there are several reports of the successful implementation of PyC, or similar turbostratic graphitic materials, in electrochemical applications including the use of PyC electrodes for detection of trace metals by Hadi et al.[128] Elsewhere, Modified PyC has been utilised as an electrode material *via* the *in situ* CVD of nitrogen and boron doped PyC on porous substrates with appropriate heteroatom precursors.[129] Furthermore, porous N-doped PyC-like material has been synthesised *via* the pyrolysis of nitrogen-bearing organic compounds on mesoporous templates and successfully employed as an electrode material for the ORR (see chapter 6 for more details on this reaction).[130]

It is noteworthy that in many of the studies which successfully utilised PyC in electrochemical applications, the presence of heteroatoms or dopants in the PyC was necessary. The genesis of the following work on functionalised PyC lies in the work by Dr. Gareth Keeley which found that functionalisation of PyC with oxygen plasma drastically improved the ET kinetics of the material.[131]

4.2 Plasma Treatment

Plasma treatment of PyC films was carried out as described in chapter 3. Both O_2 and NH_3 plasma treatments were investigated. The majority of the results presented in this chapter are for PyC films which have been exposed to just O_2 or NH_3 treatments. However, some results are presented which show the effects of a two-step plasma treatment whereby samples were exposed to O_2 plasma and then a subsequent NH_3 plasma.

4.3 Physical Characterisation

4.3.1 Electron Microscopy

Changes in the surface morphology of the PyC films after plasma treatment were first investigated using SEM. Low accelerating voltages and the in-lens detector were employed to ensure that the generated image was mostly due to the surface of the films. It was found that the surface porosity of the as-grown PyC increases visibly after all plasma treatments. This is seen in fig. 4.1 where it appears that the NH_3 plasma treatment causes the largest increase in the surface porosity.

4.3.2 Atomic Force Microscopy

AFM was performed on all PyC films to gain a quantitative insight into the changes in surface morphology after plasma treatment. Scans areas of 10x10 μm were analysed

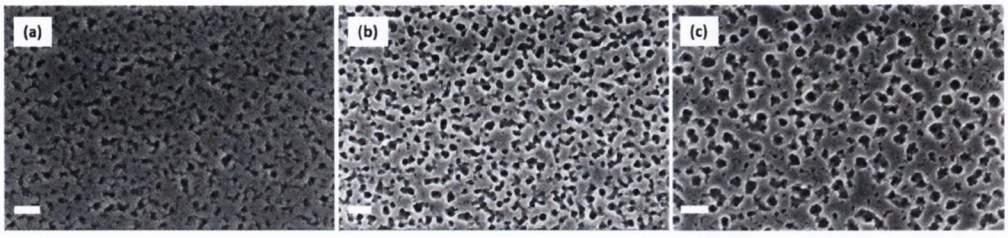

Fig. 4.1. SEM images of **(a)** *as-grown,* **(b)** O_2 *and* **(c)** NH_3 *treated PyC films. Scale bar is 200 nm in each case. Images obtained with 2 kV accelerating voltage and in-lens detector.*

Table 4.1. RMS roughness values for as-grown PyC and plasma treated PyC.

Sample	As-grown	O_2	NH_3
RMS roughness (nm)	0.5	0.89	3.8

and the RMS roughness was calculated over this scanned area of each sample. Fig. 4.2 shows AFM images for as-grown PyC and the various plasma treated PyC films.

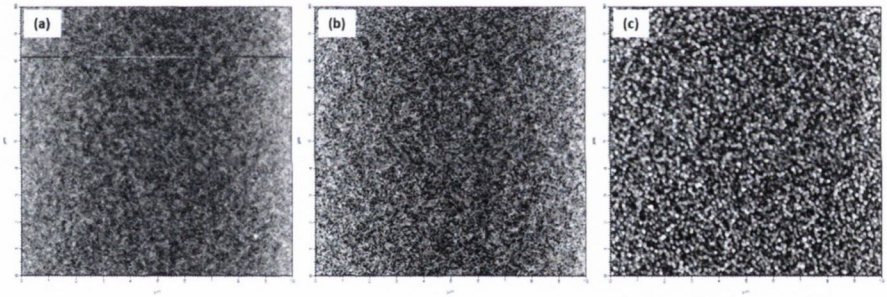

Fig. 4.2. AFM images for **(a)** *as-grown,* **(b)** O_2 *treated and* **(c)** NH_3 *treated PyC. Scan areas measure 10x10 μm.*

It was found that all plasma treatments increase the PyC film roughness, with the roughness values shown in 4.1. Despite the fact that O_2 plasma is very reactive with carbon materials, the NH_3 plasma treated films exhibited a RMS roughness of greater magnitude than that of the O_2.

4.3.3 Plasma Etch Rates

It is known that O_2 plasma reactively etches carbon materials. Indeed, ashing samples in this manner is routinely used to remove residual photo-resist during lithographic patterning of samples. The etch rates of the O_2 and NH_3 plasma treatments were investigated by scratching the surface of a PyC sample with a scalpel to make a scratch down to the SiO_2 substrate and measuring the depth of the scratch by profilometry. The scratch depth was measured on several sites and the averages are presented

below in fig. 4.3. The thickness measurements presented here are averaged across several sites on the scratch with the linear fit representing the etch rate.

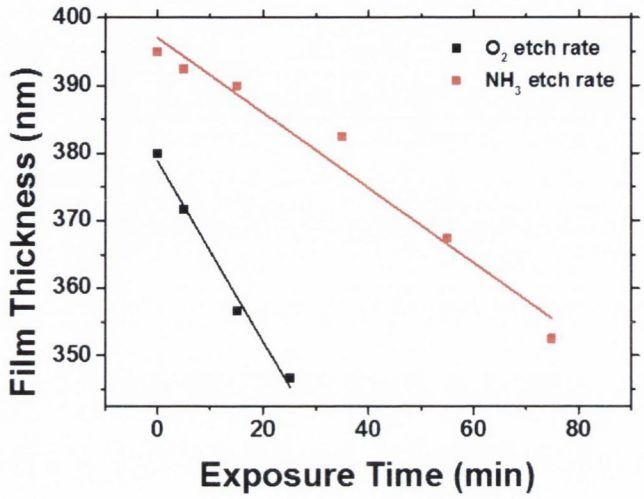

Fig. 4.3. Etch rates of O_2 (black) and NH_3 (red) plasma on PyC. Data sets averaged over several sites.

It was found that the O_2 plasma exhibits an etch rate of approximately 1.34 nm s^{-1}, while the NH_3 plasma etches the PyC at a rate of approximately 0.55 nm s^{-1}. These relative values make sense as oxygen radicals are known to be more reactive with carbon materials than nitrogen radicals.

4.3.4 Raman Spectroscopy

Raman spectroscopy is an excellent tool for characterising the crystalline properties of graphitic systems owing to the very strong Raman peaks which such systems exhibit. As-grown and plasma treated PyC films were analysed using Raman spectroscopy with the resultant spectra shown below in fig. 4.4. It is clear that there is no appreciable difference between the samples with all displaying a broad and poorly defined D band region of similar intensity to the G band with the 2D peak heavily suppressed. This is typical of heavily disordered graphitic systems, such as PyC, where the suppression of the 2D band is related to a lack of spatial uniformity. In addition to the three main spectral contributions, other peaks arise due to the defective nature of PyC. These are the *D'* , *I* and *D"* bands. The *D'* band was previously discussed in chapter 2 and arises due to defects in graphitic systems.[105] The *I* band is related to graphitic disorder, sp^2-sp^3 bonds and the presence of polyenes.[106,107] The *D"* is suspected to be related to amorphous carbon.[108]

The presence of sp^3 bonds and amorphous carbon are expected for such a

polycrystalline material. I_D/I_G for the PyC here suggests that the material is in stage two of the amorphisation trajectory described in chapter 2, the stage between nanocrystalline graphitic carbon and amorphous carbon. A greater study and discussion of the Raman spectrum of PyC is presented by McEvoy *et al.*[123] The average crystallite size was calculated to be less than 10 nm.

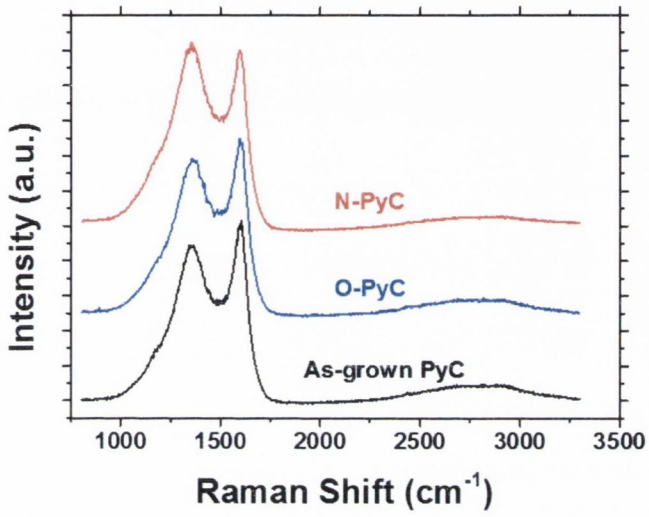

Fig. 4.4. Raman spectra of as-grown and plasma treated PyC. All spectral intensities normalised to G peak

4.4 Surface Chemistry

4.4.1 Water Contact Angle

Functionalisation of the surface of carbon films brings about a significant change in the surface chemistry of the film. For plasma treated PyC films, any changes in the surface chemistry of the films was initially investigated by studying the water contact angle of each sample type. Fig. 4.5 shows the water contact angles for as-grown PyC and plasma treated PyC.

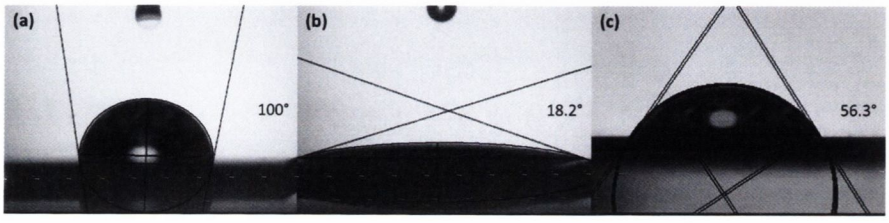

Fig. 4.5. Images of water contact angle for ***(a)*** *as-grown PyC,* ***(b)*** O_2 *treated and* ***(c)*** NH_3 *treated PyC.*

The as-grown PyC displays a water contact angle of approximately 100°, a typical value for graphitic carbon films which exhibit hydrophobic behaviour. The reduction in contact angle after the various plasma treatments is consistent with the introduction of polar surface groups which interact with the polar water molecules. Noticeably, the O_2 treated sample displays the lowest water contact angle of 18.2°, while the NH_3 treated sample has a contact angle of 56.3°. This can be accounted for if one considers the polarity of any introduced O or N surface moieties. O has a larger electronegativity than N and, thus, O groups will have greater polarity than N groups and, hence, the O_2 treated PyC film has the lowest contact angle.

4.4.2 XPS

XPS was used to probe the surface chemistry of the PyC films in a quantitative manner. as-grown PyC, and O_2 and NH_3 plasma treated were analysed using this technique. For brevity, O_2 and NH_3 treated PyC will be referred to as O-PyC and N-PyC. Survey spectra presented in fig. 4.6 clearly illustrate the differences between the various samples. The dominant feature here is the C 1s core level emission centred at 284.4 eV. The small O 1s at 532 eV for the as-grown sample is attributed to edge termination of the graphitic crystallites in the PyC films and, so, the presence of a certain level of oxygen is inevitable. The spectra presented in fig. 4.6 only show a portion of the spectral range measured (the Al Kα source allows measurements of binding energies up to 1486.7 eV) to highlight the pertinent core level peaks. The extended spectral range does not show any peaks associated with other elements.

After O_2 plasma treatment the O 1s peak increases significantly in intensity compared to the C 1s, signifying the introduction of oxygen moieties on to the surface of the film. This is accounts for the observed reduction in the water contact angle for the O_2 treated film. NH_3 plasma treatment sees as slight change in the shape of the O 1s peak with the N-PyC displaying a slightly narrower and more intense peak than the as-grown film. These differences, however, are well within the accuracy of the measurement system and do not signify any meaningful physical or chemical changes. Changing a setting as simple the X-ray incident angle could influence this. Thus, the oxygen contribution for N-PyC was determined to remain invariant compared to the as-grown sample; but the emergence of a very clear N 1s peak signifies the introduction of nitrogen to approximately 3 at. % on the film surface.

High resolution scans of the core level peaks spectral region for the samples allowed different spectral contributions to be fitted to give a quantitative measure of the level of functionalisation present in the various samples. Fig. 4.7 shows the

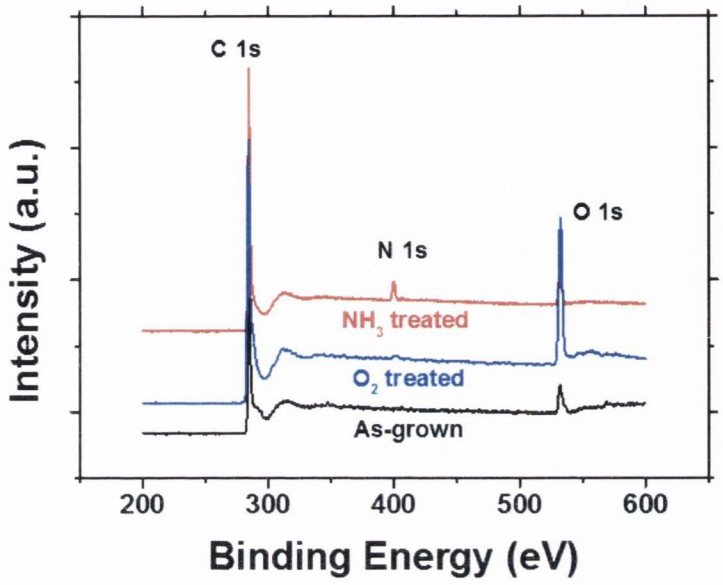

Fig. 4.6. Survey spectra of as-grown PyC, O_2 treated and NH_3 treated PyC. Core level peaks are indicated. All spectra normalised to C1s intensity.

C1s spectral region for as-grown PyC, O-PyC and N-PyC as well as the N1s region for the N-PyC sample. Spectral contributions are fitted and labelled.

Assignment of spectral contributions followed previously reported literature values for similar functionalised/doped graphitic systems as follows. The dominant feature of the C 1s region is a peak centred at ~284.4 eV; this is due to the presence of carbon in an sp^2 or graphitic configuration and is indicated as C=C in the figure.[132,133] A second peak found at ~285.5 eV arises due to the presence of sp^3-hybridised carbon in the sample.[133] This is labelled as C-C. The as-grown PyC samples in this study display predominantly graphitic character with a narrow C 1s peak width and minimal sp^3 carbon present. This is attributed to some edge sites in the graphitic lattice as well as the presence of some covalent bonding between adjacent crystallites. The slight shoulder is present in the higher binding energy portion of the C 1s region and arises due to the presence of various carbon functional groups. The previously mentioned small amount of oxygen in the PyC films is present in several moieties such as hydroxyl (286.6 eV),[44,134,135] carbonyl (288 eV)[44,133] and carboxyl (289 eV)[43] groups.

After O_2 plasma treatment the C1s region displays a significantly increased shoulder region which arises due to the increase in the level of oxygen moieties and sp^3 sites. After NH_3 plasma treatment, however, the level of oxygen groups remains invariant and the sp^3 contribution only increases a small amount. Two new peaks are seen in the shoulder of the C 1s peak which arise due to C-N groups in sp^2

(286.1 eV) and sp^3 (287.3 eV) configurations.[44]

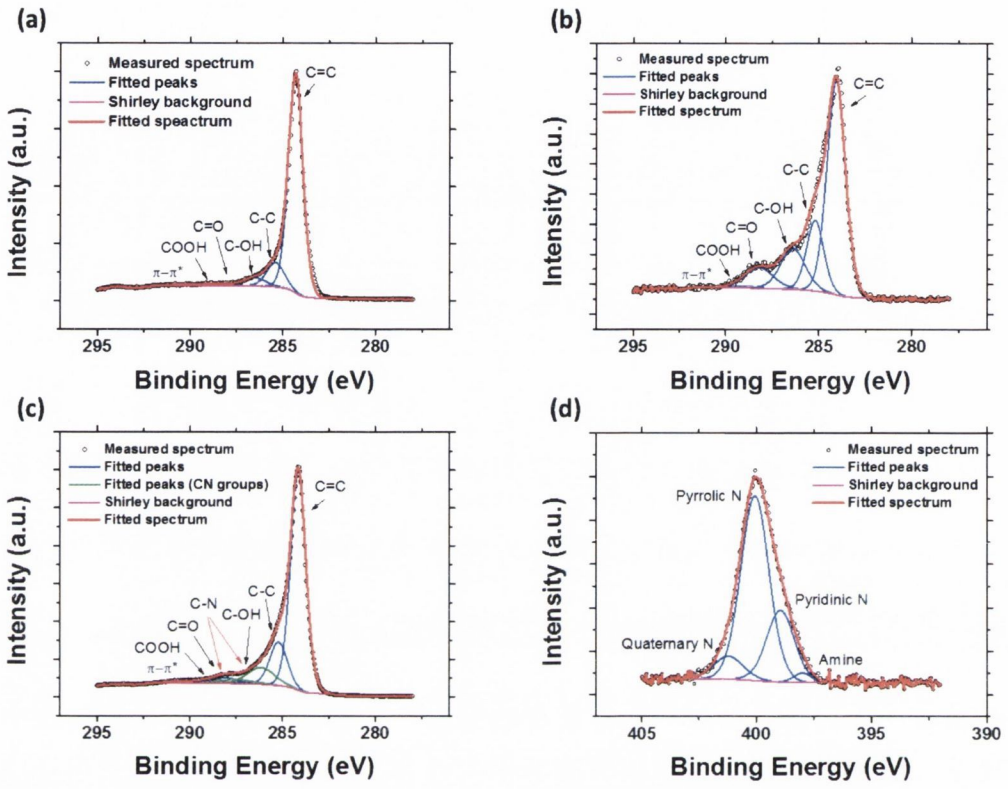

Fig. 4.7. ***(a)*** *C1s core level spectral region for as-grown PyC,* ***(a)*** *C1s spectral region for O_2 treated PyC,* ***(c)*** *C1s spectral region for NH_3 treated PyC,* ***(d)*** *N1s spectral region for NH_3 treated PyC*

Further insight regarding the nature of the nitrogen functional groups in the N-PyC was garnered by fitting spectral contributions to the N1s region for this sample. It was found that nitrogen is present in mostly pyrrolic (~400.1 eV)[44,55] and pyridinic (~399 eV)[43,44,51,136] with small amounts of quaternary nitrogen (401 eV)[43,44,55,137] and some amine groups (397.9 eV).[138,139] That the majority of the nitrogen is present in pyridinic or pyrrolic form suggests that the NH_3 plasma treatment introduces nitrogen functional groups along the edges of the graphitic lattice of the PyC.

Two-Step Plasma Treatments

Additional measurements were performed on PyC samples which had been subjected to an initial O_2 plasma treatment and then a subsequent NH_3 plasma treatment. It is known that for some functionalisation treatments, it is necessary to initially generate reactive sites before functionalising with the desired chemical species. In this case it was investigated as to whether the initial O_2 plasma treatment influences the

incorporation of nitrogen into the film after the subsequent NH_3 treatment. Shown in fig. 4.8 is a comparison of the survey and C 1s spectra comparing N-PyC produced via a simple NH_3 treatment and that produced by the two-step process. The survey spectra in fig. 4.8 (a) clearly show little to no difference between the two films in terms of relative intensities of the core level peaks. Indeed, it was found that nitrogen was present to a level of ~3 at. %, consistent with the samples treated only with NH_3 plasma. Of most interest in this measurement is the fact that all oxygen introduced into the film during the first O_2 plasma step has been removed, indicating the strong reducing power of the NH_3/H_2 plasma mixture. Analysis of high resolution C 1s scans for both samples reveals little change between the two. Both exhibit the same surface functional groups at similar relative concentrations. The relative intensities of the various oxygen moieties shows that oxygen groups from the first plasma step have been effectively removed in the second step. Given the lack of difference between these two samples, all subsequent work on N-PyC in this study was carried out on samples which had only been subjected to the single NH_3 plasma treatment.

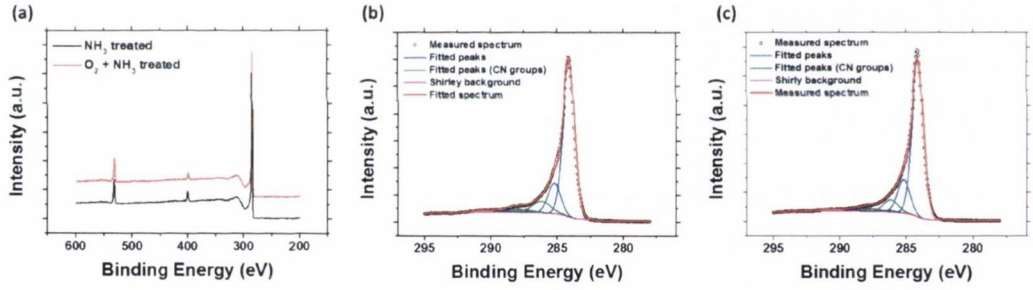

Fig. 4.8. ***(a)*** *Survey spectra for N-PyC produced via single or two step plasma treatments.* ***(b)*** *C 1s core level peaks for N-PyC produced via a single NH_3 plasma treatment.* ***(c)*** *C 1s core level peaks for N-PyC produced via a two-step plasma treatment of O_2 initially, followed by a subsequent NH_3 treatment*

4.5 Electrochemical Characterisation

4.5.1 Ferri/ferro-cyanide

Initial electrochemical characterisation of the various PyC films was performed using a redox probe of ferri/ferro-cyanide ($[Fe(CN)_6]^{3-/4-}$) to investigate the kinetics of the charge transfer at the electrode surface. The ET kinetics of this probe are subject to some discussion in the literature. Traditionally viewed as an outer-sphere probe, this view has recently been questioned by several prominent electrochemists. This probe has been shown to exhibit inner-sphere behaviour where the presence of redox groups and a locally modified electronic structure due to structural defects

enhances the ET kinetics.[140–143] Additionally, the history of "inert" electrodes has shown to have a significant bearing on the electrochemical response of this probe, negating its suitability as a means of investigating basal plane graphitic materials.[144] With this in mind, the ferri/ferro complex presents a suitable probe to investigate the influence of plasma treatments of PyC on electrochemical processes at the PyC surface. Both CV and EIS were performed using this system, with the results of both sets of measurements presented in fig. 4.9.

The peak definition for the as-grown film is very poor; indicative of rather sluggish charge transfer behaviour. In fact, so poor is the peak definition that the potential at which redox peaks are positioned cannot be identified. The plasma treated samples, however, both show considerably different voltammetric responses with a considerably better peak definition for each. The peak separation, ΔE_p, is related to the rate of ET between the electrode and electrolyte. This peak separation value can, in turn, be used to calculate the so-called heterogeneous ET rate constant, k^0, which gives a quantitative evaluation of the ET kinetics at the electrode. This was calculated using the method outlined by Nicholson[145] and a thorough explanation of the calculation is dealt with by Lyons and Keeley.[146] This technique is only applicable for systems exhibiting quasi-reversible ET behaviour and, furthermore, is not the only method for calculating kinetic rate constants,[147] resulting in some discrepancies in calculations, reporting and comparisons of this value in the literature. Indeed, a comparison of rate constants with literature works is instructive when assessing the performance of an electrode in a given redox probe, but a more accessible comparison to previous works can be drawn by directly comparing values of ΔE_p. All values for k^0 presented in this thesis are calculated using the technique described here and, thus, are a valid metric within this thesis.

The O-PyC sample displays a peak separation of 179.6 mV, a value which corresponds to an ET rate with k^0=0.0153 cms^{-1}. For N-PyC, ΔE_p=71.7 mV and k^0=0.044 cms^{-1}. The indicates that the N-PyC exhibits significantly enhanced ET kinetics compared to the O-PyC. It also must be noted that the enhanced ET kinetics of the functionalised PyC films exist in spite of the electrostatic repulsion between the negatively charged ferri/ferro-cyanide anion and negatively charged oxygen and nitrogen surface moieties. This repulsion has been shown to impede ET in some systems.[142]

EIS also reveals the substantially enhanced ET kinetics of the plasma treated PyC compared to the as-grown sample. The diameter of the semi-circular portion of the nyquist plots in fig. 4.9 (b) is related to the resistance to charge transfer, R_{ct}. This was calculated by fitting the measured data to a Randles equivalent circuit model. The data points represent the measured EIS data while the solid lines are the fitted

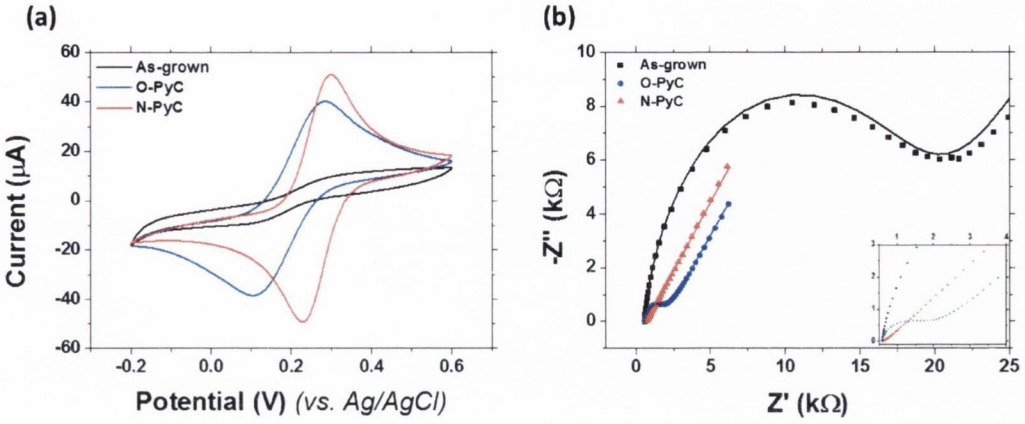

Fig. 4.9. ***(a)*** *Voltammetric response of as-grown and plasma treated PyC in 1 mM* $[Fe(CN)_6]^{3-/4-}$ *in 1 M KCL background electrolyte. Scan rate is 100 mV* s^{-1}. ***(b)*** *Nyquist plots for the same system when measured using electrochemical impedance spectroscopy at a DC potential of +0.26 V.* ***Inset:*** *Rescaled Nyquist plot showing smaller semi-circular regions of O-PyC and N-PyC.*

Table 4.2. R_{ct} *values for as-grown PyC, O-PyC and N-PyC as calculated by Randles equivalent circuit modelling.*

Sample	As-grown	O-PyC	N-PyC
R_{ct} **(kΩ)**	18	1.35	0.21

data. The calculated values are presented in Table 4.2 where it is apparent that these results are consistent with the CV data and confirm that the N-PyC exhibits superior ET kinetics to that of the O-PyC.

The enhanced ET behaviour of the plasma etched PyC films compared to the as-grown material is attributed to two effects. As is evident from characterisation of the physical morphology of the samples (see section 4.3), the plasma treatments reactively etch a small amount of material from the surface. This increase in surface roughness exposes a greater density of electrochemically active edge plane graphitic sites than the rather inert basal plane sites, compared to the as grown PyC. Previous work on O-PyC has documented this effect and the same is also valid for N-PyC.[131] Fig. 4.10 illustrates the basal and edge plane regions of graphitic carbon. In ordered systems such as graphite the difference in reactivity between these two locations is rather marked. In addition to the increased exposure of edge plane sites, the presence of the functional groups on the electrode surface enhance the ET kinetics. While it is difficult to deconvolute the influences of these two effects, both contribute to the facile ET kinetics observed after plasma treatment.

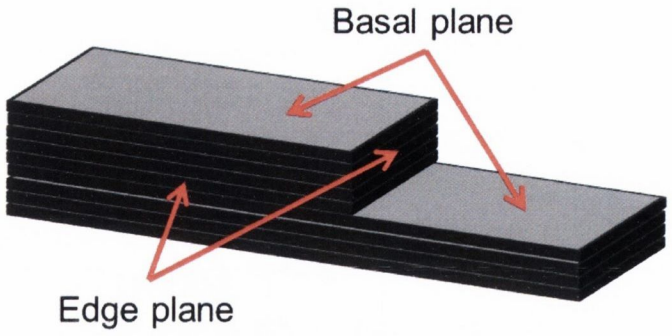

Fig. 4.10. Schematic illustrating the basal and edge plane regions of graphitic carbon.

4.5.2 *Hexa amine ruthenium (III) chloride*

Further electrochemical measurements were performed using the redox probe hexa amine ruthenium (III) chloride ($[Ru(NH^3)_6]^{3+}$). This probe exhibits ideal outer-sphere ET kinetics which are not influenced by surface microstructure or the presence of surface functionalities. The voltammetric response is shown in fig. 4.11 where it is clear that there is no obvious change in the ET behaviour of the PyC after any plasma treatment. CV was performed at a number of scan rates and a linear relationship was observed to exist between the square root of the scan rate, ν, and the peak redox current, i_p. This is illustrated in Fig. 4.11 (b). This signifies that the redox events which contribute to the peaks in the voltammetric response are diffusion controlled processes, according to the Randles-Sevcik equation for solution-based Nernstian redox events (equation 2.9).

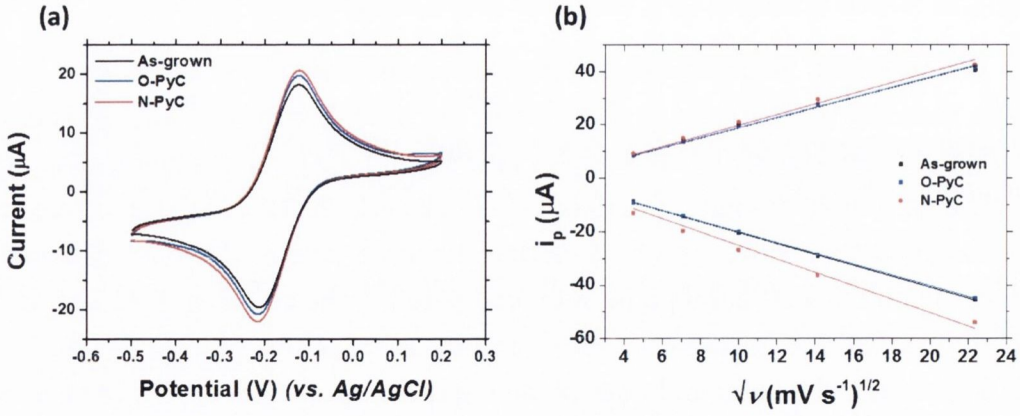

Fig. 4.11. ***(a)*** *Voltammetric response for as-grown and plasma treated PyC films in 1 mM hexamine ruthenium (III) chloride in 1 M KCL background electrolyte. Scan rate is 100 mV s^{-1}.* ***(b)*** *Plots of $\sqrt{\nu}$ versus peak redox current (i_p) for the same samples. Data is taken from voltammetry at a range of scan rates.*

4.6 Electrochemical Applications

Electrochemical studies of plasma treated PyC was extended to electrochemical sensing of biomolecules. The inexpensive nature of PyC when compared to typical commercial carbon electrode materials such as Edge Plane Pyrolytic Graphite (EPPG) makes this an attractive alternative for commercial applications. Initial tests in to the applicability of plasma treated PyC were carried out by performing CV in dopamine (0.1 mM). From fig 4.12 below it is clear that both the O-PyC and N-PyC films exhibit a reduction in the oxidation peak potential compared to the as-grown film. This apparent electrocatalytic effect coupled with the better defined oxidation peak compared to the as-grown film suggests some applicability of these materials in sensing.

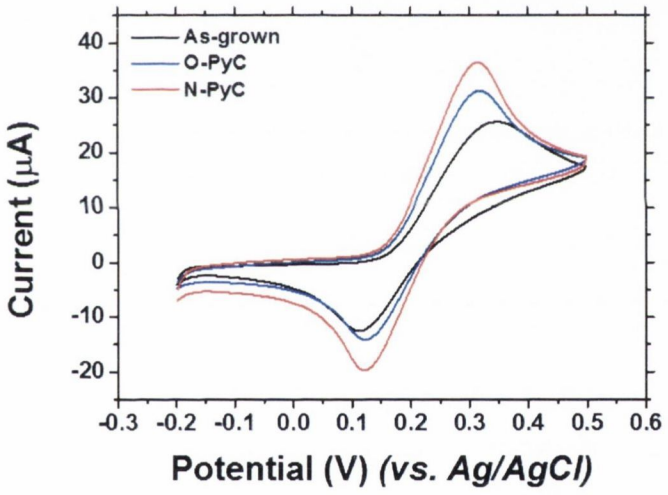

Fig. 4.12. Voltammetric response of as-grown and plasma treated PyC in dopamine hydrochoride (0.1 mM) in a background electrolyte of pH 7 phosphate buffer solution. Scan rate is 100 mV s^{-1}.

Measurements performed with Dr. Gareth P. Keeley demonstrated further electrochemical sensing properties of PyC in greater detail. This study involved the successful simultaneous detection of dopamine and paracetamol with O-PyC. Shown in fig. 4.13 (a) is the voltammetric response of O-PyC in separate solutions of dopamine and paracetamol. The well defined oxidation peaks can be clearly distinguished from each other which allows both oxidation events to be detected without either influencing the other. Fig. 4.13 (b) shows the voltammetric response at an O-PyC electrodes for a solution containing both dopamine and paracetamol for a solution of just dopamine and paracetamol and for a second solution which also includes ascorbic acid and uric acid. The two peaks are still well resolved with no interference from the other biological molecules; highlighting the suitability of

this electrode in realistic samples where many species are present.

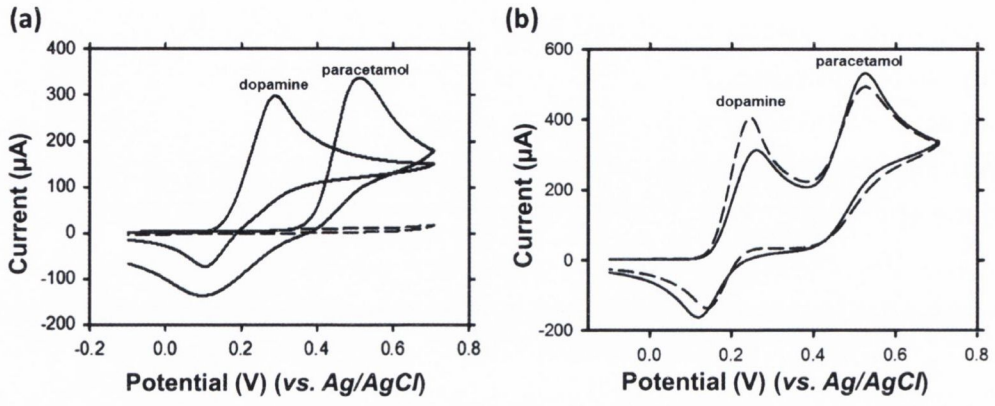

Fig. 4.13. ***(a)*** *Voltammetric response of O-PyC in dopamine (1 mM) and paracetamol (0.1 mM) measured in separate solutions of pH 7 buffer solution at O-PyC electrodes. Background electrolyte response shown as dashed data. Scan rate is 100 mV* s^{-1}. ***(b)*** *Response of a mixture of dopamine and paracetamol (same concentrations) for as-grown PyC and O-PyC. Scan rate of 50 mV* s^{-1}.

The performance of PyC and O-PyC electrodes in the detection of dopamine and paracetamol was compared to commercially available electrodes. Basal Plane Pyrolytic Graphite (BPPG) consists of pure basal plane graphite and is used as an inert comparison electrode. EPPG electrodes are extremely electrochemically active due to the pure edge plane electrode surface. Fig. 4.14 shows that, untreated PyC shows a very sluggish response which is, in fact, worse than that of BPPG. O-PyC, however, displays a response comparable to that of EPPG. From this, it can be concluded that the introduction of electro-catalytically active edge plane sites in the PyC surface during plasma treatment is of great importance to the enhanced detection performance. That the performance of the easily prepared O-PyC is similar to that of EPPG suggests that O-PyC is a viable alternative electrode material to the more expensive EPPG.

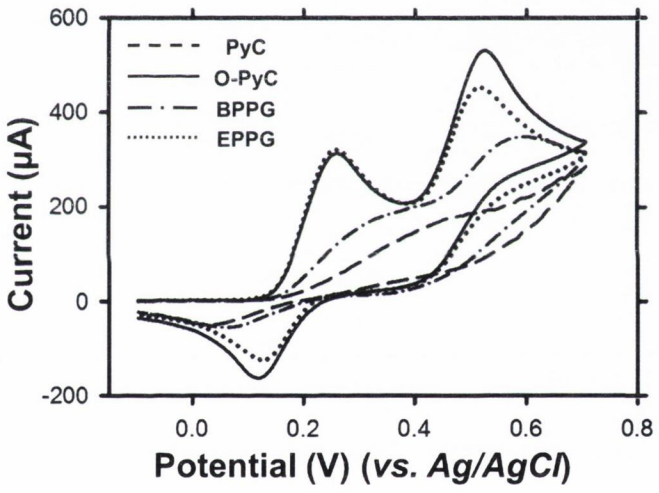

Fig. 4.14. A comparison of the voltammetric response of as-grown PyC and O-PyC with EPPG and BPPG in dopamine (1 mM) and paracetamol (0.1 mM).

4.7 Conclusions

Plasma treatment of PyC films with O_2 and NH_3 was shown to dramatically alter the chemical properties of these films. Only minor changes to the surface morphology were observed, the most significant change being a roughening of the surface. The surface chemistry was significantly modified with the reduced water contact angle signifying the introduction of polar surface groups after treatment. This was confirmed via XPS where spectral contributions consistent with oxygen (for O-PyC) and nitrogen (for N-PyC) groups were observed and quantified. A two-step plasma treatment process whereby and initial O_2 treatment was followed by a subsequent NH_3 treatment found little significant difference between samples treated in this manner or N-PyC prepared by a single NH_3 treatment. The find of most significance for the two-step process was that a NH_3 plasma appears to perform excellently in the removal of surface oxygen moieties.

Electrochemical characterisation of O-PyC and N-PyC showed that these films exhibit significantly enhanced electrochemical properties compared to as-grown PyC. The inner-sphere ferri/ferro-cyanide redox probe displays a much narrower peak to peak separation for plasma treated films compared to as-grown PyC. This is indicative of rather facile ET properties at these chemically modified electrode surfaces. The heterogeneous rate transfer constant, k^0, was calculated from this peak separation and it was found that k^0=0.0153 cm s^{-1} for O-PyC and k^0=0.044 cm s^{-1} for N-PyC. No value could be determined for the as-grown PyC, so poor was the ET. The enhanced ET behaviour was attributed to the increased concentration of edge plane graphitic sites caused by the roughening during the plasma treatment in addition to the presence of the surface moieties themselves. Measurements which employed outer-sphere redox probes showed a reversible response typical of diffusion controlled systems. An extension of the electrochemical measurements investigated the use of plasma treated PyC electrodes in the detection of biomolecules. O-PyC and N-PyC both showed a reduction in the detection potential of dopamine solutions compared to as-grown PyC. Results on N-PyC were published in Phys. Chem. Chem. Phys.[148] Simultaneous detection of both dopamine and paracetamol using O-PyC was observed and shown to be a valid alternative electrode material to expensive commercial EPPG electrodes. A more comprehensive study on this work was published in Anal. Methods.[149]

This work on PyC could be extended in several directions for future work. Alternative plasma treatments could be investigated to functionalise PyC with other heteroatoms. In particular, phosphorus and boron-doped carbon materials are

attracting much attention in the research community at present. Use of precursors such as phosphine or diborane could allow the plasma treatment presented here to be used for the production of such materials. Plasma functionalised carbon films could be used as a starting point for the chemical attachment of further functional or organic groups on the film surface. This groups could ensure selectivity to certain biological analytes in further sensing applications.

Chapter 5

Plasma Treated CVD Graphene

5.1 Introduction

The expertise developed in using downstream plasma treatments to functionalise CVD grown PyC films was extended to the more exotic graphene. Graphene films were grown via CVD on catalytic transition metal substrates. Graphene has generated huge interest in the research community in the last ten years and is much more heavily researched than other graphitic materials like PyC. Both monolayer graphene and Multi-Layer Graphene (MLG) samples were investigated.

5.2 Monolayer CVD Graphene

Monolayer graphene was grown *via* CVD on Cu foils and transferred to SiO_2 substrates, as described in chapter 3.

5.2.1 Plasma Treatment

For monolayer CVD graphene films, plasma treatments were carried out both directly on the growth substrate or after transfer to SiO_2. XPS measurements required that the graphene be mounted on an electrically conductive substrate so plasma treatments and subsequent measurements were carried out on the growth Cu foil. All other characterisation techniques were performed on SiO_2 wafers and the samples were transferred to these substrates prior to the plasma exposure.

One must consider, however, that transferring a graphene film to another substrate may influence its susceptibility to functionalisation by the plasma exposure compared to a film which remains on the Cu foil. It is likely that small tears and cracks are introduced into the graphene film during the transfer process. These may facilitate greater access of plasma radicals to the graphene and increase

the degree of functionalisation. With this in mind, one can directly compare different samples provided they have been exposed to plasma under the same criteria; *viz*, which substrate was used. However, comparing results of films that were exposed on Cu foils and SiO_2, while useful for qualitative comparisons, is likely to be somewhat inaccurate.

O_2 treatments were carried out at a flow rate of 100 sccm for various times, while for NH_3 treatments a gas mixture of NH_3 (50 sccm) and H_2 (50 sccm) was used. A power of 1 kW was used for all plasma exposures.

5.2.2 Oxygen Plasma Treatment

Water Contact Angle

Any changes in the surface chemistry were initially investigated by measuring the water contact angle of the plasma treated graphene. To this end, as-grown graphene was transferred to SiO_2 wafers and various plasma treatments were performed. Fig. 5.1 shows how the water contact angle evolves with increasing exposure to O_2 plasma. The significantly decreased contact angle is indicative of a material heavily functionalised with polar functional groups.

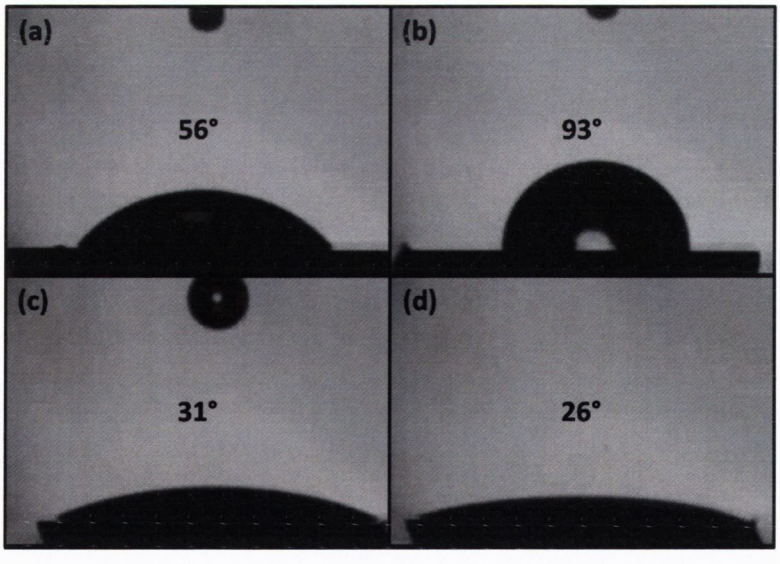

Fig. 5.1. Water contact angles for **(a)** *bare SiO_2,* **(b)** *pristine graphene,* **(c)** *10 s O_2 treated graphene and* **(d)** *300 s O_2 treated graphene.*

Raman Spectroscopy

The sensitivity of Raman spectroscopy to the structural changes in graphitic materials allowed changes in the graphene following plasma treatment to be very

accurately probed. As monolayer graphene is essentially "all surface", any surface functionalisation by plasma treatments affect the entire film. Additionally, the much larger average crystallite sizes compared to PyC means that the graphene spectrum is much more sensitive to the introduction of defects. As such, Raman spectroscopy is the ideal technique for probing the structural changes in monolayer graphene after plasma treatments.

Pristine graphene was exposed to a range of different O_2 exposure times and the corresponding Raman spectra are presented in fig. 5.2. All spectra presented in here were taken by performing scanning Raman over an area of 30x30 μm and taking many discrete spectra over this area; typically 120x120 spectra were recorded. These were then averaged to give a representative spectrum for large areas of the graphene film as presented here. From this data it is evident that the starting pristine graphene is very high quality monolayer material with long range ordering and minimal defects due to the lack of a D band and a narrow intense 2D band with a FWHM of 31 cm^{-1}, respectively

After even just 10 s plasma treatment the 2D band is heavily suppressed and a strong D band emerges. This is consistent with the creation of many defects in the graphitic structure. Also of note is the clear emergence of a D' band on the shoulder of the G peak, lending further evidence to the creation of structural defects. Increasing the plasma exposure time causes the 2D band to reduce further in intensity until it is almost completely suppressed after 5 minutes exposure time. The D' band increases in intensity with exposure time until it merges with the G band to the point that the two cannot be clearly distinguished. This behaviour is consistent with that observed by Cançado *et al.* for mechanically exfoliated graphene flakes bombarded by Ar^+ ions.[111]

Section 2.3.2 showed how the average crystallite size in graphene, L_a, can be related to I_D/I_G in terms of the laser energy, where I_D and I_G represent the intensities of the D and G peaks, respectively. In the case of the O_2 plasma treated graphene, these equations cannot be used as the material has moved far enough along the amorphisation trajectory that the level of defects is too high for the equation to be valid. Indeed, the merging of the D' peak with the G peak makes it difficult to accurately determine I_G.[102]

Scanning Raman Analysis

Further Raman analysis was performed by mapping out various scanned regions of the graphene films. An instructive selection of Raman maps are shown in fig. 5.3 where the G band intensity (I_G), D to G intensity ratio (I_D/I_G) and 2D FWHM are

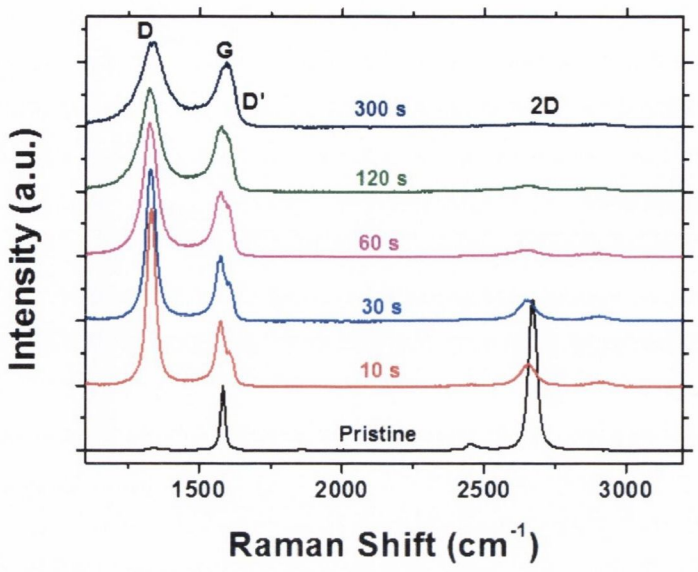

Fig. 5.2. Raman spectra for pristine and various O_2 plasma treated graphene.

presented for pristine graphene and that exposed to 10 s O_2 plasma. Also included are optical images of the areas over which the spectra were measured, showing little surface contamination on the graphene with no visible change after plasma treatment.

Analysis of the I_G map reveals that the graphene film covers the entire area with minimal tearing or holes, as shown by the reasonably uniform intensity across the sample. Some islands of secondary growth are present which manifest as bright areas on this map as I_G increases in intensity with the addition of subsequent graphene layers. A similar map is seen for I_G for the plasma treated sample, but greater contrast is observed between the monolayer region and secondary islands. A great deal of information can be garnered from the I_D/I_G map, however. For the pristine graphene, there are small areas of high I_D/I_G intensity, signifying areas of higher defect levels. However, the actual instance of these areas is rather low and the graphene film as a whole can be considered to be of very high quality. After just 10 s O_2 plasma treatment this map changes a huge amount, with defects introduced across the whole film as evidenced by the much brighter intensity profile. This is consistent with the plasma treatment uniformly introducing defects on the graphene surface. Additional information about the plasma functionalisation process can be determined from the fact that there are discrete spots of very low I_D/I_G intensity which appear as the dark spots in this map. These areas correspond to the islands of bilayer growth where the secondary islands suffer the plasma damage and protect the layer below. Hence, it can be deduced that the plasma treatment only affects the very surface of the films

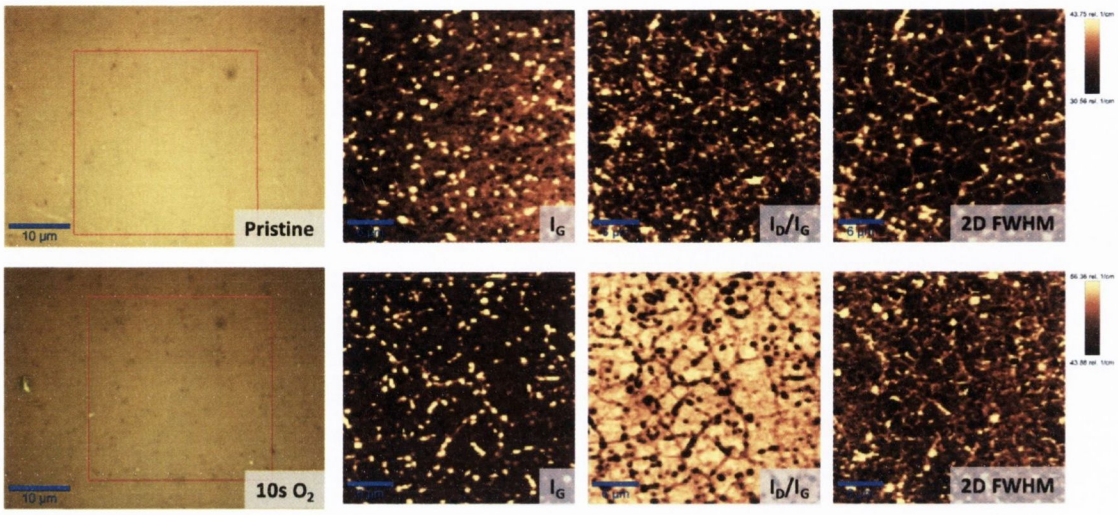

Fig. 5.3. Scanning Raman maps over a 30x30 μm area showing the G band intensity (I_G),D to G peak intensity ratio (I_D/I_G) and the peak width of the 2D band. ***Top row:*** *pristine graphene.* ***Bottom row:*** *10s O_2 plasma treated graphene. Bright areas signify a high signal; dark areas a low signal.*

as I_D/I_G is lower in these bilayer regions.

The 2D FWHM map for the pristine sample shows a rather uniform film with a typical FHWHM of 30-35 cm^{-1} with the brighter areas exhibiting a FWHM of approximately 45 cm^{-1}. This information is consistent with the I_G map in that it confirms that the sample largely consists of high quality monolayer graphene with a small number of bilayer islands also present. Additionally, the edges of the graphene domains are evident as lines of slightly wider 2D FWHM, corresponding to a slight disorder associated with the domain edges. Visualising the graphene domains in this manner allows quantitative analysis of domain size distribution and uniformity of coverage, should that be desired. After 10 s plasma treatment the 2D FWHM broadens to a a width of >45 cm^{-1} in most regions, corresponding to the reduction in the long range ordering of the film as defects are introduced.

Scanning Raman analysis was also performed on the 300 s O_2 plasma treated sample. Fig. 5.4 (a) and (b) show the I_G and I_D/I_G maps for this sample, respectively. From this it is clear that the I_G map appears to have the opposite intensity profile than was observed for the 10 s O_2 plasma treated sample, with the bilayer regions appearing as regions of low intensity here when compared to the monolayer areas. This is easily explained by considering the effect of the very large D' contribution for the 300 s sample. In this case the D' has merged with the G band, increasing the apparent intensity of the G band relative to that of the D peak. The islands of second layer growth protect the layer beneath from plasma damage in the same manner as for the 10 s sample and, thus, a lower D' intensity and resultant apparent G intensity

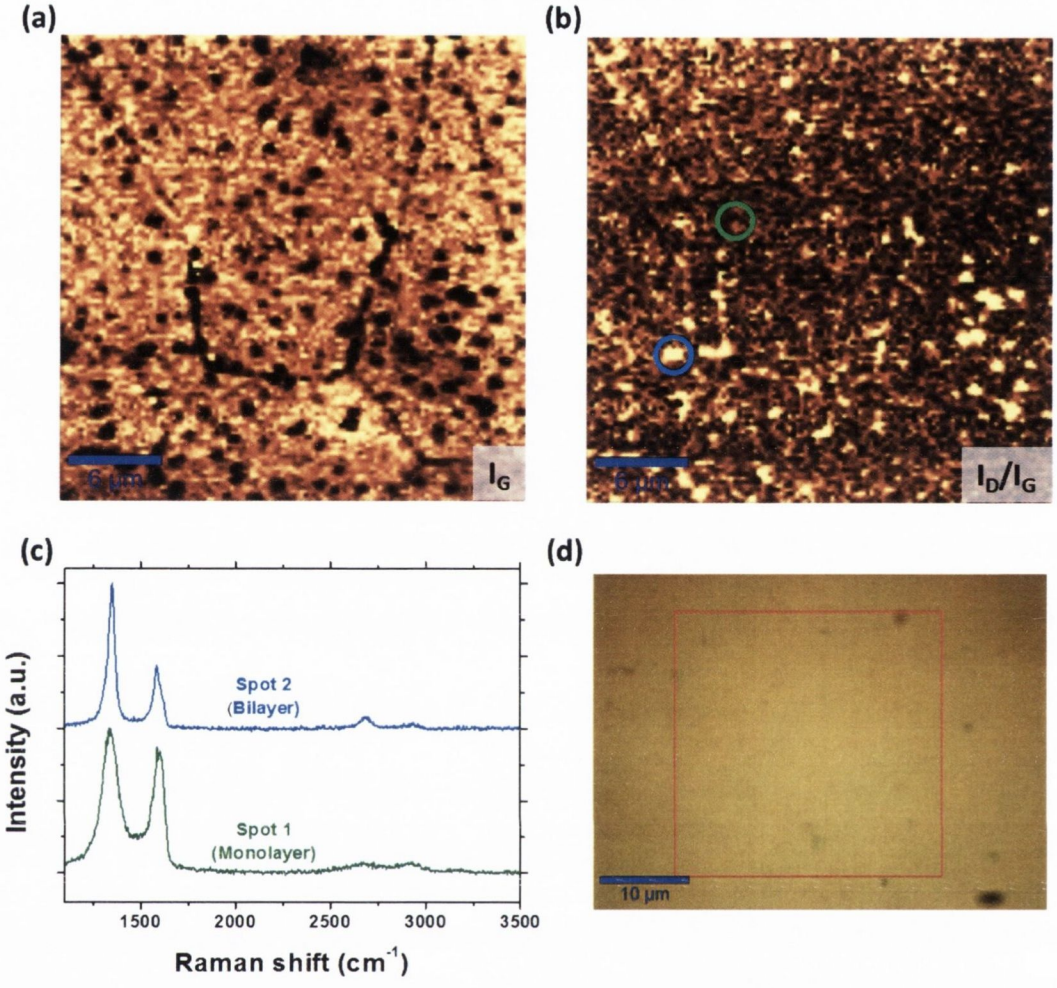

Fig. 5.4. Scanning Raman maps over a 30x30 μm area on a 300 s O_2plasma treated sample showing ***(a)*** *the G band intensity (I_G) and* ***(b)*** *the D to G band intensity ratio (I_D/I_G) map.* ***(c)*** *Raman spectra pertaining to the marked regions on the ID/G map.*

are observed. This is corroborated by the map of I_D/I_G, which shows bright spots corresponding to secondary islands less susceptible to plasma induced defects. The effect of the reduced contribution of the D' peak to the apparent G band intensity is clearly illustrated in the spectra in fig. 5.4 (c). The spectrum for the monolayer region (marked as 1, green data plot) shows the D and G bands of similar intensity. The spectrum corresponding to a region of second layer island (marked as 2, blue data plot) shows a much lower apparent I_D/I_G, due to the reduced prominence of the D' peak. An optical image of the area over which the scans were taken is shown in fig. 5.4 (d). This clearly shows no visible damage to the graphene film, even after such a long O_2 plasma exposure.

X-ray Photoelectron Spectroscopy

While Raman spectroscopy gave great insight into the effects of various O_2 plasma treatments on the crystalline structure of graphene films, no information was revealed regarding the functionalisation of the film surface during the plasma treatment process. To this end, XPS was employed to gain a quantitative insight into the nature of any surface groups resulting from the plasma exposure. Survey scans of various films revealed the effects of the varying O_2 plasma exposure times. Fig. 5.5 (a) shows the survey spectra for pristine, 10 s and 300 s O_2 plasma treated graphene with the intensities of all spectra normalised to the C 1s core level. It is immediately apparent that the pristine graphene sample contains very little oxygen, as evidenced by the very small O 1s core level. Increasing plasma exposure times result in an increase in the intensity of this peak, signifying a greater amount of oxygen functional groups present on the surface of the graphene film.

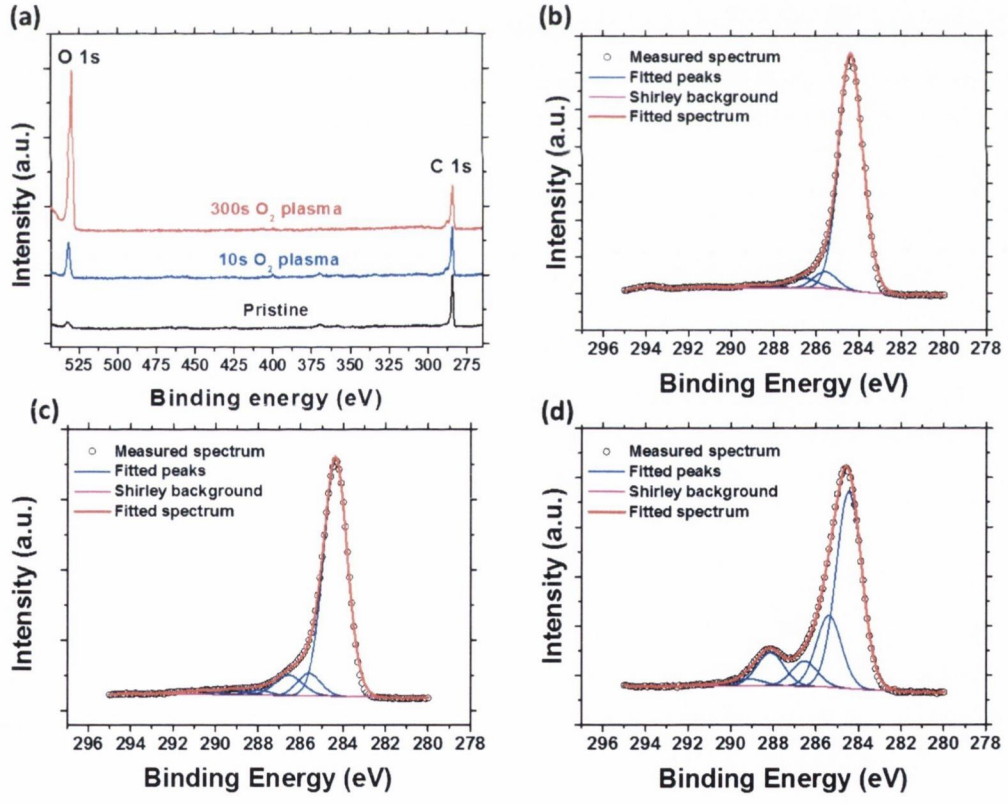

Fig. 5.5. ***(a)*** *Survey spectra for pristine, and various O_2 plasma treated graphene films. Fitted C 1s core level peak for* ***(b)*** *pristine,* ***(c)*** *10 s and* ***(d)*** *300 s O_2 plasma treated graphene.*

High resolution scans of the C 1s core level for the various samples allowed different spectral contributions to be assigned to this spectral region in each case. A first glance shows broadening of the C 1s peak with increased plasma treatment

time as well as the evolution of a shoulder peak at higher binding energies. The binding energy values used in the fitting of the core level peaks that follows in this section were based on the same literature values as used for plasma treated PyC in chapter 4. The as-grown graphene film displays a prominent graphitic peak at 284.4 eV with minor contributions from other species. Defects or sp^3 carbon sites are manifested as a peak at 285.5 eV, hydroxyl groups as a peak at 286.6 eV, carbonyl groups at 288 eV and carboxyl groups at 289 eV. A satellite of the graphitic peak is also found at 291 eV. As expected for the pristine graphene film, the C 1s peak primarily consists of the graphitic peak with only small contributions from carbon atoms in non-graphitic environments. This is in keeping with the Raman spectroscopy data, which shows a spectrum typical of high purity monolayer graphene. The small sp^3 and functional group contributions in this sample can be somewhat attributed to edge-termination of the graphene lattice and the presence of structural defects. With oxygen plasma treatment the intensity of the peaks relative to the graphitic peak increases. These show that the oxygen plasma treatment leads to the incorporation of oxygenated functionalities on the surface of the graphene and, in turn, shows that defect contributions in the Raman spectra arise from the presence of such functional groups and not just from edges and vacancies. Of note, also, is the increase in prominence of the sp^3/defect peak at 285.5 eV with increasing treatment time. As oxygen reacts with the graphene film, the sp^2 symmetry is destroyed and more sp^3 sites emerge; which corresponds to the increased level of oxygenated functional groups. The increased prominence of sp^3 sites is consistent with the observed evolution of the Raman spectrum with increasing plasma exposure time. As more oxygen moieties attach to the graphene, greater levels of defects in the graphitic lattice occur.

Electrochemical Measurements

Following the success in electrochemical measurements of plasma functionalised PyC, it was investigated if plasma functionalised graphene displayed any enhanced or otherwise interesting behaviour in electrochemical measurements. Graphene films were employed as the working electrode in a typical three electrode cell set-up with 1 M KCL background electrolyte. The voltammetric response of both pristine and 10 s plasma treated films is shown in fig. 5.6. The rectangular profile of the voltammograms is a typical charging current in background electrolyte. However, the charging current of the 10 s O_2 plasma treated graphene film is significantly reduced when compared to the pristine film, suggesting a smaller surface area accessible to the electrolyte. It was deduced that the plasma treatment and

functionalisation of the graphene film drastically compromises the conductivity of the graphene film. This is easily explained if one considers how functionalisation of the film disrupts the conductive graphitic lattice with defect sites. As graphene is all surface, such surface functionalisation as is achieved *via* the plasma exposure affects the conductivity of the whole film. As a result of this, the apparent surface area of the graphene electrode which can maintain a charging current is much reduced in the functionalised graphene film compared to the pristine. Additionally, the profile of the charging currents in fig. 5.6 are rather diagonal, as opposed to the completely horizontal profile expected for a pure double layer charging. This suggests significant resistive components in the system, likely due to issues with electrically contacting the Au-coated periphery of the film using crocodile clips. In light of this, no further electrochemical measurements were carried out of plasma functionalised monolayer graphene.

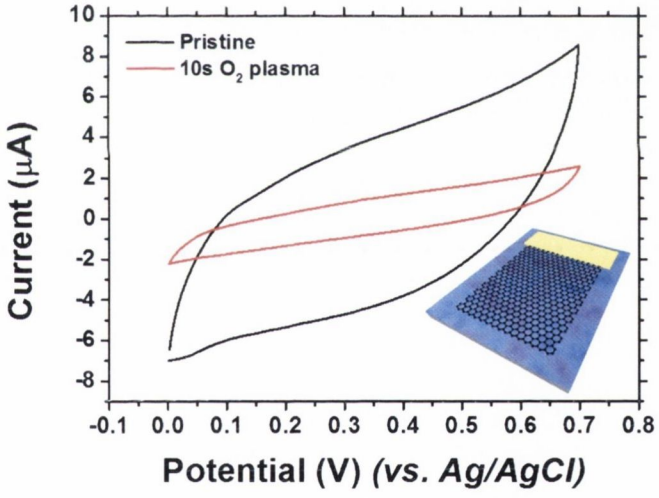

Fig. 5.6. Voltammetric response of pristine and 10 s O_2 plasma etched graphene in 1 M KCl background electrolyte. Scan rate is 100 mV s^{-1}. ***Inset:*** *Illustration showing Au contact on graphene film.*

5.2.3 Ammonia Plasma Treatment

N-doping of monolayer graphene was investigated using NH_3 plasma. Initially, pristine graphene was exposed directly to NH_3 plasma in the same manner that PyC was in chapter 4. It was found that this treatment did not affect the graphene at all. As shown in fig. 5.7, no obvious changes in the Raman spectrum are visible. While there may be some minor change to I_D/I_G, there is no obvious broadening of any of the peaks, a D' peak is not evident and no suppression of the 2D peak has taken

place. Additionally, no spectral shift of the characteristic peaks to higher Raman shifts has occurred; this has been suggested as an indication of N-doping in graphitic systems. It was deduced that, as NH_3 is not as reactive with carbonaceous materials as O_2, the highly crystalline pristine graphene does not offer viable reactive sites for nitrogen groups to attach to the graphene. As a result, further investigations into N-doping of graphene using NH_3 plasma were carried out using the two-step plasma treatment process initially investigated with PyC.

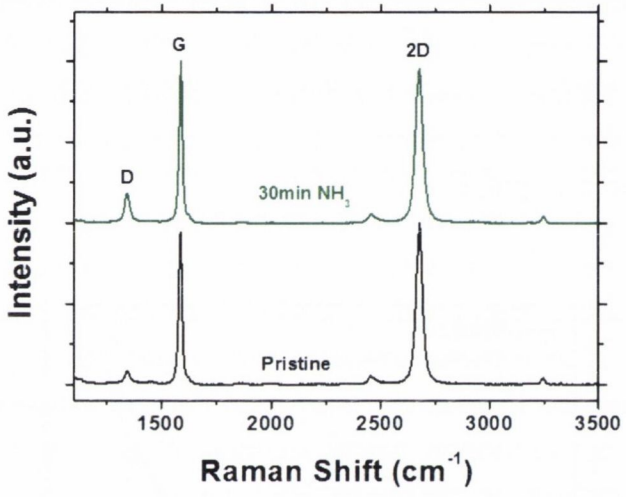

Fig. 5.7. Raman spectra for pristine graphene and plasma treated graphene exposed to only NH_3 plasma.

For two-step plasma treatments, graphene films were initially exposed to 300 s O_2 plasma in the same manner as previously, before a subsequent NH_3 treatment for 30 minutes. The Raman spectrum of such a sample is shown in fig. 5.8 (a) in addition to the spectra for pristine and O_2 treated graphene. Following the NH_3 plasma treatment there is an evident reduction in the intensity of the D peak with an accompanying reduction in its width. There is also a re-emergence of the 2D band. Both of these features suggest some removal of defects and the restoration of graphitic ordering. Additional information lies in the positions of the G and 2D peaks. The apparent up shift of the G peak in the O_2 treated sample is explained by the presence of a prominent D' peak in the heavily defective film. This merges with the G peak and causes the apparent G peak to appear slightly upshifted. Following the NH_3 treatment, the G band is upshifted further, despite a clear reduction in defect levels. Additionally, the 2D peak of the NH_3 treated sample is seen to be upshifted compared to that of the pristine graphene. An explanation for such upshifting of the G and 2D peak positions is N-doping of the graphene film, although there are many conflicting reports on this. To categorically understand the chemical nature of

the graphene film after the two stage plasma process, one must turn to elementally sensitive techniques, such as XPS.

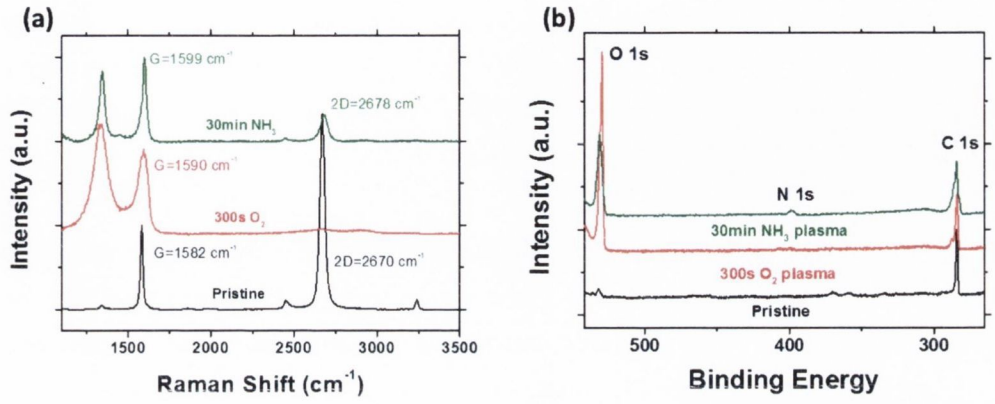

Fig. 5.8. ***(a)*** *Raman spectra for pristine, O_2 and O_2+NH_3 plasma treated graphene. Positions of spectral peaks are marked for each sample.* ***(b)*** *XPS survey scans for the same sample set. All intensities normalised to the C 1s intensity.*

XPS was employed to investigate the functional groups on the various graphene films; survey spectra for the these are shown in fig. 5.8 (b) A significant reduction in oxygen content after the NH_3 treatment is evidenced by the reduction in the O 1s peak intensity. Additionally, the emergence of the N 1s peak signifies the presence of nitrogen groups on the film. The reduction in oxygen content in the NH_3 treated film is consistent with the Raman data suggesting a partial restoration in the graphitic lattice while the N-doping explains the observed upshifting of Raman peaks. As before, high resolution spectra of the C 1s peaks for the various films allowed the spectral contributions of various surface groups to be quantified. Fig. 5.9 (a) and (b) show the C 1s spectral region for pristine and 300 s O_2 plasma treated graphene, as seen previously. Fig 5.9 (c) shows the C 1s peak for graphene which has been exposed to the two-step O_2 and NH_3 plasma treatment. The contributions from the various oxygen moieties have reduced in prominence and two new contributions are seen at binding energies of 286.3 and 287 eV, corresponding to CN groups in sp^2 and sp^3 configurations, respectively. The relative intensities of the peaks corresponding to the spectral contributions in fig. 5.9 (c) should be considered with some caution. These peaks are very close together and limitations in the spectral resolution of the instrumentation preclude completely accurate fitting of these contributions. Nonetheless, the difference between the C 1s peak shown in fig. 5.9 (b) and (c) is stark and serves to illustrate the reduction in oxygen moieties and introduction of peaks due to the presence of CN groups.

Fitting of the N 1s peak revealed that the nitrogen moieties consisted of quaternary, pyrrolic and pyridinic nitrogen as well as amine groups. Pyridinic and

amine groups comprised the majority of the N-dopants. This suggests that nitrogen is most easily incorporated either into the edge regions of the graphene lattice in pyridinic configuration, rather than in the basal plane as in the case of quaternary nitrogen; or as out of plane functional groups in amine configuration. In the case of amine groups it is likely that the oxygen in the surface groups is directly replaced with nitrogen without any restoration of the graphitic structure. It is possible that with further optimisation of the process, more extensive restoration of the graphitic lattice would result in a greater proportion of the pyridinic nitrogen could be converted to quaternary nitrogen. Quaternary N-doped graphene should exhibit more desirable electronic conductivity and carrier mobilities than the other N-dopant configurations and, so, this technique presents a feasible route towards N-doped large area monolayer graphene for device applications.

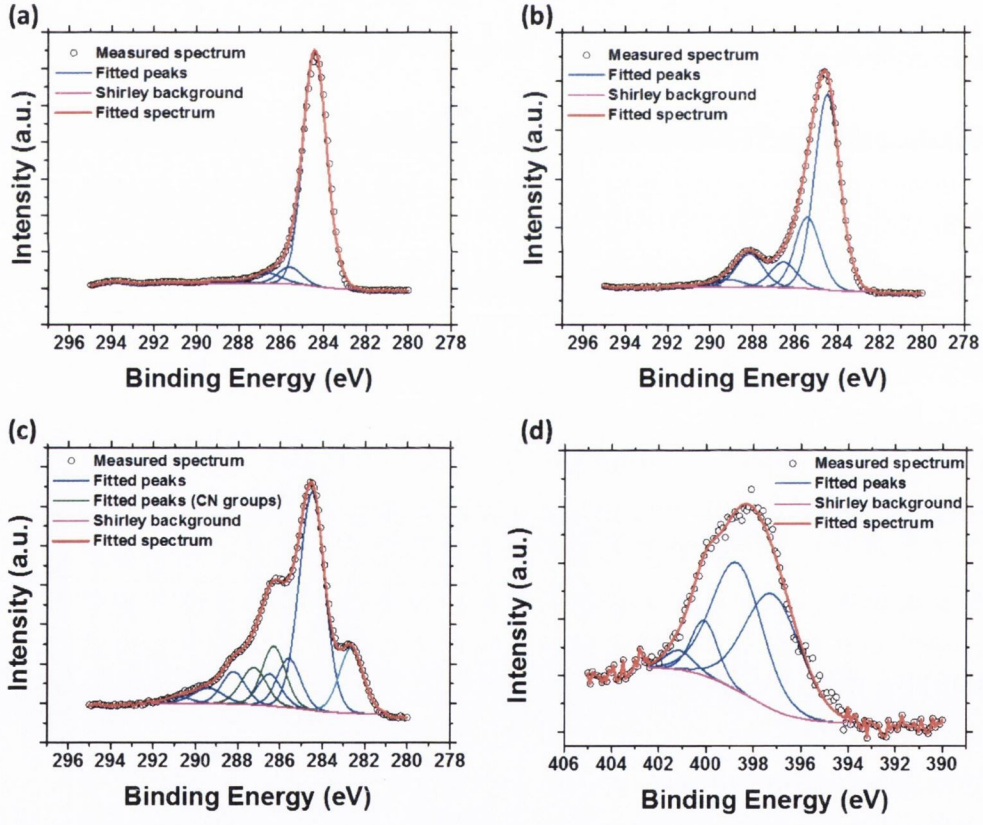

Fig. 5.9. C 1s core level peaks with spectral components fitted for ***(a)*** *pristine,* ***(b)*** *O_2 and* ***(c)*** *NH_3 treated graphene.* ***(d)*** *N 1s core level with fitted components for NH_3 treated graphene.*

5.2.4 Conclusions

Downstream plasma functionalisation was successfully demonstrated on monolayer graphene films and thoroughly characterised by several techniques. O_2 plasma was

used to incorporate oxygen moieties on the surface of the film in a controllable manner. Raman spectroscopy showed the introduction of ever greater levels of crystalline defects as exposure time was increased and this was correlated to XPS which showed a corresponding increase in the level of oxygen and sp^3 carbon sites. A subsequent NH_3 plasma treatment showed a partial restoration of the graphitic lattice with the simultaneous reduction of oxygen and incorporation of nitrogen into the graphene film. The heavy functionalisation of the monolayer material compromised the conductivity of the film and precluded its use as an electrochemical electrode. It is proposed that further work on optimisation of the experimental parameters could allow greater control over the level of functionalisation and still allow the film to remain conductive. In particular, N-doping of the graphitic structure should electronically n-dope the film and introduce a Fermi level shift in the graphene. In order to fully probe this the charge transport behaviour electrical measurements will have to be performed on these films. A route to circumventing the poor conductivity of the functionalised graphene films is to use few layer graphene so that a conductive pathways still exists below the functionalised film surface.

5.3 Multilayer CVD Graphene

In order to study the electrochemical properties of plasma functionalised graphene, MLG was grown on Ni foils *via* CVD. As it has been demonstrated that the plasma functionalisation only affects the surface of carbon films, thicker graphene films should allow for modification of the surface chemistry while still maintaining an electrically conductive film. Deposition of graphitic material on Ni, unlike Cu, is not self limiting after one layer. Two growth mechanisms, vapour phase deposition and segregation of C out of the Ni upon cooling, combine to result in rather thicker graphene films of several layers. As MLG is more mechanically robust to handling than monolayer films, no polymer support was required for transfer to arbitrary substrates after growth. Ni/MLG foils were simply floated on $FeCl_3$ to etch the Ni. The MLG film was then fished out of the etchant to clean water using a glass slide before finally fishing it out with the desired final substrate and allowed to dry. Raman and XPS measurements were performed on both the Ni/MLG growth foil and after transfer to SiO_2. Electrochemical measurements were performed on a substrate of poly(ethylene terephthalate) (PET). Fig. **??** shows the various stages involved in the growth and transfer of MLG films.

5.3.1 Plasma Treatment

Plasma treatment of MLG films was carried out in the usual manner. After CVD growth, Ni/MLG foils were cut to the desired size and exposed to the appropriate plasma conditions. Exposure times of only 2 minutes O_2 were employed for this section of the study. Otherwise standard conditions of 100 sccm flow rate and power of 1 kW were used. All plasma exposures were carried out on the growth Ni/MLG foil prior to transferring to desired substrates.

5.3.2 Raman Spectroscopy

As with monolayer graphene films, Raman spectroscopy was performed to investigate the nature of any changes to the graphitic structure of the MLG films. The spectrum is shown in fig. 5.11 and is, as expected, typical for a multilayer graphitic film with a prominent narrow G peak, small D peak due to the polycrystalline nature of Ni-grown films and a broad 2D of considerably lower intensity than the G peak. Of note is the increase in the intensity of the D peak after plasma treatment. This is related to the introduction of graphitic defects on the MLG surface as oxygen moieties bond to the surface. The increase in intensity of this peak after plasma treatment is significantly less than in the case of the monolayer graphene which had been exposed under the

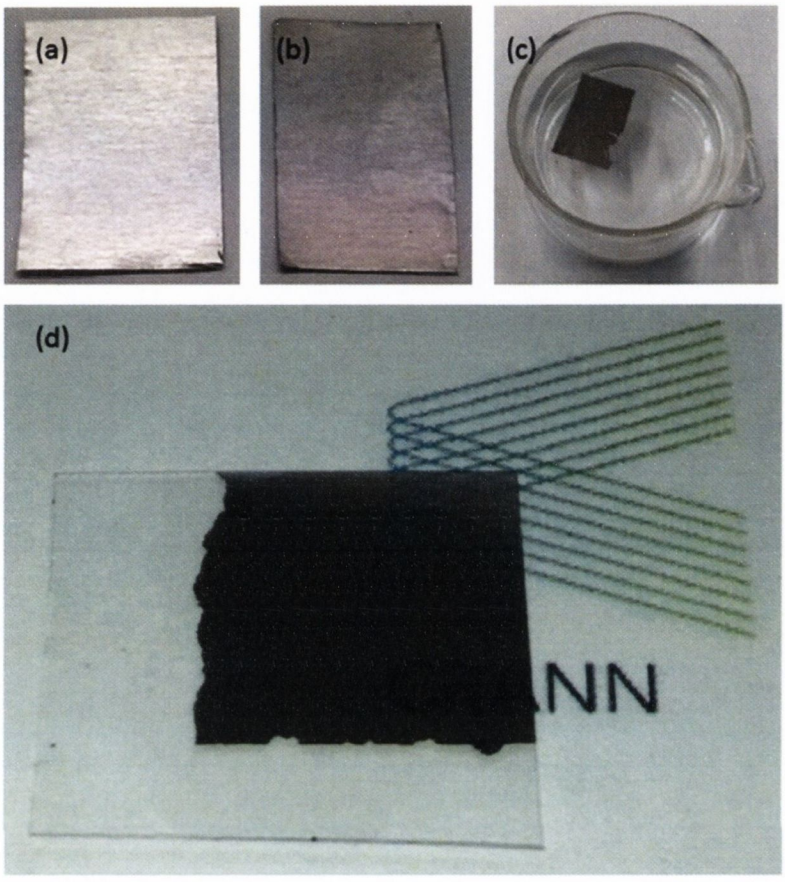

Fig. 5.10. ***(a)*** *Bare Ni foil prior to growth.* ***(b)*** *Ni/MLG foil after CVD.* ***(c)*** *Free-standing MLG film floating on water after etching of Ni foil.* ***(d)*** *MLG transferred to PET substrate showing partial transparency.*

same conditions. This is explained when one considers that the laser used in Raman spectroscopy probes beyond the surface layer in graphitic materials. Consequently, the quantity of defects in the entire volume probed by the laser is significantly less for a thicker film like MLG than for a film like monolayer graphene, which is effectively all surface.

5.3.3 XPS

XPS was performed both on the Ni/MLG foil directly after growth and after transfer to SiO_2 substrates. Survey spectra of pristine and 10 s O_2 plasma treated graphene on both Ni and SiO_2 are shown in fig. 5.12 (a) and (b), respectively. The spectra taken on the Ni/MLG foil show a clear increase in the O 1s core level after plasma treatment, confirming that the small D peak increase for the same sample corresponds, at least in part, to oxygen functionalisation. The inset spectrum shows the strong peaks exhibited by the Ni foil. After transfer to SiO_2, all traces of Ni

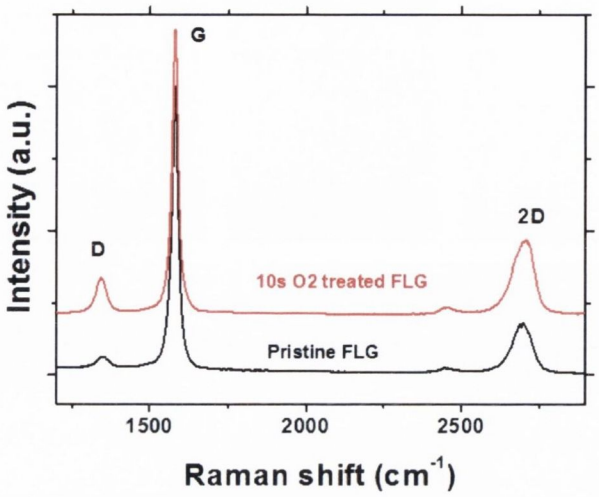

Fig. 5.11. Raman spectra for pristine and O_2 plasma treated MLG on substrates of SiO_2.

peaks disappear from the survey spectrum; confirming the full removal of the growth substrate during the $FeCl_3$ etch. This is of absolute importance if these films are to be employed in electrochemical applications. Ambrosini and Pumera showed that improperly transferred MLG retains Ni nanoparticles which display very prominent redox behaviour that swamps other electrochemical processes at the MLG surface.[150] The oxygen present in the substrate results in similar peak intensities for the O 1s level for both the pristine and plasma treated MLG samples. This prevents the extraction of any useful information regarding the level of oxygen functionalities on the MLG. The presence of characteristic Si peaks in the spectrum confirms that the SiO_2 substrate does, indeed, contribute to the spectrum.

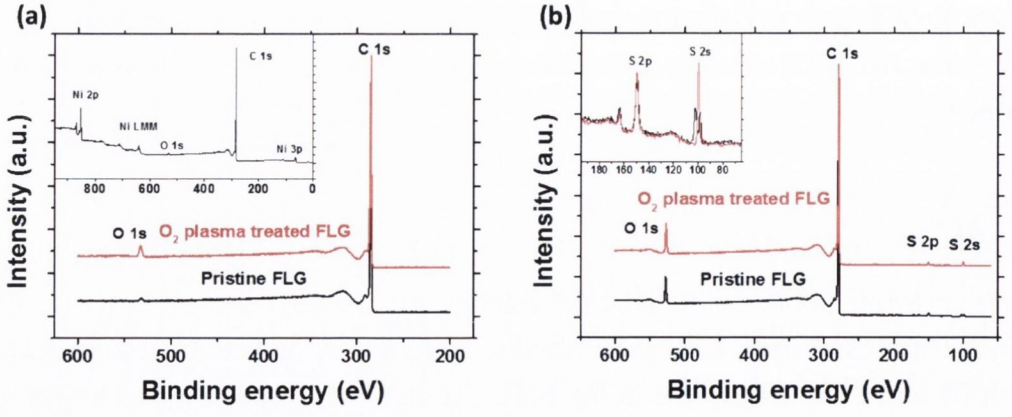

Fig. 5.12. ***(a)*** *Survey spectra for pristine and 10 s O_2 plasma treated MLG as measured on the Ni/MLG growth foil.* ***Inset:*** *Full range spectrum for the pristine MLG film including characteristic Ni peaks.* ***(b)*** *Survey spectra for the same sample set after transfer to SiO_2.* ***Inset:*** *Spectral region magnifying the characteristic Si peaks. All spectra normalised to the C 1s intensity.*

The high resolution C 1s spectra in fig. 5.13 show the increase in oxygen content of the MLG following O_2 plasma treatment by virtue of the increased prominence of the peaks corresponding to oxygen moieties on the shoulder of the C 1s peak. Whether measured on Ni/MLG or after transfer to SiO_2, all pristine and plasma treated MLG films display a very narrow C 1s peak belying the highly graphitic structure of the films. Fitted contributions follow the same procedure as described previously. The sp^3 sites and oxygen moieties present in the untreated film are related to edge termination of crystallites in the MLG. After O_2 plasma treatment the spectral contributions corresponding to oxygen functional groups increase in intensity. The inset of each panel of fig. 5.13 shows the shoulder region of the C 1s peak in higher magnification to highlight the increase in prominence of these contributions.

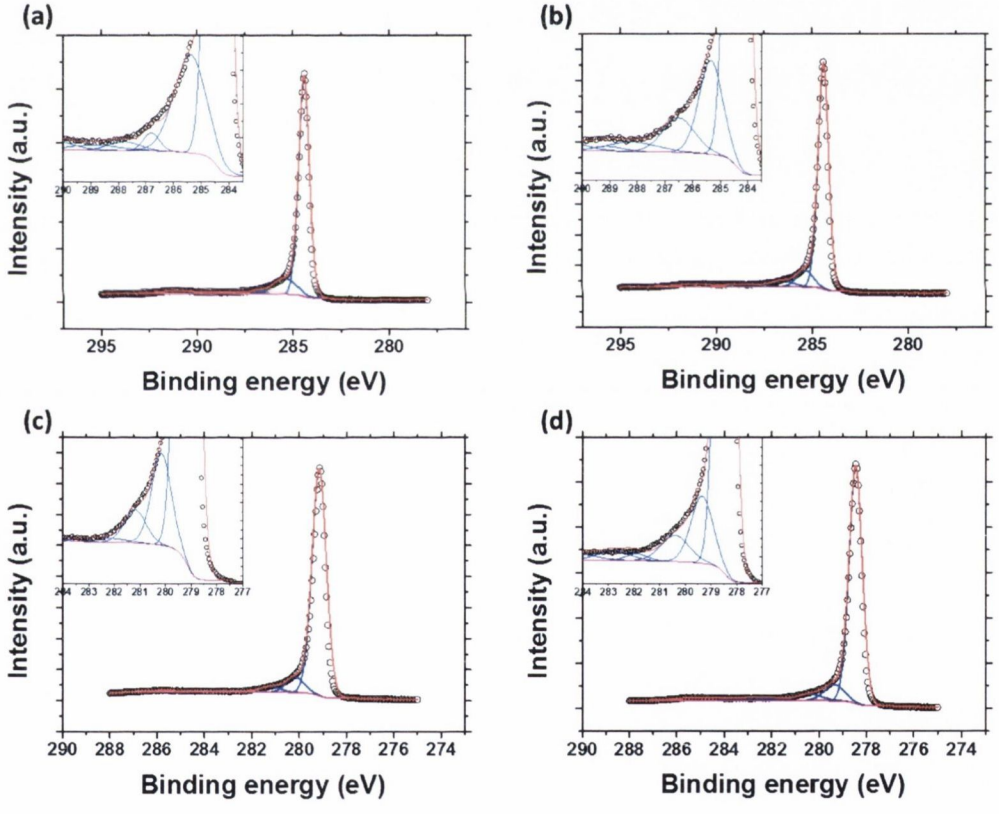

*Fig. 5.13. C 1s peaks for pristine and 10 s O_2 plasma treated MLG as measured on the Ni/MLG growth foil (**(a)** and **(b)**,respectively) and after transfer to SiO_2 (**(c)** and **(d)**, respectively) with spectral contributions fitted. **Inset:** in all cases shows a magnified region of the spectrum to clearly show the fitted contributions.*

5.3.4 *Electrochemical Measurements*

The multilayer nature of MLG means that even after plasma functionalisation, the majority of the graphitic film still retains its electrical conductivity and, so, can

be used for electrochemical measurements and applications. MLG transferred to PET was employed as the working electrode in a standard three electrode cell, as described in chapter 3. Electrochemical measurements of MLG were performed with Dr. Gareth P. Keeley and involved a comparison of pristine and 10 s O_2 plasma treated MLG, in all cases.

Electrochemical Characterisation

Initial electrochemical characterisation was performed using a series of standard electrochemical redox probes to ascertain the nature of the surface chemistry of pristine and plasma treated MLG. The voltammetric responses of both MLG film types were compared to determine information about charging and ET characteristic behaviour of each. Additionally, redox measurements of MLG were compared to equivalent measurements for commercially available EPPG and BPPG. These electrode types represent both highly active and inert graphitic electrodes, respectively.

The background charging behaviour of MLG in KCl is shown in fig. 5.14 (a) and shows an increase in the charging current for the plasma treated MLG compared to the pristine film. This is attributed to pseudocapacitance which arises due to the occurrence of Faradaic processes at the oxygen moieties on the MLG surface. The outer-sphere probe hexaamine ruthenium (II) chloride ($[Ru(NH^3)_6]^{3+}$) was used to investigate ET at the MLG surface. This shows, in fig. 5.14 (b), no significant difference between the MLG films or, indeed, the EPPG or BPPG electrodes. This is consistent with the observed behaviour in the equivalent measurements which compared PyC, O-PyC and N-PyC, which showed no difference in the responses of the different films. Probes with true outer-sphere kinetics are not influenced by the presence of structural defects, surface functional groups or impurities.

Ferri/ferro-cyanide exhibits inner-sphere ET kinetics which are sensitive to the presence of edge plane graphitic sites. Fig. 5.14 (c) shows the voltammetric responses of the various MLG films and commercial electrodes. The poor peak definition for the pristine MLG film is characteristic of very sluggish ET kinetics, but the plasma treated MLG shows a reduction in peak separation indicative of enhanced ET behaviour. A similar trend is observed between BPPG and EPPG, where the former exhibits poor ET kinetics while the latter shows excellent peak definition and a very small peak separation. This suggests that the structural defects introduced in the plasma treated MLG are of central importance to the electrochemical response of this material in certain analytes which are sensitive to edge plane graphitic sites.

In order to electrochemically probe the oxygen functional groups on the surface

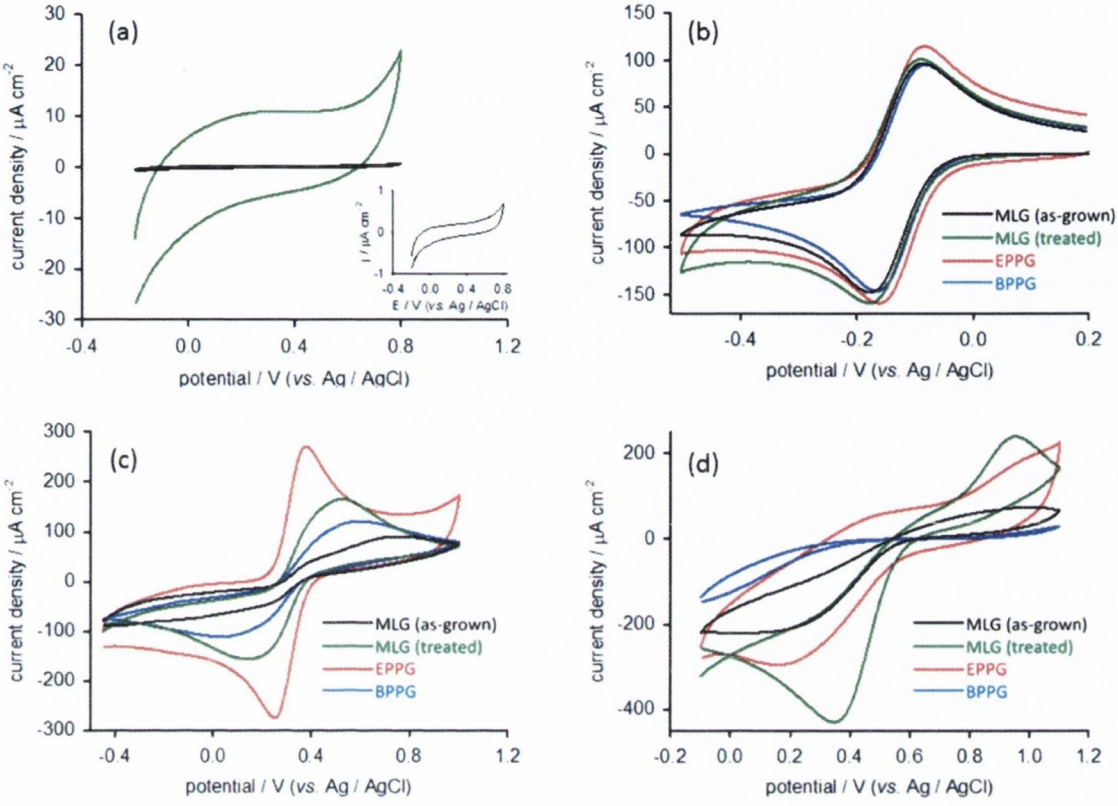

Fig. 5.14. **(a)** *Voltammetric response of pristine and plasma treated MLG in background KCl.* ***Inset:*** *magnification of the response of the pristine film. Comparison of the voltammetric response of both MLG films, EPPG and BPPG in* **(b)** *1 mM $[Ru(NH^3)_6]^{3+}$ in 1 M KCl,* **(c)** *1 mM $[Fe(CN)_6]^{3-/4-}$ and* **(d)** *5 mM $NH_4Fe(SO_4)_2$ in 0.2 M $HClO_4$. Scan rates are 50 mV s^{-1} in each case.*

of the plasma treated MLG, the ammonium iron (III) sulfate ($NH_4Fe(SO_4)_2$, referred to as $Fe^{2+/3+}$) redox probe was used. The ET kinetics of this probe are known to be highly sensitive to the presence of surface oxygen functional groups. Fig. 5.14 (d) shows the response for both MLG films, EPPG and BPPG in this probe. As expected, the pristine MLG film exhibits a rather sluggish response while the plasma treated MLG shows very strong redox peaks, indicating the presence of oxygen moieties on the surface. The extremely low response of the BPPG arises due to the fact that this electrode is freshly cleaved prior to measurements and no surface oxides have had the chance to form in the presence of air. The EPPG, on the other hand, was open to the air for a long time prior to the measurements so some oxygen groups on the surface are inevitable; as evidenced by the appreciable (if still small) response in this $Fe^{2+/3+}$ probe.

Electrochemical Applications

With the kinetics of the pristine and plasma treated MLG having been thoroughly investigated using standard redox probes and related to commercially available electrodes, attention was turned towards implementing MLG electrodes in electrochemical sensing. Accordingly, a series of biological molecules were analysed using CV at MLG films. The voltammetric responses of dopamine, NADH, ascorbic acid and uric acid solutions for MLG, EPPG an BPPG are compared in fig. 5.15. Plasma treated MLG shows an improved performance over pristine MLG by virtue of increased peak currents and reduced peak potentials. The extent of the enhanced response was governed by various features of the electrodes as each molecule is sensitive to different surface properties. NADH is known to be rather insensitive to surface oxides and is most sensitive to the electronic density of states near the Fermi level. As such, this analyte only shows a small improvement for the plasma treated MLG. Ascorbic acid behaves as an inner-sphere redox probe and is sensitive to the surface structure of the electrode. For this analyte, the increase in structural defects and graphitic edge plane sites following plasma treatment account for the improved performance of the plasma treated MLG over the pristine film. Uric acid is highly sensitive to oxygen species and this is reflected in the significantly enhanced response of the plasma treated MLG compared to the pristine film. While EPPG still represents a graphitic electrode with the highest sensitivity towards the analytes studied here, it is clear that the plasma treatment of MLG improves the performance of MLG towards that of EPPG. While MLG is competitive with EPPG for only one analyte shown here, it is clear that this electrode system can be extended to other analytes which exhibit a sensitivity to oxygen functionalised graphitic materials. CVD of MLG followed by O_2 plasma treatment presents a facile route towards inexpensive alternative to the expensive production of commercial electrodes such as EPPG.

5.4 Conclusions

Graphene films were successfully exposed to plasma treatments to introduce functional groups without destroying the film. A range of O_2 plasma treatment times were shown to increase the hydrophilicity and level of defects and oxygen moieties in the graphene film with increased plasma exposure times. A subsequent NH_3 plasma treatment step was found to simultaneously reduce the oxidised graphene while introducing N-dopants in the film. This was observed via the reduction in defect related Raman peaks and the re-emergence of peaks related to

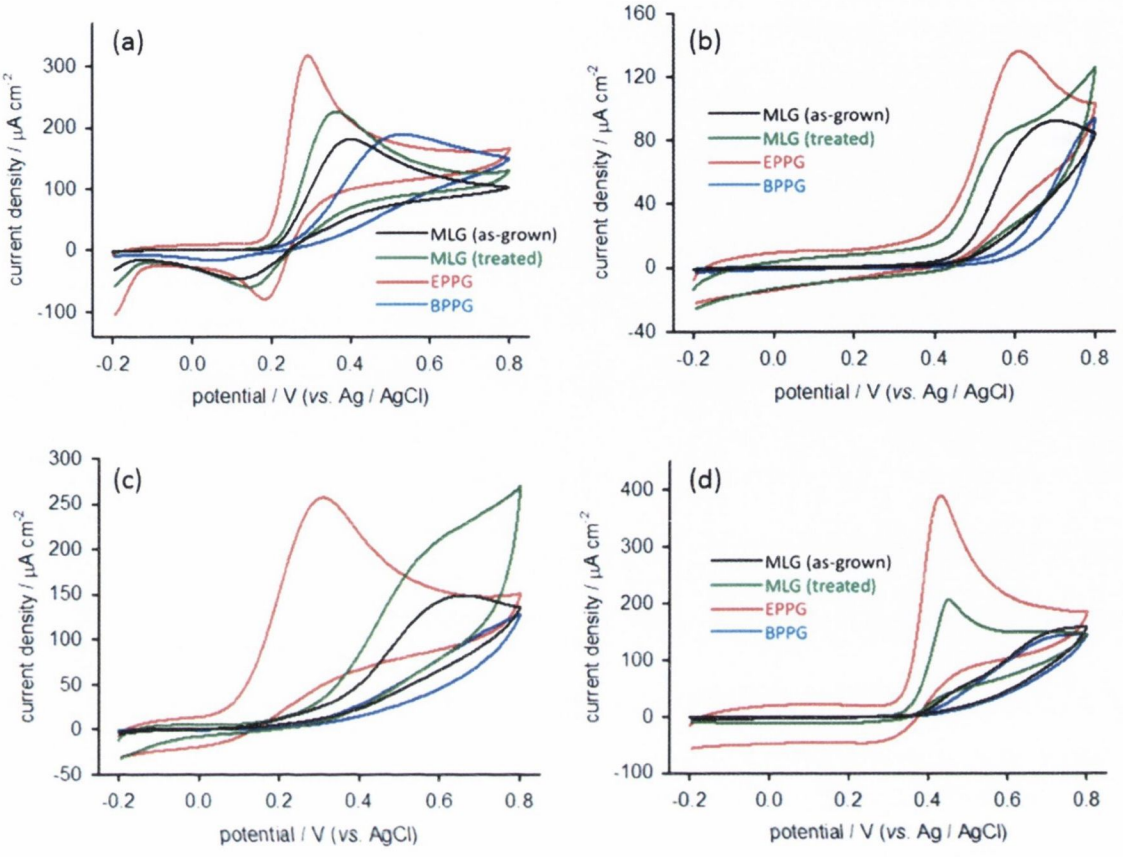

Fig. 5.15. Voltammetric response for MLG films, EPPG and BPPG in 1 mM ***(a)*** *dopamine,* ***(b)*** *NADH,* ***(c)*** *ascorbic acid and* ***(d)*** *uric acid in 0.1 M pH 7 phosphate buffer solution. Scan rates are 50 mV* s^{-1} *in each case.*

long range ordering. XPS showed a reduction in oxygen content and that of sp^3 carbon sites while a nitrogen peak emerged in the spectrum. This functionalised monolayer graphene was found to be unsuited to electrochemical measurements as the conductivity of the film was significantly reduced with the introduction of so many functional groups. To circumvent this problem, MLG was used instead of monolayer films, which allowed for surface functionalisation whilst retaining electrical conductivity. O_2 plasma treatments of MLG resulted in significantly enhanced ET kinetics compared to the pristine MLG by virtue of the defects and oxygen moieties introduced on the film surface. Plasma treated MLG was shown to have potential in electrochemical sensing applications and was even shown to be competitive to EPPG for certain analyte types.

A logical extension of this work involves a fuller investigation of plasma treatment parameters, particularly exposure time. This would allow the level of oxide coverage on the MLG surface to be correlated with the electrochemical performance of the films. Further work should also be carried out investigating potential uses for N-doped MLG

produced via the two-step plasma treatment as used for monolayer films. To take the work in a different direction, electrical device measurements should be performed on functionalised monolayer graphene films. Properties such as the conductivity and primary charge carrier type of functionalised graphene films could be determined via the fabrication of simple electronic devices such as Field Effect Transistors (FETs). These structures are rather easily fabricated using well established lithography and deposition techniques and would yield valuable information about the films.

Chapter 6

Plasma Treatment of Reduced Graphene Oxide

6.1 Introduction

Given that N-doped graphene has so many mooted applications it is necessary to produce large quantities of material for such applications to be realised. One approach to graphene production which has large yields, but at the cost of overall graphene quality, is the reduction of GO. The success of the two-step plasma treatments proved in producing N-doped graphene was reliant on the first plasma treatment creating reactive sites on the graphene basal plane in the form of oxygen groups. GO possesses a very large number of oxygen groups which are susceptible to further functionalisation. This section of this study is concerned with the production of N-doped rGO (N-rGO) *via* simultaneous reduction and N-doping by exposure of GO powder to NH_3 plasma. This process avoids high temperature processing and also the need for any toxic or harmful substances such as hydrazine, which are often involved in the production of rGO. The lack of liquid phase processing of the GO powder should also minimise re-aggregation of rGO flakes and ensure a well exfoliated material.

6.2 GO Synthesis and Plasma Treatment

GO powder was synthesised following a well established procedure initially used by Hummers and Offeman.[151] Graphite powder was exposed to strong oxidising conditions which introduced extensive coverage of surface oxides. The resultant GO readily disperses and exfoliates in water to form monolayer or few layer flakes. Washing of the oxidising agents and allowing the resulting aqueous dispersion to dry yielded dry GO powder.

NH_3 plasma treatments were carried out in a similar manner to previous works on CVD films. For powder samples a amount of GO powder (typically) ~0.5 g was placed in a ceramic crucible and placed ~15 cm from the plasma source. Typically, plasma exposures were carried out for 1 hour. Fig. 6.1 (a) shows GO powder following synthesis. Of note is the brown colour typical of the material. The rGO obtained following NH_3 plasma treatment is shown in fig. 6.1 (b). The colour has changed to black, an oft-used indication that significant reduction in oxygen content has taken place.

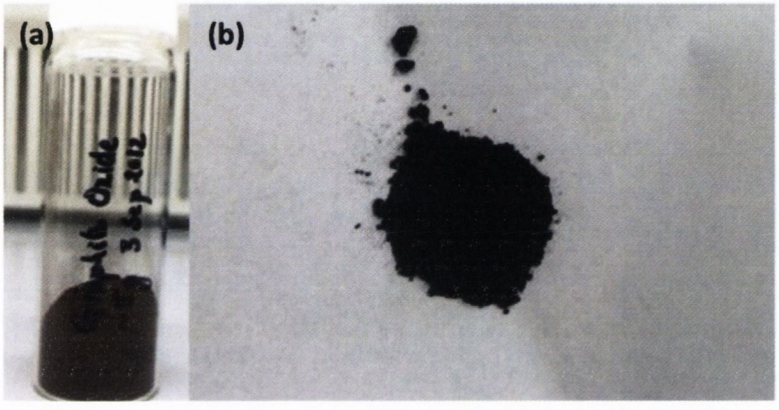

Fig. 6.1. ***(a)*** *GO powder (~5 g) after synthesis and drying.* ***(b)*** *rGO (~200 mg) following NH_3 plasma treatment.*

6.3 XPS

The effects of the NH_3 plasma were investigated using XPS. Samples were measured by pressing powder in to soft indium foils in order to mount in the XPS chamber. This eliminated the possibility of contaminating the sample using adhesives. Survey spectra for GO and plasma treated rGO are shown in fig. 6.2 (a). The GO shows a very high oxygen signal, typical of material with such extensive coverage with oxygen groups. In characteristic peaks are present but can be discounted as they are simply due to the sample mounting procedure and these peaks do not over lap with other characteristic peaks present in the sample. GO has a C/O ratio of 2.2, after plasma treatment the rGO has a C/O ratio of 5.2; indicating the reduced oxygen content. Additionally, the emergence of the N 1s peak for rGO indicates N-doping of the material. These spectral changes confirm the simultaneous reduction and doping of the original GO and, thus, the plasma treated material is henceforth referred to as N-rGO.

Fitting of the C 1s peaks for both GO and N-rGO revealed considerable chemical information about each material. As before, binding energy values for fitted

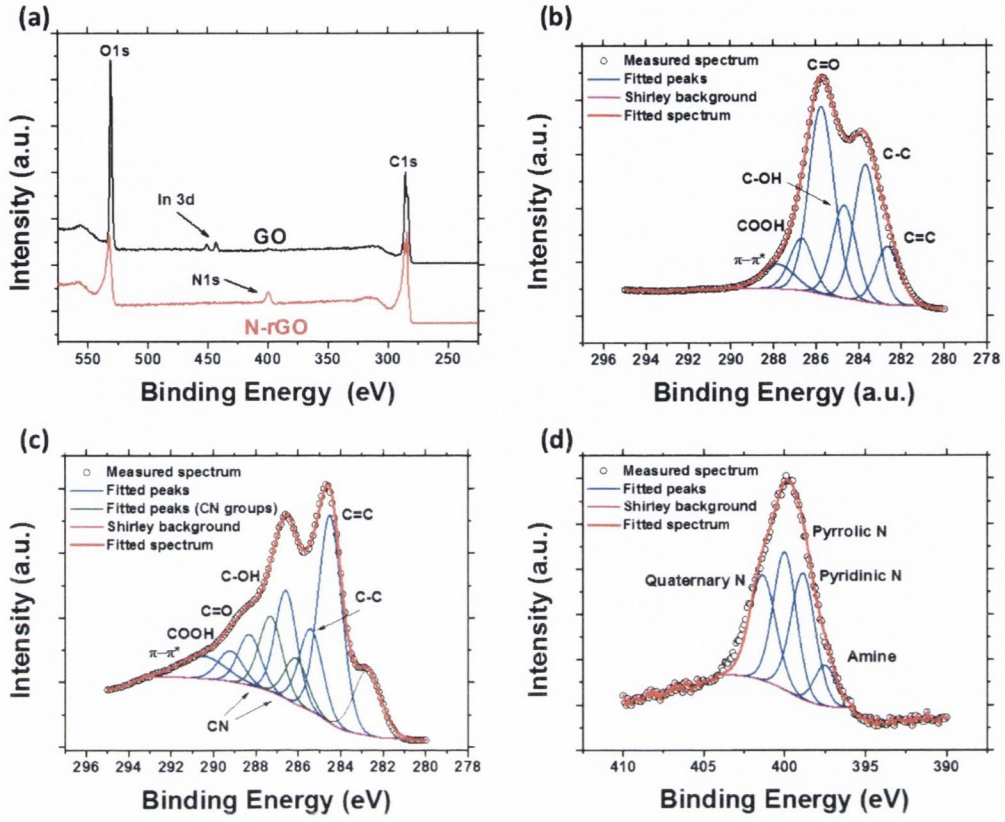

Fig. 6.2. ***(a)*** *Survey spectra for GO and N-rGO.* ***(b)*** *C 1s core level for GO.* ***(c)*** *C 1s core level for N-rGO.* ***(d)*** *N 1s core level for N-rGO.*

contributions to the core level peaks are based on the literature values used in chapter 4. In GO it is noteworthy that the material is so heavily oxidised that the contribution of sp^3 carbon bonds or sp^2 defects is actually greater than that of sp^2 carbon itself. The usual C 1s profile of a primary peak with a higher energy shoulder due to functional groups is replaced by a peak where the shoulder region is, in fact, of greater intensity than the primary graphitic carbon peaks. It must also be noted that GO is a heavily insulating material so it was necessary to utilise charge compensation in order to measure spectra for this material. As a result, the entire C 1s region has been shifted to lower binding energies than expected due to overcompensation by the charge compensation. This does not, however, affect the relative positions and intensities of the various spectral contributions to this peak.

After plasma treatment the contributions from the oxide species and sp^3 carbon sites reduce in intensity while the peak due to graphitic carbon increases in prominence. Two new contributions are seen to emerge on the shoulder of the C 1s and represent nitrogen bonded in sp^2 and sp^3 configurations. As was the case with the similar C 1s fitting in chapter 5 (fig. 5.9 (c)), there are many overlapping peak

contributions which prevents an absolute measure of their relative intensities. Even so, the reduction in oxygen content and introduction of nitrogen spectral features is indisputable. In order to further understand the nature of these nitrogen moieties the N 1s peak of the N-rGO was fitted with spectral contributions. Most of the nitrogen species were found to consist of quaternary, pyrrolic and pyridinic nitrogen with a small amount of amine groups. N-doping in graphitic sites, such as quaternary or pyridinic groups, are particularly electrochemically active and of great interest for various electrochemical applications.

6.4 Raman Spectroscopy

Raman spectroscopy was performed on GO and N-rGO powders and resultant single spectra are shown in fig. 6.3 (a). Both materials show spectra typical of disordered graphitic materials with broad D and G bands somewhat merged together and little to no 2D band. I_D/I_G, in fact, increases slightly after plasma treatment. For GO, I_D/I_G=0.97; while I_D/I_G=1.05 for N-rGO. However, little quantitative information can be inferred from this measurement as both materials exhibit spectra typical of heavily defective or functionalised graphitic materials.

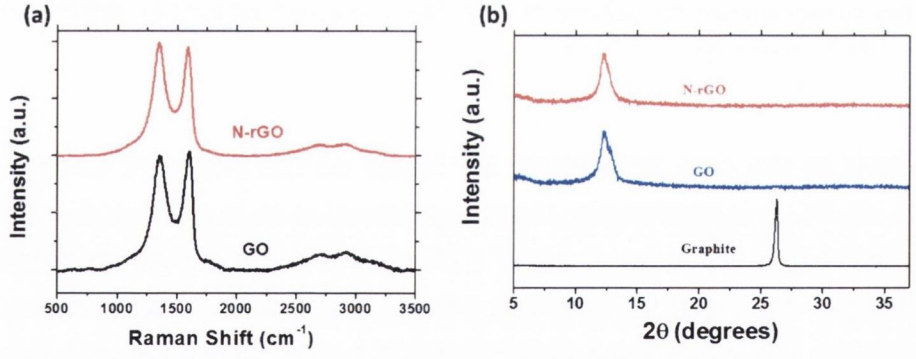

Fig. 6.3. ***(a)*** *Raman spectra for both GO and N-rGO.* ***(b)*** *XRD plots for pristine graphite, GO and N-rGO.*

6.5 X-Ray Diffraction

Powder X-Ray Diffraction (XRD) was performed on GO, N-rGO and the parent graphite powder to further probe the crystallographic structure of the samples. The results for this are shown in fig. 6.3 (b). The shift in the primary graphitic peak after synthesis of GO is typical of heavily oxidised graphitic materials. After plasma treatment, that there is no further shift in this peak as the N-rGO is expected as this

material is still heavily functionalised compared to a pristine graphitic material. The interlayer spacing as measured by XRD does not change significantly when surface functional groups are exchanged. This is consistent with what was determined by Raman spectroscopy.

6.6 Electron Microscopy

6.6.1 Transmission Electron Microscopy

For the preparation of TEM samples, 25 mg of material was dispersed in deionised water (50 mL) and exposed to mild sonication. Microlitre volumes of this dispersion where then dropped on lacey carbon grids and dried in air before analysis. High resolution TEM (HRTEM) measurements and analysis were performed by Mr. Ehsan Rezvani. These images exhibit typical wrinkled morphologies with a mixture of single and few-layer graphene nanosheets. Images of a selection of such N-rGO flakes are shown in fig. 6.4, showing the variation in size and morphology. The accompanying Selected Area Diffraction Patterns (SAED) show discrete diffraction spots indicative of few or bilayer material with high levels of graphitic crystallinity. Some variation of graphitic crystalline ordering was observed across different samples. This disorder is attributed to the presence of the previously discussed functional groups.

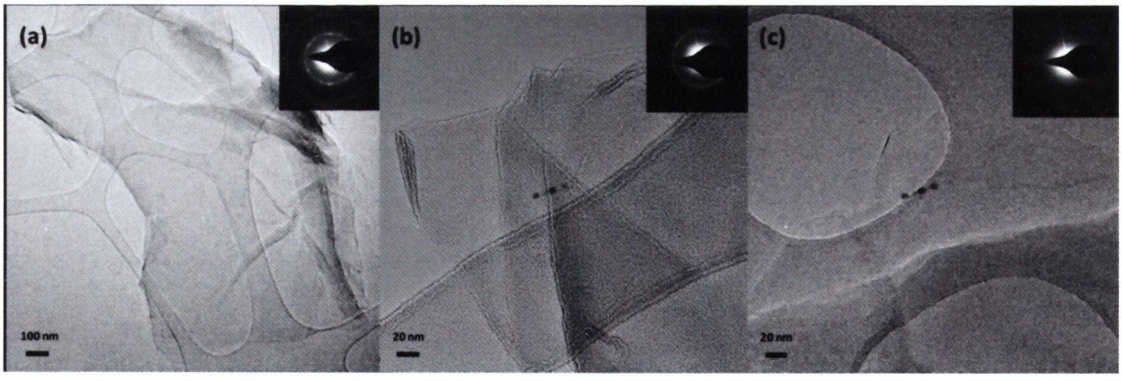

Fig. 6.4. TEM images of various N-rGO flakes with associated SAED patterns.

6.6.2 Scanning Electron and Helium Ion Microscopy

Bulk powder samples of N-rGO were analysed using SEM and Helium Ion Microscopy (HIM). HIM works on the same principle as SEM, but a focussed beam of He-ions are scanned across the surface, generating secondary electrons from the sample which are detected to form an image. Fig. 6.5 (a) shows the bulk structure of the N-rGO powder as viewed by SEM. This is shown in even greater detail in the HIM image in

fig. 6.5 (b), due to the higher resolution and greater depth of focus afforded by this tool. The layered structure of the bulk material is clearly observed. The oxidation of graphite during the production of the parent GO causes the graphitic layers to expand and exfoliate as oxygen groups are formed on the surface of the graphene layers. The nature of the gas phase plasma treatment is such that no re-aggregation of the N-rGO flakes occurs after reduction; resulting in a similar expanded layered structure in the resultant material.

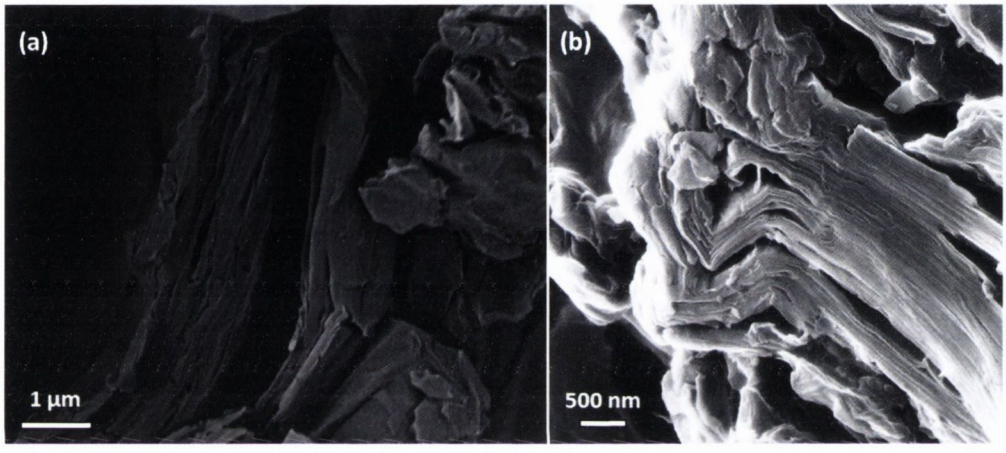

Fig. 6.5. ***(a)*** *SEM and* ***(b)*** *HIM images of N-rGO powder. Secondary electron detector used in each case.*

6.7 Electrochemical Characterisation

The ferri/ferro-cyanide redox probe was used to investigate the redox electrochemistry at N-rGO electrodes. N-rGO powder was dispersed in DMF with mild using sonication and then drop-cast on to otherwise untreated PyC wafers and dried at 80° C. Ag/AgCl and Pt were used as the counter and reference electrodes, respectively. Fig. 6.6 (a) shows the voltammetric responses of bare PyC and N-rGO. At a scan rate of 100 mV s^{-1}, the N-rGO displays a peak to peak separation of ΔE_p =103.7. Employing the Nicholson method to calculate the heterogeneous rate constant then gave k^0=$5.17x10^{-3}$ for the N-rGO. While this value is not as high as the k^0 measured for O-PyC and N-PyC in the chpater 4, it still indicates the good ET kinetics of the material.

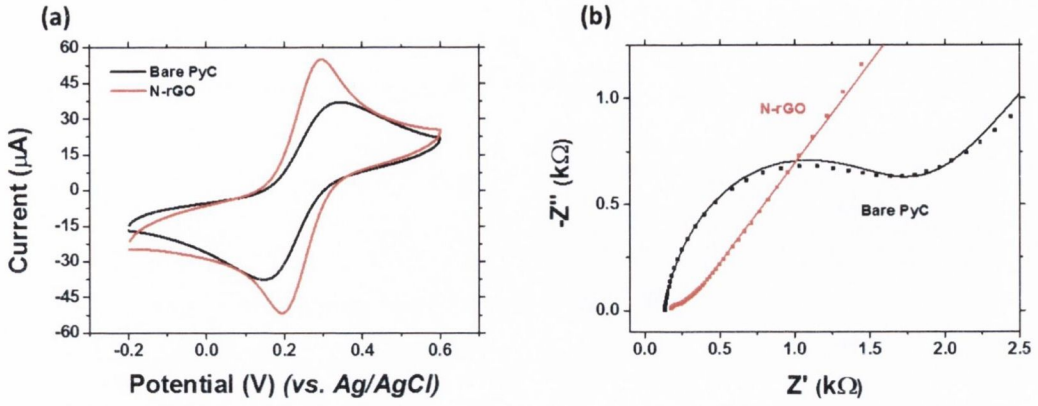

Fig. 6.6. ***(a)*** *Voltammetric response for bare PyC and N-rGO in 1 mM* $[Fe(CN)_6]^{3-/4-}$ *in 1 M KCl. Scan rate is 100 mV* s^{-1}. ***(b)*** *Nyquist plot for the same system.*

EIS further revealed information regarding ET kinetics at the N-rGO electrode in the same redox probe. Fig 6.6 (b) shows the Nyquist plots for bare PyC and N-rGO including Randles equivalent circuit model fittings. This resulted in a calculated value of R_{ct}=182.4 Ω for the N-rGO. Again, this result confirms that this material has rather facile ET kinetics, as also indicated by the voltammetry results.

6.8 Oxygen Reduction Reaction Catalysis

The N-rGO was employed as an electrocatalyst for the ORR to further evaluate the material for practical applications. The ORR involves the splitting of molecular O_2 and is of central importance to hydrogen fuel cell technology. N-doped graphitic materials have been shown to exhibit electrocatalytic behaviour such that they are a potential alternative electrode material to the currently used prohibitively expensive Pt. ORR measurements were carried out in conjunction with Dr. Richard Doyle by dispersing N-rGO in DMF with a microlitre volume of Nafion binder to improve the mechanical robustness of deposited N-rGO films. This dispersion was drop-coated on to GC which served as the electrode support. A rotating Ring Disc Electrode (RRDE) system was employed for the working electrode with Ag/AgCl and Pt as the reference and counter electrodes respectively. 1 M NaOH was used as the electrolyte.

Preliminary evaluation of the N-rGO for ORR was carried out by running CVs in both N_2 and O_2 saturated electrolyte. These were achieved by bubbling the respective gas through the electrolyte for 20 minutes before measurements. Fig 6.7 (a) shows the voltammetric responses for these measurements. While the N_2 saturated electrolyte shows a typical charging current with no Faradaic processes, the O_2 saturated electrolyte shows a clear redox peak which arises due to the reduction of molecular O_2. Further measurements were performed using the

RRDE capability. The secondary Pt working electrode was maintained at a constant potential of 0.45 V while LSV was performed at the N-rGO working electrode. The corresponding LSV is shown in fig. 6.7 (b). The current at the Pt electrode arises due to the presence of H_2O_2 in the electrolyte during the reaction, an indication that the ORR proceeds *via* a desirable four electron pathway.

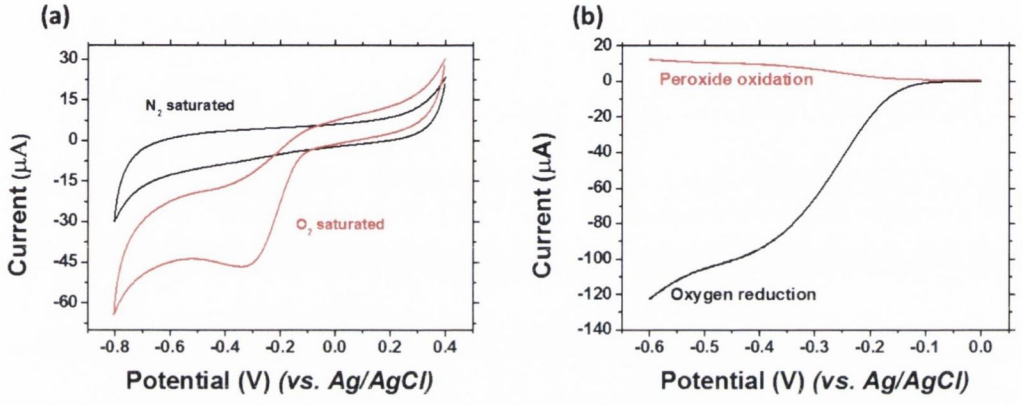

Fig. 6.7. ***(a)*** *Voltammetric response for N-rGO in N_2 (black) and O_2 (red) saturated 1 M NaOH.* ***(b)*** *LSV at N-rGO RRDE showing currents due to oxygen reduction (black) and peroxide oxidation (red); rotation speed of 2000 RPM, scan rate of 20 mV s^{-1}.*

RRDE measurements were performed at a range of rotation speeds and the voltammetric responses of these measurements are shown in fig. 6.8 (c). These range from 500 RPM and increase a further 500 RPM with each scan. The increased current response with rotation speed is due to the faster mass transport of fresh analyte to the electrode at higher speeds. The N-rGO electrode was compared to the bare GC electrode in order to more fully show the electrocatalytic behaviour of the N-rGO. Fig. 6.8 (b) shows the response of RRDE LSV measurements for GC and N-rGO. Of note is the lower onset potential for the N-rGO by approximately 50 mV compared to that of the GC. This indicates that reduction of O_2 at N-rGO occurs at a lower potential than for the bare GC, suggesting some electrocatalytic effect of the N-rGO. The lower steady state current observed for the N-rGO may also be an indication of an electrocatalytic effect. It is likely that the ORR proceeds at N-rGO *via* a different mechanism than at GC. This results in a different number of electrons involved per O_2 molecule reduced and, hence, a differing steady state current.

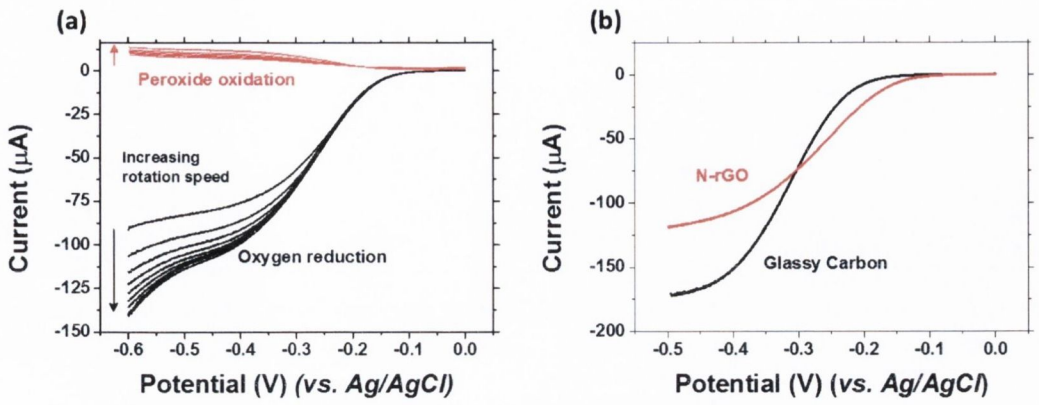

Fig. 6.8. ***(a)*** *LSVs at N-rGO RRDE at various rotation speeds showing currents due to oxygen reduction (black) and peroxide oxidation (red).* ***(b)*** *LSVs at bare GC (black) and N-rGO (red) RRDEs; rotation speed of 2000 RPM. Scan rates of 20 mV s^{-1} throughout.*

6.9 Supercapacitor Measurements

Much current research related to N-doped carbon materials revolves around their application potential as supercapacitor electrodes. Given the ease of large scale production of N-rGO demonstrated here, this material was evaluated as an electrode material for supercapacitors.

6.9.1 Electrode Fabrication

Given the heavily functionalised nature of the N-rGO flakes, this material showed good stability when dispersed in aqueous solutions. Graphitic materials such as CNTs and graphene do not form stable aqueous dispersions without the use of surfactants,[28] but the polar functional groups present on materials such as GO and N-rGO allow ease of handling in aqueous systems. N-rGO electrodes were fabricated by depositing from dispersions on ITO/glass substrates. N-rGO was dispersed in water (0.5 mg ml^{-1}) via tip-sonication for 1 hour prior to loading into the spray tool. The spray tip was maintained at a distance of 35 mm from the substrates throughout the process with the substrates heated to 100° C. A flow of 1 ml min^{-1} was used throughout with an air pressure of ~69 kPa following a standard spray pattern over an area of 9x6 cm^2. Fig. 6.9 (c) shows an image of a typical N-rGO electrode as deposited on to ITO/glass. The amount of material deposited (and, hence, thickness of the N-rGO film) is easily controlled by the number of spray cycles used. Samples used in the measurements below were deposited to a thickness of ~700 nm.

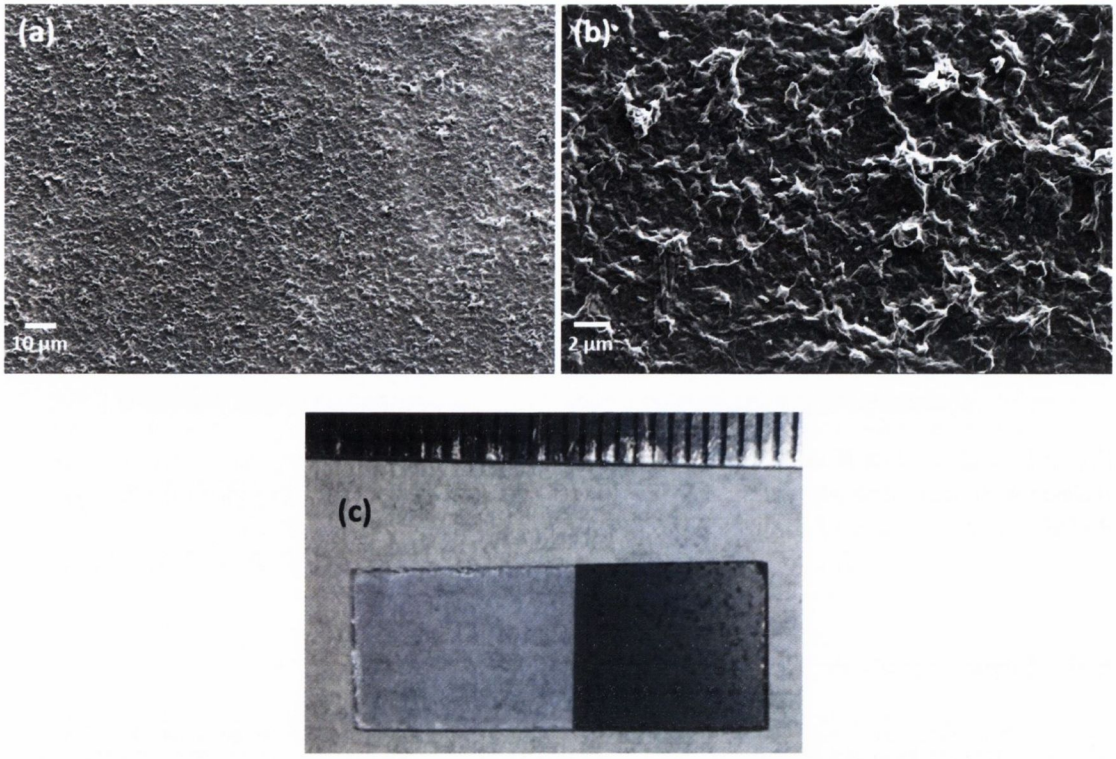

Fig. 6.9. ***(a)*** *and* ***(b)*** *SEM images of the electrode surface at different magnifications. Accelerating voltage of 2 kV, in-lens detector.* ***(c)*** *Optical image of as-deposited N-rGO electrode.*

6.9.2 Electrode Characterisation

Microscopic and spectroscopic techniques were used to characterise the as-deposited N-rGO electrodes prior to any electrochemical measurements.

SEM

Fig. 6.9 (a) and (b) show SEM images of the as-deposited N-rGO electrode surface at different magnifications. This shows a uniform film surface free of defects or obvious areas of material agglomeration. Some surface roughness due to the flaked nature of the material is inevitable and can be seen in the image, but the long range uniformity of the film is evident.

Raman Spectroscopy

Raman spectroscopy was again utilised to investigate the crystallinity and uniformity of the spray-deposited film. Discrete spectra were taken over a 20x20 μm region of the film surface and this data was used to generate an average spectrum for the measured area. This is shown in Fig. 6.10. Inset is an optical micrograph of the electrode surface with the area over which Raman spectra were measured indicated.

That the spectrum for the spray-deposited film here is largely the same as that of the bulk N-rGO powder prior to the spray deposition indicates that no crystalline re-ordering of the material takes place during the electrode fabrication.

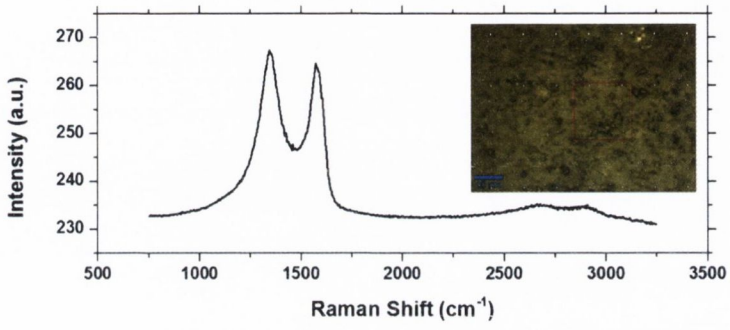

Fig. 6.10. Average Raman spectrum from 10,000 discrete spectra over 20x20 mm area of spray-deposited N-rGO film. (Inset) optical micrograph of the same film, the area marked by the red outline indicates the region over which Raman spectra were measured.

6.9.3 *Electrochemical Measurements*

Electrochemical characterisation was carried out by CV using a three-electrode configuration to investigate any faradaic processes at the electrode surface. Spray deposited electrodes were immersed in 1 M H_2SO_4 electrolyte. The N-rGO-coated ITO was then utilised as the working electrode with Pt and Ag/AgCl as the counter and reference electrodes, respectively. The surface-specific capacitance (C_s) of the electrode was calculated from the coulombic charge stored using formula 6.1.[152] Although, gravimetric specific capacitance is the more normally reported metric when assessing the performance of a supercapacitor electrode, this was deemed inappropriate for these N-rGO electrodes. Measurement of the mass increase of the ITO/glass electrodes after coating with N-rGO proved problematic as the masses involved were so small that accurate and reliable measurement of this was impossible. Additionally, Stoller and Ruoff have expressed concern that calculations of capacitance in F g^{-1} where only a small mass or extremely thin film of active electrode material is used tends to overstate the performance of the material.[153] Hence, in this study, capacitances are dealt with in F cm^{-2} when evaluating electrode performances.

$$C_s = \frac{Q}{ExA} \tag{6.1}$$

The voltammetric response of the N-rGO in acidic media over a number of cycles is presented in fig. 6.11 (a). Peaks were visible on the voltammograms and these were found to increase in prominence with increasing cycle number. A selection of cycles are shown in fig. 6.11 (a). After approximately 600-700 cycles at a scan rate of 100 mV s^{-1} the magnitude of the redox peaks was seen to stabilise and remain invariant with cycle number thereafter. The coulombic charge, Q, was measured by integrating the area under the curve for the reverse sweep and dividing by the scan rate. E is the potential window used; A is the area of the working electrode. The electrode area was measured by photographing the electrode adjacent to a known scale and using basic image processing software to calculate the area.

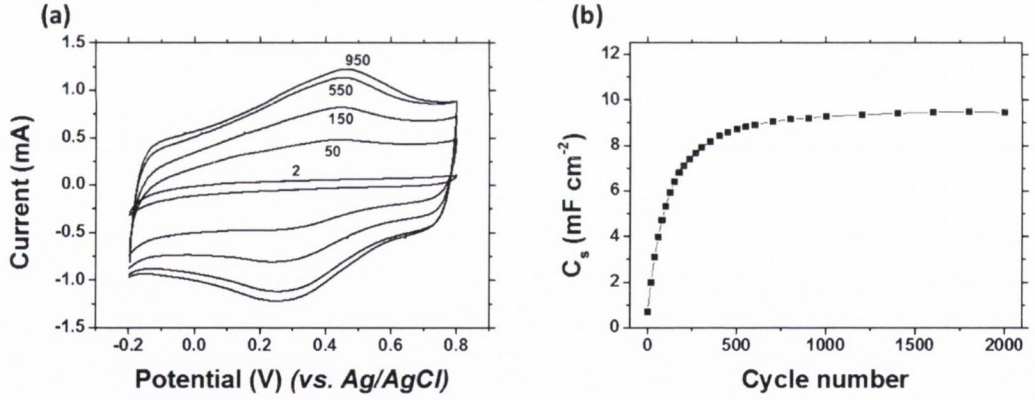

Fig. 6.11. ***(a)*** *Voltammetric response for repeated cycling of N-rGO electrode in 1 M H_2SO_4 at a scan rate of 100 mV s^{-1}. Cycle numbers are marked beside each voltammogram.* ***(b)*** *Specific capacitance (C_s) versus cycle number*

The variation of the specific capacitance with cycle number is illustrated in fig. 6.11 (b). The increase in capacitance up to approximately 700 cycles followed by a levelling off corresponds to the evolution of the redox peaks as shown in fig. 6.11 (a). Once steady-state performance was achieved, a surface specific capacitance of approximately 9.5 mF cm^{-2} was observed for the N-rGO. This value is approximately twice that previously reported for electrodes fabricated from liquid phase exfoliated pristine graphene using an identical spray deposition fabrication process.[154]

Further analysis of the charging mechanism was carried out by analysing the nature of the redox peaks present by recording voltammograms at a range of scan

rates. CV was performed on an N-rGO electrode for 1000 cycles at 100 mV s^{-1} to establish stable reversible redox behaviour. Subsequently, CV was run at the desired range of scan rates. The resultant voltammograms are displayed in fig. 6.12 (a), which indicates reversible redox behaviour at lower scan rates. Higher scan rates show less than reversible behaviour, suggesting that not all of these redox events are accessible at these elevated scan rates. This is consistent with previous discussions of Faradaic processes at electrode surfaces.[155] The relationship between the peak redox currents and scan rate for both forward and reverse sweeps is shown in fig. 6.12 (b). The well-known Randles-Sevcik equation (equation 2.9) shows that for solution based Faradaic processes, the peak redox current will display a linear relationship with the square root of the scan rate.[119,120] The redox events observed here showed a linear relationship between peak redox current and scan rate. These are attributed to surface Faradaic processes, as described in literature;[118] and are attributed to reversible redox reactions at the functional groups on the N-rGO material. It has previously been reported that retaining some amount of oxygen moieties enhances the capacitive performance of graphene material in addition to the presence of nitrogen groups.[156] The partially reduced nature of the N-rGO ensures the presence of some residual oxygen functional groups which provide another pseudo-capacitive contribution to the total material capacitance. The capacitance per unit area reported here is approximately twice that reported previously using the same technique for nonfunctionalised liquid phase exfoliated graphene electrodes.[154]

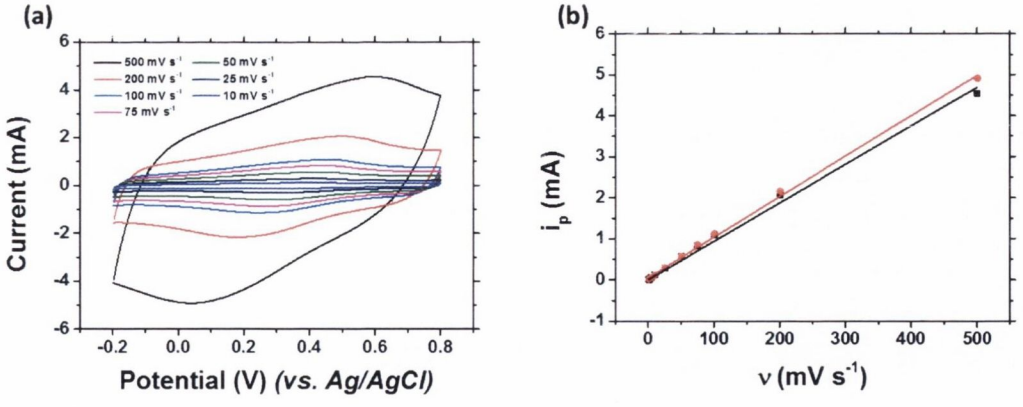

Fig. 6.12. ***(a)*** *Voltammetric response of N-rGO in 1 M H_2SO_4 at a range of scan rates, as indicated.* ***(b)*** *Relationship between peak redox current and scan rate from (a); forward redox peak shown in black, reverse peak shown in red.*

The supercapacitor performance of the N-rGO was related to GO by fabricating GO electrodes in the same manner as for the N-rGO and running an equivalent series of measurements. The GO electrodes displayed behaviour somewhat similar to the

N-rGO insofar as the specific capacitance increased with cycle number. However, as shown in fig. 6.13, the capacitance was significantly lower than that for N-rGO and ultimately the electrode failed before any stable performance was reached. It was found that the spray-deposited GO film delaminated from the ITO substrate over the course of the measurements as the electrode material failed. This was not observed on the N-rGO samples for the same measurements. It was deduced that the GO film undergoes redox processes which are irreversible over time and ultimately causes the film to delaminate. This is illustrated in fig. 6.13 (a) where initially redox peaks emerge with increasing cycle number but after a time these peaks disappear from the voltammogram as the film fails and ultimately the capacitance drops dramatically. The failure of the electrode can clearly be seen in fig. 6.13 (b), as the capacitance drops dramatically as the electrode fails. Voltammetric responses in fig. 6.13 (a) taken after this electrode failure are presented in red to indicate the disappearance of the redox behaviour and ultimately the drop in specific capacitance.

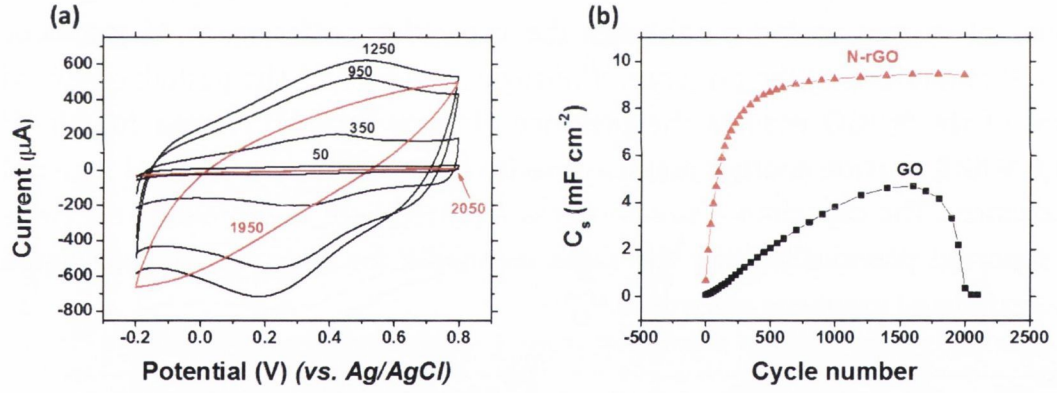

Fig. 6.13. ***(a)*** *Voltammograms for repeated cycling of GO working electrode in 1 M H_2SO_4 electrolyte at a scan rate of 100 mV s^{-1}. Cycle number corresponding to each voltammogram is indicated. Those voltammograms taken after the electrode fails are indicated in red.* ***(b)*** *Comparison of surface specific capacitance versus cycle number for N-rGO (red) and GO (black)*

CV at N-rGO was also performed in basic media. Fig. 6.14 shows the voltammetric response for N-rGO in an electrolyte of 1 M KOH. Of note is the lack of redox peaks when compared to the measurements performed in acidic media. Consequently, the charging currents are significantly smaller than for H_2SO_4 electrolyte given the absence of a pseudocapacitive contribution. The voltammetric profile shown here was typical of all scans across thousands of cycles. Unlike the data presented in the main text, there was no initial period of cycling for reversible behaviour to be established as there were no faradaic processes occurring at the electrode surface in the basic electrolyte. Hence, no "settling in" period was required for these redox processes to become established and fully reversible. Of note is the increase in current

visible at the higher potential portion of the voltammogram. This current increase corresponds to the onset of the Oxygen Evolution Reaction (OER). Performing the CV measurement further in to the OER region would result in an overstated value of C_s and must be considered when characterising supercap electrodes.

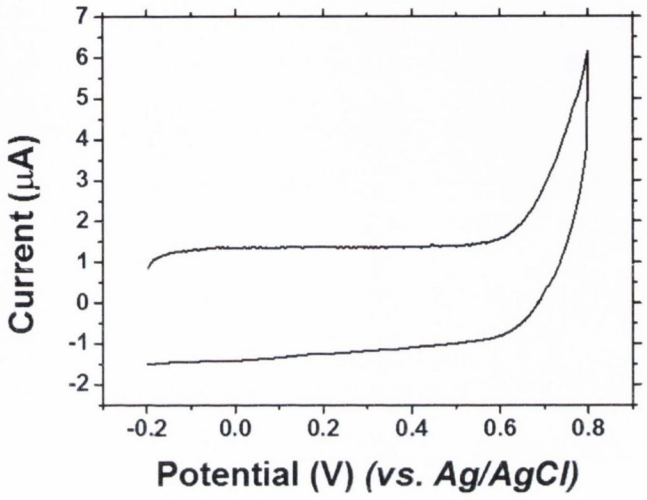

Fig. 6.14. Voltammetric response of N-rGO in 1 M KOH electrolyte

6.10 Conclusions

The NH_3 plasma treatment process was successfully extended to other heavily oxidised graphitic materials related, resulting in the simultaneous reduction and N-doping of GO to form N-rGO. This dry process was confirmed via various spectroscopic and microscopic techniques. That this process allows the production of large quantities of useful material renders it of interest for certain applications where N-doped carbon has been mooted as an inexpensive active material in this application. It was shown that the N-rGO displays some electrocatalytic behaviour towards the ORR, a reaction which is of central importance to the development of cheaper fuel cell technology. Additionally, supercapacitor electrodes were fabricated *via* a facile spray-deposition process. It was demonstrated that these electrodes showed stable pseudocapacitive behaviour after an initial settling phase as the electrodes were cycled.

Future work should include a more detailed analysis of how the nitrogen content of the N-rGO affects the performance of the material in the different applications investigated here. Optimising the N-content should see the catalytic properties of the N-rGO for ORR maximised as well as seeing the capacitance of N-rGO supercapacitors maximised. The mechanism of the ORR at N-rGO can be fully investigated with a

rigorous Tafel analysis of the reaction. This would accurately yield the number of electrons involved in the reaction and clearly reveal the reaction pathway involved. Additionally, it has been demonstrated that exfoliated graphene flakes can be used to boost the efficiency of Dye Sensitised Solar Cells (DSSCs). Initial works have already been carried out which shows that N-rGO improves this DSSC efficiency further.

Chapter 7

TMD/PyC Hybrid Electrodes

7.1 Introduction

This section of work aims to exploit the known catalytic properties of certain TMDs in various electrochemical applications. Electrocatalytic applications of TMDs are most easily realised with the material deposited on a conductive electrode to facilitate charge transfer away form the catalytic surface. Generally, the TMDs used in these experiments are semiconductors with large band gaps and charge transport becomes problematic. In many cases in the literature, the material is processed in dispersions as a result of the synthesis method or from liquid phase exfoliation and this is simply deposited on to conductive electrodes such as GC or Au.[72,157–159] While much detailed information can be garnered from measurements based on these techniques, they are inherently limited to lab-scale experiments with poor scalability. The approach taken in this study combines pre-existing expertise of PyC electrodes with the catalytic capability of MoS_2 by fabricating hybrid electrodes with thin films of MoS_2 atop PyC films. The MoS_2 layer provides a catalytic electrode surface, while PyC ensures a conductive and electrochemically robust electrode platform.

7.2 MoS_2 Synthesis

MoS_2 films were synthesised by a simple vapour phase sulfurisation technique of metallic Mo films as described in chapter 3. Mo was initially deposited on arbitrary substrates *via* electron beam evaporation to various thicknesses. For most measurements, MoS_2 films were grown on PyC. Some characterisation techniques, however, required that the MoS_2 film be grown on SiO_2 wafers. The substrate type is noted in the following measurements. For Mo deposition for electrodes, areas of the PyC substrates were physically masked so that only a 1 cm^2 area of the PyC

sample was exposed to the Mo flux. This ensured a reproducible electrode area from sample to sample.

7.3 Spectroscopic Ellipsometry

Spectroscopic Ellipsometry (SE) was performed by Mr. Chanyoung Yim to accurately measure the thickness of various MoS_2 films. This process allowed the thickness and wavelength dependent optical constants of the MoS_2 film to be determined by measuring the change in the polarisation state of the reflected light from the film surface and developing an optical dispersion model of the film material. The process and model for these measurements of MoS_2 have previously been thoroughly explored.[160] For this process to be successful, it was necessary to grown MoS_2 on SiO_2 wafers. The electron beam evaporation of Mo at various thicknesses included both PyC and SiO_2 substrates, allowing the thickness of the resultant MoS_2 on PyC to be indirectly measured. Fitting the measured SE data to theoretical models allowed the film thicknesses to be determined. It was found that Mo films of 2, 4, and 20 nm were found to increase in thickness by a factor of approximately 2.5 after sulfurisation. The resultant MoS_2 films were found to be approximately 4.5, 10 and 53 nm thick, respectively.

7.4 Raman Spectroscopy

MoS_2 samples 4.5, 10 and 53 nm thick were investigated by Raman spectroscopy and spectral features of both PyC and MoS_2 were observed. Fig. 7.1 (a) shows the Raman spectra for bare PyC and the MoS_2/PyC films of various thicknesses. The D and G band region of the spectra are typical of PyC and are marked in grey in the figure. The peaks observed at ~383 and ~408 cm^{-1} are characteristic of MoS_2 and are denoted the $E^1{}_{2g}$ and A_{1g} peaks and arise due to in plane and out of plane vibrations, respectively. These are marked in cyan in fig. 7.1 (a). All spectra presented are normalised to the intensity of the A_{1g} peak. It is immediately apparent that the relative PyC characteristic signal is much reduced as the MoS_2 layer thickness increases. The greater quantity of MoS_2 present atop of the PyC surface causes a decreased penetration of the Raman laser into the PyC substrate.

Analysis of the MoS_2 characteristic peaks at high spectral resolution divulges information regarding the nature of these films. Fig. 7.1 (b) shows that the spectral region of interest for MoS_2 is rather similar for all samples. However, closer inspection shows a shift in peak position which is dependent on MoS_2 thickness. The coupling between electronic transitions and phonons is modified as the MoS_2 thickness is

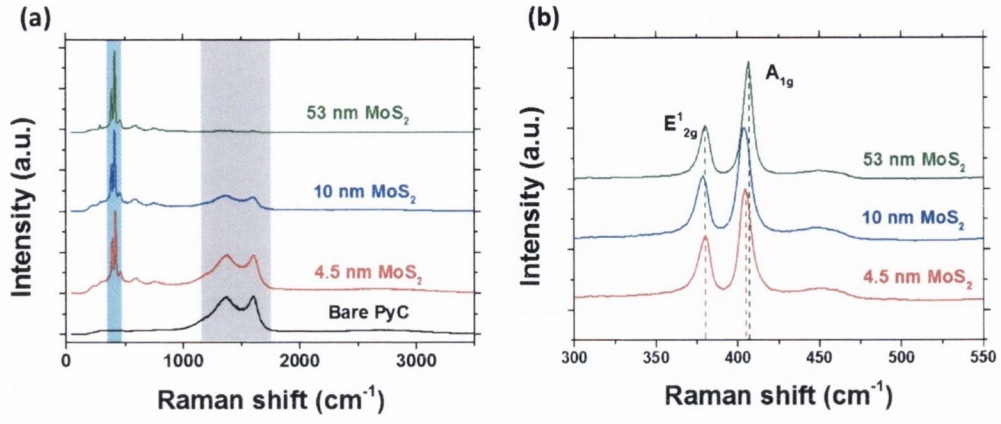

Fig. 7.1. ***(a)*** *Raman spectra for bare PyC and MoS_2/PyC films of various thicknesses, as marked.* ***(b)*** *Higher spectral resolution scans showing the $E^1{}_{2g}$ and A_{1g} peaks characteristic of MoS_2 with peak separations marked by the dotted lines.*

decreased, causing a narrowing of peak separation between the $E^1{}_{2g}$ and A_{1g} modes. This behaviour is reflected here with the dotted lines highlighting a reduction in peak separation of ~ 2 cm^{-1} on going from 53 nm to 4.5 nm thick MoS_2. From this it is apparent that the 4.5 nm film can be considered distinct from bulk MoS_2. The polycrystalline nature of the MoS_2 films should be considered here. The measured thickness represents an average over a large area of the sample, but there will be both thicker and thinner crystallites present.

7.5 XPS

Survey spectra for the MoS_2/PyC films are shown in fig. 7.2 with characteristic photoemission peaks corresponding to C, S and Mo highlighted in grey, yellow and cyan, respectively. As was the case with Raman spectroscopy, the thicker Mo films result in a diminished contribution of spectral features from the PyC. The spectral contributions of the PyC disappear with increasing MoS_2 thickness more rapidly for XPS than for Raman. This is consistent with XPS having a much shallower sampling depth than Raman, XPS being a rather surface sensitive technique.

High resolution scans of the S 2p and Mo 3d spectral regions were recorded and spectral contributions were fitted to the measured data. Fig. 7.3 shows the S 2p spectral region for the various MoS_2/PyC samples with peak contributions fitted in line with the binding energies found by Eda *et al.*[61] The primary contribution to this is the doublet found at a binding energy of approximately 163 eV, which is associated with sulfur typically present in MoS_2 (marked in blue). A second contribution to the spectral region is shifted by approximately 0.85 eV to higher binding energy than the sulfide and was found to increase in intensity for the thinner MoS_2 films. This

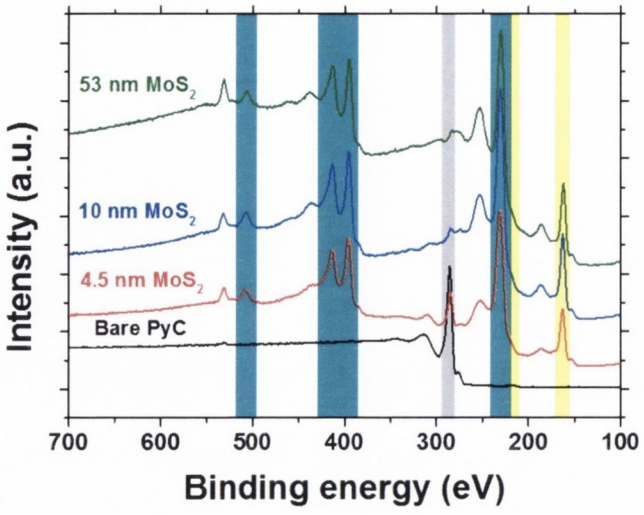

Fig. 7.2. Survey spectra for MoS_2/PyC electrodes. Carbon characteristic core level peaks marked by grey, Mo peaks by cyan and the S peaks by yellow.

doublet can be assigned to "edge-sulfur" or unsaturated sulfur along edge planes of the MoS_2 lattice. This is covered in some detail by Backes *et al.*,[161] where it was found that the edge contribution in films of liquid phase exfoliated MoS_2 significantly increases in intensity relative to the bulk signal as flake size is reduced. Analysis of the edge contributions in this manner is new to the field of XPS of TMDs and allows for a simple metric of the extent of edge sites in a given TMD. It has been widely reported that such uncoordinated sites give rise to enhanced electrocatalytic activity of MoS_2. The thermal treatment involved in the vapour phase sulfurisation during the synthesis ensures that the entire sample will consist of the 2H polymorph. That no 1T MoS_2 is present is confirmed by the lack of a spectral component at a slightly lower binding energy than the 2H MoS_2.

Analysis of the Mo3d spectral region allowed the nature and quantities of any oxides present to be probed. The Mo 3d regions for the various MoS_2/PyC samples are shown in fig. 7.4 with spectral contributions due to Mo in MoS_2, MoO_2 and MoO_3 configurations. The S 2s peak overlaps with the Mo 3d region and must be considered in the fitting as shown, but it does not itself reveal any information regarding the nature of any MoO_x materials. Mo 3d doublets were found to be shifted corresponding to the presence of MoO_2 and MoO_3, in addition to the expected shift due to MoS_2. These contributions were found at binding energies shifted approximately 0.7 and 3.3 eV from the MoS_2 contributions, respectively. The higher oxidation state of the Mo in the MoO_3 caused a greater chemical shift in the binding energy relative to that of the MoO_2. The oxide levels were found to remain invariant with MoS_2 film thickness. As such, any differences in

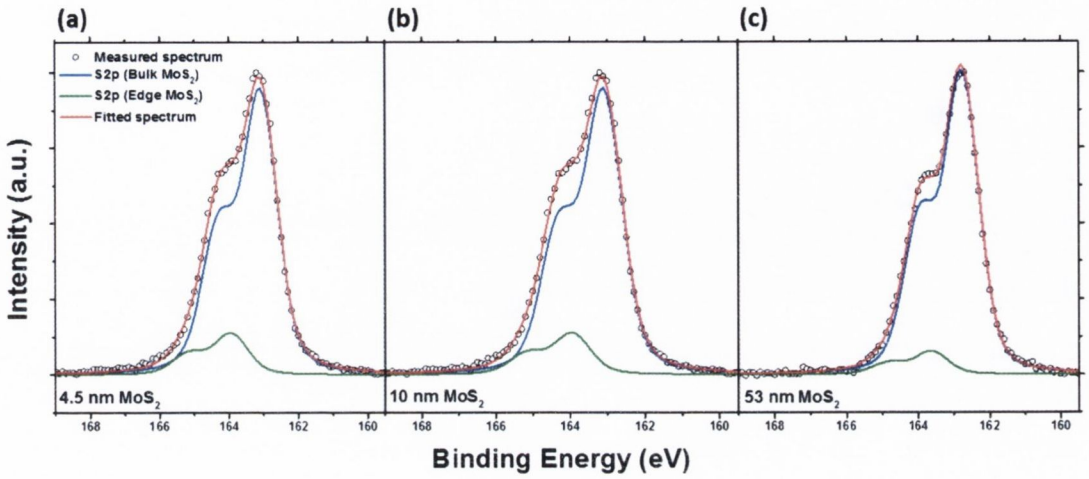

Fig. 7.3. Fitted S 2p core levels for ***(a)*** *4.5 nm,* ***(b)*** *10 nm and* ***(c)*** *53 nm thick MoS_2 films on PyC substrates.*

electrocatalytic performance between the various MoS_2/PyC can be attributed to other features than relative oxide levels.

7.6 Atomic Force Microscopy

AFM analysis of the various films revealed a trend in surface roughness dependent on the thickness of the MoS_2 layer in the hybrid electrodes. Fig. 7.5 shows images of AFM measurements for bare PyC, 4.5 nm MoS_2 and 53 nm MoS_2 films. The lack of surface microstructures or large features over long length scales is immediately apparent. The bare PyC substrate displays an extremely smooth surface with a RMS roughness of 0.55 nm, consistent with the previous AFM studies of as-grown PyC in chapter 4. RMS roughness of 1.52 nm was measured for the 4.5 nm MoS_2 film this was found to increase to a roughness of 3.69 nm for the 53 nm MoS_2 sample.

7.7 Electron Microscopy

7.7.1 Scanning Electron Microscopy

The surface morphologies of the various MoS_2/PyC films were also visualised by SEM. The imaged surfaces were consistent with the measurements taken by AFM. Fig. 7.6 shows the bare PyC and various MoS_2 films. The bare PyC is practically featureless with some level of surface detail for the MoS_2 films which increased in apparent roughness with increasing MoS_2 thickness.

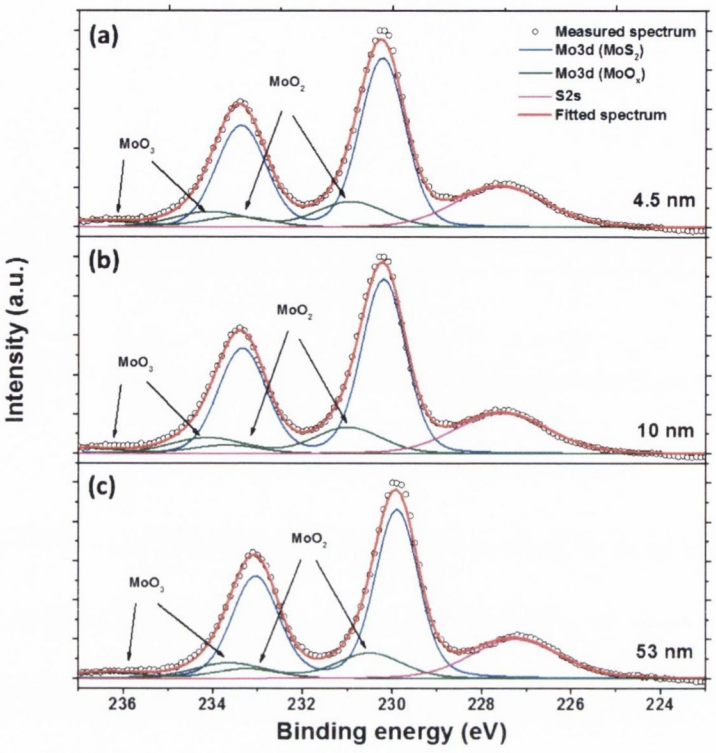

Fig. 7.4. Fitted Mo 3d core levels for **(a)** *4.5 nm,* **(b)** *10 nm and* **(c)** *53 nm thick MoS_2 films on PyC substrates.*

7.7.2 Transmission Electron Microscopy

TEM analysis of MoS_2 materials was performed by Ms. Maria O'Brien, in conjunction with her own related studies on TMDs. The interface between the PyC and MoS_2 layers was investigated via cross sectional TEM. A cross section of a 53 nm MoS_2/PyC film was prepared by depositing protective layers of Au/Pd and Pt on top of the film and then excavating a lamellar section using FIB milling. Fig. 7.7 (a) shows the lamella at low magnification with all substrate and capping layers visible. Fig. 7.7 (b) shows a magnified image of the interface between the PyC and MoS_2. The polycrystalline nature of the MoS_2 is evident here and randomly oriented crystallites can be discerned by virtue of the crystalline planes.

Further TEM analysis was carried out on MoS_2 grown on SiO_2 using an identical technique as used for that grown on PyC. This substrate allowed the MoS_2 film to be transferred to TEM grids via a polymer supported transfer method. A top-down image of such a MoS_2 film is shown in fig. 7.7 (c). Hexagonal symmetry is clearly visible in the lattice. Inset in this panel is a Fast Fourier Transform (FFT) corresponding to this image. The clear hexagonal pattern further confirms the highly crystalline structure of the film with the presence of multiple MoS_2 layers evidenced by the outer ring in

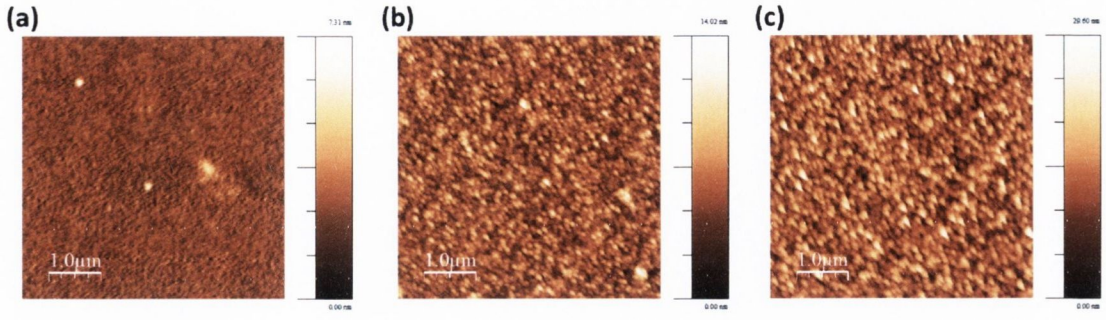

Fig. 7.5. AFM measurements for **(a)** *bare PyC,* **(b)** *4.5 nm MoS_2 and* **(c)** *53 nm MoS_2 films. Scale bar is 1 μm in each case.*

the FFT spot pattern.

TEM analysis allowed the interlayer spacing of the MoS_2 to be measured. Fig. 7.8 (a) shows a portion of a TEM cross-section of a typical MoS_2 layer from a hybrid electrode. Where a crystallite is found to be of the correct orientation, the lattice fringes are clearly visible. Fig. 7.8 (b) shows the intensity profile across the line marked in fig. 7.8 (a), from which an interlayer spacing of approximately 6.6 Å, in accordance with the accepted literature values for this figure.

7.8 HER Catalysis

The electrocatalysis of the HER at MoS_2/PyC hybrid electrodes was primarily investigated by LSV. The hybrid electrode was employed as the working electrode in a three-electrode cell with graphite and a RHE as the counter and reference electrodes, respectively. An electrolyte of 0.5 M H_2SO_4 was used, as is standard practice in the literature for such measurements. All hybrid electrodes were prepared such that the area of the MoS_2 exposed to the electrolyte was 1 cm^{-2}. This allowed a direct comparison of current density in A cm^2 between samples. The voltammetric data is presented in fig. 7.9 where it is apparent that the hybrid electrodes have a significantly lower onset potential compared to the bare PyC substrate. The onset potential for the different materials was determined by measuring the overpotential at which a current density of 2 mA cm^{-2} was achieved. It was found that the bare PyC substrate only achieved this current density at an overpotential of approximately 870 mV. Pt is known to have excellent HER catalytic performance and, as expected, a near-zero overpotential was observed. The onset potential of the MoS_2/PyC films was found to decrease with decreasing film thickness. For 53 nm MoS_2 an onset potential of 540 mV was recorded, the 10 nm film displayed a potential of 520 mV while an onset of 503 mV was observed for the 4.5 nm sample. This is a small but clear reduction of the onset potential which

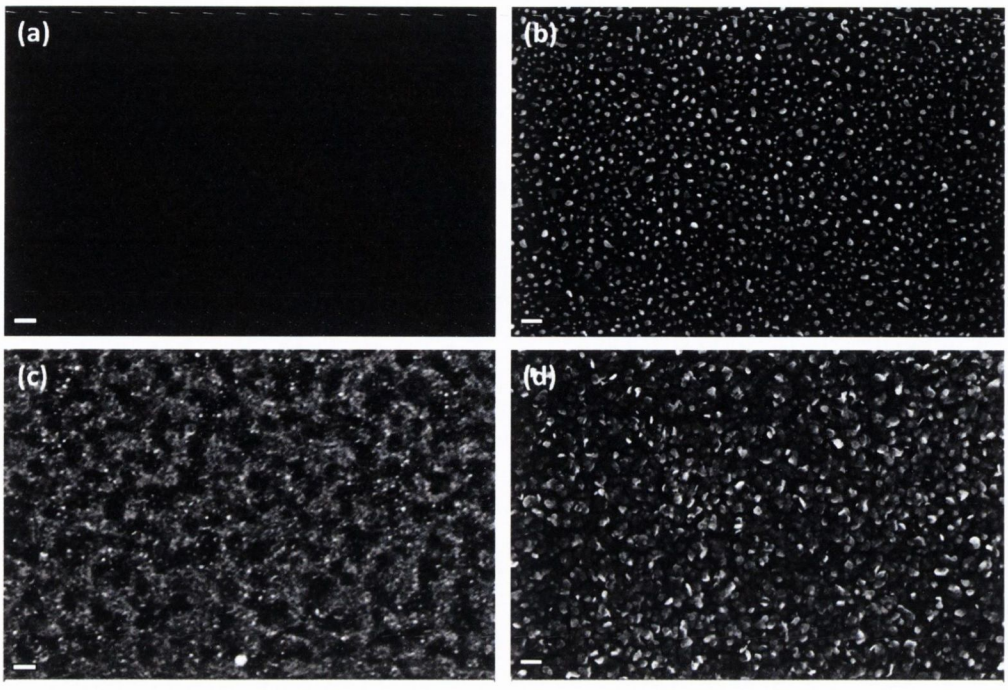

Fig. 7.6. SEM images for **(a)** *bare PyC,* **(b)** *4.5 nm MoS_2,* **(c)** *10 nm MoS_2 and* **(d)** *53 nm MoS_2. In lens detector used. Scale bar is 100 nm in each case.*

trends with film thickness.

Re-plotting the voltammetric data as shown in fig. 7.9 (b) allows one to analyse the slope of the linear portion of the Tafel plot for the various samples in order to reveal details regarding the mechanism by which HER proceeds. It is known that the HER at a Pt electrode proceeds via the so-called Volmer-Tafel mechanism with a Tafel slope of 30 mV decade^{-1}. This is reflected in our experimental data where the Pt electrode exhibited an almost ideal Tafel slope of 31 mV decade^{-1}. Of the MoS_2 films investigated in this study, the thinnest (4.5 nm) displayed the lowest Tafel slope of 95 mV decade^{-1}. The thicker the MoS_2 film, the greater the Tafel slope observed. Li *et al.* proposed that the HER at MoS_2 electrodes proceeds via a Volmer-Heyrovsky mechanism.[72] A modification of the structural morphology of the MoS_2 flakes used in their MoS_2/rGO electrodes caused a reduction in Tafel slope which suggested an increase in site density for H_{ads}, as is consistent with this mechanism. In addition, it was proposed that more effective electronic coupling between the rGO and MoS_2 flakes contributed to the enhanced HER performance. Our investigations indicate a reduction in Tafel slope as the film thickness decreases. It is likely that decreasing the MoS_2 film thickness exposes a greater density of active edge sites on the surface of the film which, in turn, provides a greater number of accessible sites for H_{ads}. This is consistent with behaviour observed by Wang *et al.*, where smaller MoS_2 flakes displayed enhanced HER activity compared to larger ones which was

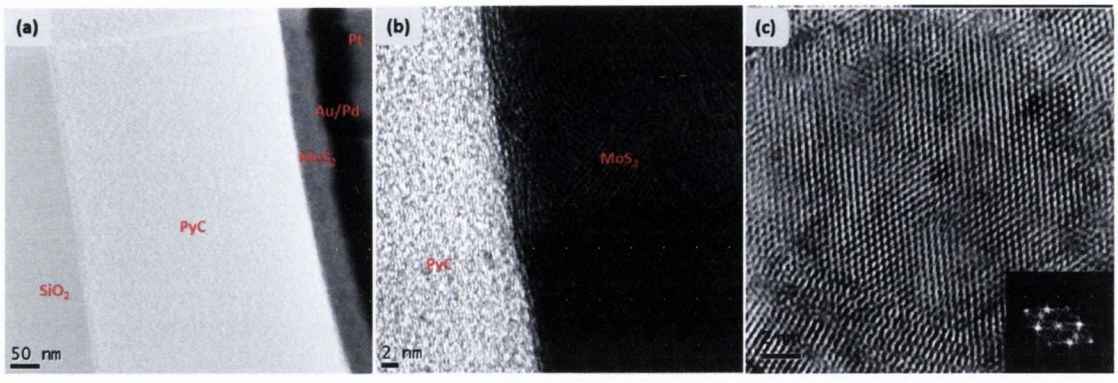

Fig. 7.7. TEM images of **(a)** *MoS_2/PyC film at low magnification showing all layers,* **(b)** *the MoS_2/PyC film interface at higher magnification and* **(c)** *high resolution top-down image of MoS_2 film on TEM grid with evident hexagonal symmetry.* ***Inset:*** *Corresponding FFT image.*

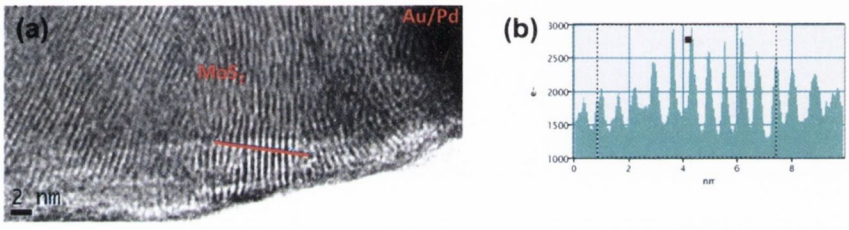

Fig. 7.8. **(a)** *TEM cross-section of MoS_2 layer from hybrid electrode.* **(b)** *Image intensity profile for the marked line in (a) showing interlayer spacing.*

attributed to an increase in unsaturated sulfur sites at the MoS_2 flakes.[159] The Tafel slope of 95 mV decade^{-1} for our thinnest film is well below that of 110 mV decade^{-1} reported for untreated exfoliated MoS_2 flakes[77] and comparable to that observed by Xie *et al.*[157] for calcined synthetic MoS_2 nanosheets and by Li *et al.* for synthetic MoS_2 particles.[72] The MoS_2/rGO hybrid material of Ma *et al.* exhibits an identical Tafel slope.[162] It should be noted that a secondary phenomenon may contribute to the improved HER performance of the thinner MoS_2 films in this study whereby the thinner films facilitate electron migration to the MoS_2 surface.

Further measurements were taken to assess the reliability and stability of the hybrid electrodes. The performances of several hybrid electrodes of the same MoS_2 film thickness were compared with the resultant voltammograms shown in fig. 7.10 (a). Here it is clear that the same onset potential and HER current profile is observed across the three different hybrid electrodes. The cycling stability of the hybrid electrodes is presented in fig. 7.10 (b). This shows the voltammetric response of a hybrid when LSV is performed before and after 1000 CV cycles. This reveals that there is a small increase in the onset potential after multiple cycles, but the degradation is minimal. Despite this, HER electrodes in practical applications are typically operated at constant potentials for constant H_2 evolution, rather than

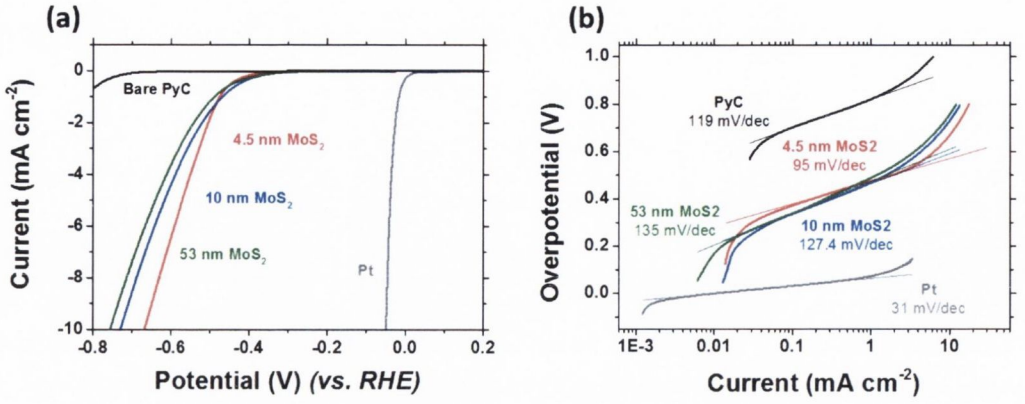

Fig. 7.9. ***(a)*** *Voltammetric response for various MoS_2/PyC hybrid electrodes compared to bare PyC and Pt. Electrolyte of in 0.5 M H_2SO_4 and scan rate of 5 mV s^{-1}.* ***(b)*** *Corresponding Tafel plots with fitted slopes for linear portions.*

continuously sweeping the potential. Fig. 7.10 (c) shows potentiostatic measurements when a constant potential of -0.6 V is applied; showing a steady current response over a number of hours. The initial drop in current magnitude is explained by the formation of H_2 bubbles on the electrode passivating areas of the surface. After an initial settling period a steady current response is observed 60 which corresponds to the continuous formation and detachment of H_2 bubbles on the electrode surface. Behaviour like this has previously been observed in studies of the HER at MoS_2 electrodes.

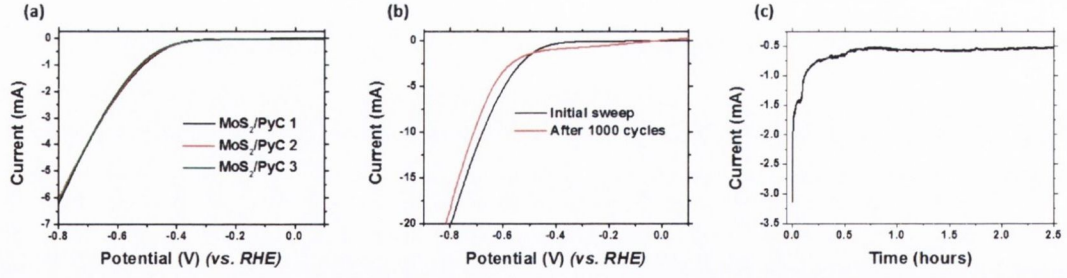

Fig. 7.10. ***(a)*** *LSVs for several hybrid electrodes displaying the same electrocatalytic response.* ***(b)*** *LSVs for a hybrid electrode taken before and after 1000 CV cycles showing minimal degradation in performance.* ***(c)*** *Potentiostatic hydrogen evolution at a potential of -0.6 V, versus RHE.*

7.9 Conclusions

MoS_2 thin films on substrates of PyC are encouraging electrodes for electrocatalysis of the HER. These hybrid electrodes were fabricated by a robust technique and promising catalytic results were demonstrated. This combination of materials leads to a mechanically durable electrode assembly which can easily be manufactured on

a large scale, unlike many techniques which are used in the literature to investigate HER at TMDs. Spectroscopic techniques conform the stoichiometry of the MoS_2 film and also indicate that the thinnest films behave in a manner distinct from bulk MoS_2. The improved performance of the thinner MoS_2 films over thicker ones is correlated to an apparent increase in sulfur defects in the thinner sample. It is proposed that this increase in crystalline defects allows for an increased surface coverage of adsorbed H (H_{ads}) on the electrode surface. Controlling the thickness of the starting Mo layer is sufficient to enhance the HER performance of the resultant electrode. The performance of the MoS_2 catalyst is comparable to other published results for untreated MoS_2 materials. Further engineering of the MoS_2/PyC electrode presented here to increase surface roughness and defect levels could further enhance the HER performance. Additionally, the methods presented here could readily be extended to synthesise electrodes from other members of the TMD family (WS_2, $MoSe_2$ etc.), potentially improving their catalytic performance. TMDs based on Se and Te are typically more conductive than those based on S and these materials could well exhibit greater HER performance in part due to the ease of conduction of electrons to the electrode surface to allow the reaction to proceed.

Chapter 8

Conclusions and Future Outlook

The material presented in this thesis largely concerned the functionalisation and characterisation of graphitic carbon nanomaterials. Initial measurements involved the deposition, *via* CVD, of PyC films followed by the exposure of these films to O_2 and NH_3 plasma treatments. The resultant surface functionalisation with oxygen and nitrogen moieties, respectively, was thoroughly investigated using physical and spectroscopic techniques. Electrochemical characterisation and sensing measurements gave further insight to the nature of the modified film surface. These electrochemical measurements were extended to show that plasma treated PyC displays very promising potential as an inexpensive material for electrochemical sensing applications.

The same plasma treatments were then extended to monolayer graphene and FLG films produced *via* CVD. An extensive understanding of the defects introduced by the plasma treatment was garnered from Raman spectroscopy of monolayer films and related to chemical information provided by XPS. O_2 plasma treated FLG was shown to be a very promising material for electrochemical sensing. The performance of the material in detection of various biological molecules was related to different structural and chemical features of the film surface. In the case of detection of uric acid, plasma treated FLG displayed a detection performance on-par with that of EPPG electrodes; the industry standard of a "best-case" graphitic electrode material.

N-doping of graphitic materials was extended to simultaneous reduction and N-doping of GO to form N-rGO. This facilitated production of N-doped graphene material on large scales for application based measurements. Indeed, N-rGO was successfully shown to catalyse the ORR and, as such, is promising as an inexpensive metal free catalyst in fuel cells. N-rGO was also employed as the active material in supercapacitor electrodes, the functional groups exhibiting pseudocapacitive behaviour to increase the electrode capacitance. Moreover, the fabrication route for

these N-rGO electrodes utilised techniques which are readily scalable, rendering the entire electrode production process as a feasible route towards large scale production.

The final section of this thesis built upon the knowledge and expertise regarding carbon electrodes and electrocatalysis acquired in the previous sections and moved into a newer field of materials electrochemistry. MoS_2 films were grown on PyC and their performance in catalysing the HER was related to the surface chemistry of the MoS_2 layer.

Several techniques proved invaluable over the course of the measurements over the completion of this thesis. In particular, Raman spectroscopy and XPS were essential tools for determining the crystalline microstructure of surface chemistry of the various materials studied. Taken as complimentary characterisation techniques, these allowed a comprehensive understanding of modifications to the surfaces of studied materials. This then allowed a fuller and more complete understanding of the surface processes which occur during electrochemical measurements.

One clear message taken from the work presented here is that simpler materials are often just as suitable as, if not better suited to, applications as more exotic graphitic materials. This is particularly evident from the experiments on graphitic carbon. The synthesis and handling of graphene is much more intricate with scope for causing damage to samples than for materials such as PyC. In electrochemical sensing, the O-PyC films displayed a performance on-par with expensive EPPG electrodes; indicating that one does not need to use expensive materials in order to achieve desired results. PyC was further revealed to be of use as a robust platform for other catalytic layers when used in TMD/PyC hybrid electrodes.

There is ample scope for future works to be undertaken on the basis of the data presented in this thesis. In the case of PyC and FLG electrochemistry, no rigorous investigations into electrochemical sensing have yet been completed for N-doped variants of these materials. The understanding of how different surface features, such as microstructure, electronic density of states and functional groups, influence detection of different analytes has not been explored for N-doped PyC or graphene. Additionally, electronic device measurements of functionalised materials should yield information regarding charge carrier regimes and how the surface moieties influence this.

The clearest extension of the work presented in this document relates to TMD catalysis of the HER. Thus far, only MoS_2 has been investigated as an electrocatalyst for this reaction. Recent upgrades to the facilities available in our lab has made possible the production of selenides, which significantly extends the possibilities of this project. In addition to using different chalcogens, there are a large number of

transition metals which can be converted to TMDs *via* sulfurisation of metal films. Yet more scope for expansion of this project exists in the use of TMD films grown via CVD from oxide precursors. TMDs grown in this manner are typically monolayer, which has positive implications for overcoming conductivity issues in the hybrid electrodes; and the crystallite size can be modulated by growth conditions to produce films with a greater proportion of defects in the chalcogen sub-lattice for enhanced electrocatalytic performance.

Publications and Presentations

1. "CVD growth and processing of graphene for electronic applications", *physica status solidi (b)* **248** (11), 2604-2608

   Shishir Kumar, Niall McEvoy, Hye-Young Kim, Kangho Lee, Nikos Peltekis, Ehsan Rezvani, **Hugo Nolan**, Anne Weidlich, Ronan Daly, Georg S Duesberg

2. "Simultaneous electrochemical determination of dopamine and paracetamol based on thin pyrolytic carbon films", *Analytical Methods* **4** (7), 2048-2053

   Gareth P Keeley, Niall McEvoy, **Hugo Nolan**, Shishir Kumar, Ehsan Rezvani, Michael Holzinger, Serge Cosnier, Georg S Duesberg

3. "Synthesis and analysis of thin conducting pyrolytic carbon films", *Carbon* **50** (3), 1216-1226

   Niall McEvoy, Nikolaos Peltekis, Shishir Kumar, Ehsan Rezvani, **Hugo Nolan**, Gareth P Keeley, Werner J Blau, Georg S Duesberg

4. "Production of 3D-shaped graphene via transfer printing", *physica status solidi (b)* **249** (12), 2515-2518

   Sinéad Winters, Toby Hallam, **Hugo Nolan**, Georg S Duesberg

5. "Functionalisation of graphene surfaces with downstream plasma treatments", *Carbon* **54**, 283-290

   Niall McEvoy, **Hugo Nolan**, Nanjundan Ashok Kumar, Toby Hallam, Georg S Duesberg

6. "Plasma-assisted simultaneous reduction and nitrogen doping of graphene oxide nanosheets", *Journal of Materials Chemistry A* **1** (14), 4431-4435

   Nanjundan Ashok Kumar*, **Hugo Nolan***, Niall McEvoy*, Ehsan Rezvani, Richard L. Doyle, Michael E. G. Lyons, Georg S. Duesberg

7. "Nitrogen-doped pyrolytic carbon films as highly electrochemically active electrodes", *Physical Chemistry Chemical Physics* **15** (42), 18688-18693

Hugo Nolan, Niall McEvoy, Gareth P Keeley, Stephen D Callaghan, Cormac McGuinness, Georg S Duesberg

8. "Highly sensitive, transparent, and flexible gas sensors based on gold nanoparticle decorated carbon nanotubes", *Sensors and Actuators B: Chemical* **188**, 571-575

   Kangho Lee, Vittorio Scardaci, Hye-Young Kim, Toby Hallam, **Hugo Nolan**, Brian E Bolf, Gregory S Maltbie, James E Abbott, Georg S Duesberg

9. Inkjet-defined field-effect transistors from chemical vapour deposited graphene, *Carbon* **71**, 332-337

   Sarah Hurch, **Hugo Nolan**, Toby Hallam, Nina C Berner, Niall McEvoy, Georg S Duesberg

10. "Nitrogen-doped reduced graphene oxide electrodes for electrochemical supercapacitors", *Physical Chemistry Chemical Physics* **16** (6), 2280-2284

    Hugo Nolan, Beatriz Mendoza-Sanchez, Nanjundan Ashok Kumar, Niall McEvoy, Sean O'Brien, Valeria Nicolosi, Georg S Duesberg

11. "Electroanalytical Sensing Properties of Pristine and Functionalized Multilayer Graphene", *Chemistry of Materials* **26** (5), 1807-1812

    Gareth P Keeley, Niall McEvoy, **Hugo Nolan**, Michael Holzinger, Serge Cosnier, Georg S Duesberg

12. "Molybdenum disulfide/pyrolytic carbon hybrid electrodes for scalable hydrogen evolution", *Nanoscale*, **6** (14), 8185-8191

    Hugo Nolan, Niall McEvoy, Maria O'Brien, Nina C Berner, Chanyoung Yim, Toby Hallam, Aidan R McDonald, Georg S Duesberg

* denotes equal contributions from these authors.

Oral presentations

1. "Nitrogen-Doped Carbon Nanomaterials for Energy Conversion and Storage", Stuttgart Nanodays, Stuttgart, 2013

2. "Synthesis and Electrochemical Applications of Graphene-like Pyrolytic Carbon", New Diamond and Nano Carbon Conference, Chicago, 2014

3. "Molybdenum Disulfide/Pyrolytic Carbon Hybrid Electrodes for Scalable Hydrogen Evolution", Flatlands, Dublin, 2014

4. "Synthesis and Electrochemical Applications of Graphene-like Pyrolytic Carbon", International Conference on Diamond and Carbon Materials, Madrid, 2014

Poster presentations

1. "Functionalisation & Characterisation of Nano-Structured Carbon Films for Sensing Applications"

   Smart Surfaces 2012, 6th-9th March, 2012

2. "Synthesis, Functionalisation and Characterisation of Nitrogen Functionalised Thin Pyrolytic Carbon Films"

   Electrochem 2012, 2nd-4th September, 2012

3. "Plasma Treatments of Carbon Nanomaterials"

   Electrograph M18 Dissemination Workshop, November 15th/16th, 2012

4. "Plasma Assisted Simultaneous Reduction and N-Doping of Graphene Oxide Nanosheets for Energy Conversion and Storage"

   ImagineNano-Graphene 2013, 23rd-26th April, 2013

Patents

1. "Transition Metal Dichalcogenide/Pyrolysed Nano-Carbon Hybrid Electrodes"

   UK patent application number: 1410616.5

   US patent application number: 62/011,851

References

[1] H. W. Kroto, J. R. Heath, S. C. O'Brien, R. F. Curl and R. E. Smalley, *Nature*, **318**, 162–163.

[2] S. Iijima, *Nature*, **354**, 56–58.

[3] K. S. Novoselov, A. K. Geim, S. V. Morozov, D. Jiang, Y. Zhang, S. V. Dubonos, I. V. Grigorieva and A. A. Firsov, *Science*, **306**, 666 –669.

[4] W. Benzinger, A. Becker and K. Hüttinger, *Carbon*, **34**, 957–966.

[5] A. Becker and K. Hüttinger, *Carbon*, **36**, 177–199.

[6] A. Becker and K. Hüttinger, *Carbon*, **36**, 201–211.

[7] A. Becker and K. Hüttinger, *Carbon*, **36**, 213–224.

[8] A. Becker and K. Hüttinger, *Carbon*, **36**, 225–232.

[9] M. Brüggert, Z. Hu and K. Hüttinger, *Carbon*, **37**, 2021–2030.

[10] J. Antes, Z. Hu, W. Zhang and K. Hüttinger, *Carbon*, **37**, 2031–2039.

[11] Z. Hu and K. J. Hüttinger, *Carbon*, **39**, 433–441.

[12] B. Reznik and K. Hüttinger, *Carbon*, **40**, 621–624.

[13] J. L. Ely, M. R. Emken, J. A. Accuntius, D. S. Wilde, A. D. Haubold, R. B. More and J. C. Bokros, *The Journal of Heart Valve Disease*, **7**, 626–632.

[14] C. P, M. A, L. S, B. P and B. B, *Journal of biomedical materials research*, **21**, 191–218.

[15] R. Meier, M. Schulz, H. Krimmer, N. Stütz and U. Lanz, *Operative Orthopädie Und Traumatologie*, **19**, 1–15.

[16] A. Koster, H. Matzner and D. Nicholsi, *Nuclear Engineering and Design*, **222**, 231–245.

[17] L. Gerard C, *Pyrolytic carbon nose for hypersonic vehicles*, 1973, US Patent 3,776,139.

[18] P. Winckler, *Clutch with pyrolytic carbon friction material*, 1987, US Patent 4,700,823.

[19] V. Starý, L. Bačáková, J. Horník and V. Chmelík, *Thin Solid Films*, **433**, 191–198.

[20] S. R, G. D, C. MC, L. G, V. F and D. C. R, *The International journal of artificial organs*, **14**, 491–498.

[21] K. S. Kim, Y. Zhao, H. Jang, S. Y. Lee, J. M. Kim, K. S. Kim, J.-H. Ahn, P. Kim, J.-Y. Choi and B. H. Hong, *Nature*, **457**, 706–710.

[22] Y. Wu, Y.-m. Lin, A. A. Bol, K. A. Jenkins, F. Xia, D. B. Farmer, Y. Zhu and P. Avouris, *Nature*, **472**, 74–78.

[23] F. Bonaccorso, Z. Sun, T. Hasan and A. C. Ferrari, *Nature Photonics*, **4**, 611–622.

[24] J. Park, W. H. Lee, S. Huh, S. H. Sim, S. B. Kim, K. Cho, B. H. Hong and K. S. Kim, *The Journal of Physical Chemistry Letters*, **2**, 841–845.

[25] W. Y. Kim and K. S. Kim, *Nature Nanotechnology*, **3**, 408–412.

[26] A. K. Geim and K. S. Novoselov, *Nat Mater*, **6**, 183–191.

[27] Y. Hernandez, V. Nicolosi, M. Lotya, F. M. Blighe, Z. Sun, S. De, I. T. McGovern, B. Holland, M. Byrne, Y. K. Gun'Ko, J. J. Boland, P. Niraj, G. Duesberg, S. Krishnamurthy, R. Goodhue, J. Hutchison, V. Scardaci, A. C. Ferrari and J. N. Coleman, *Nature Nanotechnology*, **3**, 563–568.

[28] M. Lotya, Y. Hernandez, P. J. King, R. J. Smith, V. Nicolosi, L. S. Karlsson, F. M. Blighe, S. De, Z. Wang, I. T. McGovern, G. S. Duesberg and J. N. Coleman, *J. Am. Chem. Soc.*, **131**, 3611–3620.

[29] K. R. Paton, E. Varrla, C. Backes, R. J. Smith, U. Khan, A. O'Neill, C. Boland, M. Lotya, O. M. Istrate, P. King, T. Higgins, S. Barwich, P. May, P. Puczkarski, I. Ahmed, M. Moebius, H. Pettersson, E. Long, J. Coelho, S. E. O'Brien, E. K. McGuire, B. M. Sanchez, G. S. Duesberg, N. McEvoy, T. J. Pennycook, C. Downing, A. Crossley, V. Nicolosi and J. N. Coleman, *Nature Materials*, **13**, 624–630.

[30] D. R. Dreyer, S. Park, C. W. Bielawski and R. S. Ruoff, *Chem. Soc. Rev.*, **39**, 228–240.

[31] C. Gómez-Navarro, R. T. Weitz, A. M. Bittner, M. Scolari, A. Mews, M. Burghard and K. Kern, *Nano Lett.*, **7**, 3499–3503.

[32] H. A. Becerril, J. Mao, Z. Liu, R. M. Stoltenberg, Z. Bao and Y. Chen, *ACS Nano*, **2**, 463–470.

[33] M. Zhou, Y. Zhai and S. Dong, *Analytical Chemistry*, **81**, 5603–5613.

[34] J. T. Robinson, M. Zalalutdinov, J. W. Baldwin, E. S. Snow, Z. Wei, P. Sheehan and B. H. Houston, *Nano Lett.*, **8**, 3441–3445.

[35] A. Reina, X. Jia, J. Ho, D. Nezich, H. Son, V. Bulovic, M. S. Dresselhaus and J. Kong, *Nano Lett.*, **9**, 30–35.

[36] X. Li, C. W. Magnuson, A. Venugopal, R. M. Tromp, J. B. Hannon, E. M. Vogel, L. Colombo and R. S. Ruoff, *Journal of the American Chemical Society*, **133**, 2816–2819.

[37] W. Norimatsu and M. Kusunoki, *Physical Chemistry Chemical Physics*, **16**, 3501–3511.

[38] L. P. Wijesinghe, B. S. Lankage, G. M. Ó'MÃąille, S. D. Perera, D. Nolan, L. Wang and S. M. Draper, *Chemical Communications*, **50**, 10637–10640.

[39] H. Wang, C. Zhang, Z. Liu, L. Wang, P. Han, H. Xu, K. Zhang, S. Dong, J. Yao and G. Cui, *Journal of Materials Chemistry*, **21**, 5430.

[40] L. Qu, Y. Liu, J.-B. Baek and L. Dai, *ACS Nano*, **4**, 1321–1326.

[41] S. Deng, G. Jian, J. Lei, Z. Hu and H. Ju, *Biosensors and Bioelectronics*, **25**, 373–377.

[42] S. Maldonado and K. J. Stevenson, *The Journal of Physical Chemistry B*, **109**, 4707–4716.

[43] Y. Wang, Y. Shao, D. W. Matson, J. Li and Y. Lin, *ACS Nano*, **4**, 1790–1798.

[44] H. Wang, T. Maiyalagan and X. Wang, *ACS Catalysis*, **2**, 781–794.

[45] D. Wei, Y. Liu, Y. Wang, H. Zhang, L. Huang and G. Yu, *Nano Letters*, **9**, 1752–1758.

[46] Z. Jin, J. Yao, C. Kittrell and J. Tour, *ACS NANO*, **5**, 4112–4117.

[47] M. Deifallah, P. F. McMillan and F. Corà, *The Journal of Physical Chemistry C*, **112**, 5447–5453.

[48] C. Zhang, L. Fu, N. Liu, M. Liu, Y. Wang and Z. Liu, *Advanced Materials*, **23**, 1020–1024.

[49] Y. Xin, J.-g. Liu, X. Jie, W. Liu, F. Liu, Y. Yin, J. Gu and Z. Zou, *Electrochimica Acta*, **60**, 354–358.

[50] D. Yu, E. Nagelli, F. Du and L. Dai, *The Journal of Physical Chemistry Letters*, **1**, 2165–2173.

[51] A. L. M. Reddy, A. Srivastava, S. R. Gowda, H. Gullapalli, M. Dubey and P. M. Ajayan, *ACS Nano*, **4**, 6337–6342.

[52] X. Xu, S. Jiang, Z. Hu and S. Liu, *ACS Nano*, **4**, 4292–4298.

[53] J. C. Carrero-Sánchez, A. L. Elías, R. Mancilla, G. Arrellín, H. Terrones, J. P. Laclette and M. Terrones, *Nano Letters*, **6**, 1609–1616.

[54] T. Sharifi, F. Nitze, H. R. Barzegar, C.-W. Tai, M. Mazurkiewicz, A. Malolepszy, L. Stobinski and T. WÃëgberg, *Carbon*, **50**, 3535–3541.

[55] Y.-C. Lin, C.-Y. Lin and P.-W. Chiu, *Applied Physics Letters*, **96**, 133110–133110–3.

[56] E. Raymundo-Piñero, D. Cazorla-Amorós and A. Linares-Solano, *Carbon*, **41**, 1925–1932.

[57] C.-M. Yang and K. Kaneko, *Journal of Colloid and Interface Science*, **255**, 236–240.

[58] M. Chhowalla, H. S. Shin, G. Eda, L.-J. Li, K. P. Loh and H. Zhang, *Nature Chemistry*, **5**, 263–275.

[59] S. Z. Butler, S. M. Hollen, L. Cao, Y. Cui, J. A. Gupta, H. R. Gutierrez, T. F. Heinz, S. S. Hong, J. Huang, A. F. Ismach, E. Johnston-Halperin, M. Kuno, V. V. Plashnitsa, R. D. Robinson, R. S. Ruoff, S. Salahuddin, J. Shan, L. Shi, M. G. Spencer, M. Terrones, W. Windl and J. E. Goldberger, *ACS Nano*.

[60] X. Huang, Z. Zeng and H. Zhang, *Chemical Society Reviews*, **42**, 1934–1946.

[61] G. Eda, H. Yamaguchi, D. Voiry, T. Fujita, M. Chen and M. Chhowalla, *Nano Letters*, **11**, 5111–5116.

[62] A. Splendiani, L. Sun, Y. Zhang, T. Li, J. Kim, C.-Y. Chim, G. Galli and F. Wang, *Nano Letters*, **10**, 1271–1275.

[63] W. S. Yun, S. W. Han, S. C. Hong, I. G. Kim and J. D. Lee, *Physical Review B*, **85**, 033305.

[64] E. Scalise, M. Houssa, G. Pourtois, V. Afanas'ev and A. Stesmans, *Nano Research*, **5**, 43–48.

[65] B. Radisavljevic, A. Radenovic, J. Brivio, V. Giacometti and A. Kis, *Nature Nanotechnology*, **6**, 147–150.

[66] B. Radisavljevic, M. B. Whitwick and A. Kis, *ACS Nano*, **5**, 9934–9938.

[67] J. Puthussery, S. Seefeld, N. Berry, M. Gibbs and M. Law, *Journal of the American Chemical Society*, **133**, 716–719.

[68] J. Zhang, S. Najmaei, H. Lin and J. Lou, *Nanoscale*.

[69] M. Pumera, Z. Sofer and A. Ambrosi, *Journal of Materials Chemistry A*.

[70] Y. Zhao, Y. Zhang, Z. Yang, Y. Yan and K. Sun, *Science and Technology of Advanced Materials*, **14**, 043501.

[71] J. A. Turner, *Science*, **305**, 972–974.

[72] Y. Li, H. Wang, L. Xie, Y. Liang, G. Hong and H. Dai, *Journal of the American Chemical Society*, **133**, 7296–7299.

[73] D. Merki and X. Hu, *Energy & Environmental Science*, **4**, 3878–3888.

[74] D. Kong, H. Wang, J. J. Cha, M. Pasta, K. J. Koski, J. Yao and Y. Cui, *Nano Letters*, **13**, 1341–1347.

[75] H. Wang, D. Kong, P. Johanes, J. J. Cha, G. Zheng, K. Yan, N. Liu and Y. Cui, *Nano Letters*, **13**, 3426–3433.

[76] D. Voiry, H. Yamaguchi, J. Li, R. Silva, D. C. B. Alves, T. Fujita, M. Chen, T. Asefa, V. B. Shenoy, G. Eda and M. Chhowalla, *Nature Materials*, **12**, 850–855.

[77] M. A. Lukowski, A. S. Daniel, F. Meng, A. Forticaux, L. Li and S. Jin, *Journal of the American Chemical Society*, **135**, 10274–10277.

[78] D. Voiry, M. Salehi, R. Silva, T. Fujita, M. Chen, T. Asefa, V. B. Shenoy, G. Eda and M. Chhowalla, *Nano letters*, **13**, 6222–6227.

[79] B. Hinnemann, P. G. Moses, J. Bonde, K. P. Jørgensen, J. H. Nielsen, S. Horch, I. Chorkendorff and J. K. Nørskov, *Journal of the American Chemical Society*, **127**, 5308–5309.

[80] T. F. Jaramillo, K. P. Jørgensen, J. Bonde, J. H. Nielsen, S. Horch and I. Chorkendorff, *Science*, **317**, 100–102.

[81] D. Le, T. B. Rawal and T. S. Rahman, *The Journal of Physical Chemistry C*, **118**, 5346–5351.

[82] J. A. Venables, G. D. T. Spiller and M. Hanbucken, *Reports on Progress in Physics*, **47**, 399.

[83] P. Delhaes, *Carbon*, **40**, 641–657.

[84] Z. J. Hu and K. J. Hüttinger, *Carbon*, **40**, 624–628.

[85] K. J. Hüttinger, *Chemical Vapor Deposition*, **4**, 151–158.

[86] K. J. Hüttinger and W. F. Merdes, *Carbon*, **30**, 883–894.

[87] R. Watwe, H. Bengaard, J. Rostrup-Nielsen, J. Dumesic and J. Nørskov, *Journal of Catalysis*, **189**, 16–30.

[88] J. Gao, J. Yip, J. Zhao, B. I. Yakobson and F. Ding, *Journal of the American Chemical Society*, **133**, 5009–5015.

[89] H. S. Bengaard, J. K. Nørskov, J. Sehested, B. S. Clausen, L. P. Nielsen, A. M. Molenbroek and J. R. Rostrup-Nielsen, *Journal of Catalysis*, **209**, 365–384.

[90] L. L. Patera, C. Africh, R. S. Weatherup, R. Blume, S. Bhardwaj, C. Castellarin-Cudia, A. Knop-Gericke, R. Schloegl, G. Comelli, S. Hofmann and C. Cepek, *ACS Nano*, **7**, 7901–7912.

[91] S. Kumar, N. McEvoy, H. Kim, K. Lee, N. Peltekis, E. Rezvani, H. Nolan, A. Weidlich, R. Daly and G. S. Duesberg, *physica status solidi (b)*, **248**, 2604–2608.

[92] X. Li, W. Cai, L. Colombo and R. S. Ruoff, *Nano Lett.*, **9**, 4268–4272.

[93] X. Li, W. Cai, J. An, S. Kim, J. Nah, D. Yang, R. Piner, A. Velamakanni, I. Jung, E. Tutuc, S. K. Banerjee, L. Colombo and R. S. Ruoff, *Science*, **324**, 1312–1314.

[94] I. Chorkendorff, I. Alstrup and S. Ullmann, *Surface Science*, **227**, 291–296.

[95] M. Losurdo, M. M. Giangregorio, P. Capezzuto and G. Bruno, *Physical Chemistry Chemical Physics*, **13**, 20836–20843.

[96] J. E. Harry, *Introduction to Plasma Technology: Science, Engineering and Applications*, John Wiley & Sons.

[97] R. J. Goldston and P. H. Rutherford, *Introduction to plasma physics*, Institute of Physics Pub.

[98] C. V. Raman, *Indian Journal of Physics*, **2**, 387–398.

[99] P. Larkin, *Infrared and Raman Spectroscopy; Principles and Spectral Interpretation*, Elsevier.

[100] J. R. Ferraro, K. Nakamoto and C. W. Brown, *Introductory Raman spectroscopy*, Academic Press.

[101] F. Tuinstra and J. L. Koenig, *The Journal of Chemical Physics*, **53**, 1126–1130.

[102] A. C. Ferrari and J. Robertson, *Physical Review B*, **61**, 14095–14107.

[103] M. S. Dresselhaus, G. Dresselhaus and P. C. Eklund, *Journal of Raman Spectroscopy*, **27**, 351–371.

[104] A. Jorio, M. S. Dresselhaus, R. Saito and G. Dresselhaus, *Raman Spectroscopy in Graphene Related Systems*, John Wiley & Sons.

[105] A. C. Ferrari, *Solid State Communications*, **143**, 47–57.

[106] W. S. Bacsa, J. S. Lannin, D. L. Pappas and J. J. Cuomo, *Physical Review B*, **47**, 10931–10934.

[107] H. Ishida, H. Fukuda, G. Katagiri and A. Ishitani, *Applied Spectroscopy*, **40**, 322–330.

[108] T. Jawhari, A. Roid and J. Casado, *Carbon*, **33**, 1561–1565.

[109] A. C. Ferrari, J. C. Meyer, V. Scardaci, C. Casiraghi, M. Lazzeri, F. Mauri, S. Piscanec, D. Jiang, K. S. Novoselov, S. Roth and A. K. Geim, *Physical Review Letters*, **97**, 187401.

[110] L. G. Cançado, K. Takai, T. Enoki, M. Endo, Y. A. Kim, H. Mizusaki, A. Jorio, L. N. Coelho, R. MagalhÃčes-Paniago and M. A. Pimenta, *Applied Physics Letters*, **88**, 163106.

[111] L. G. Cançado, A. Jorio, E. H. M. Ferreira, F. Stavale, C. A. Achete, R. B. Capaz, M. V. O. Moutinho, A. Lombardo, T. S. Kulmala and A. C. Ferrari, *Nano Letters*, **11**, 3190–3196.

[112] H. Hertz, *Annalen der Physik*, **267**, 983–1000.

[113] A. Einstein, *Annalen der Physik*, **322**, 132–148.

[114] M. Prutton, *Introduction to surface physics*, Clarendon Press.

[115] D. P. Woodruff and T. A. Delchar, *Modern techniques of surface science*, Cambridge University Press.

[116] A. C. Fisher, *Electrode Dynamics*, Oxford University Press.

[117] R. G. Compton and C. E. Banks, *Understanding Voltammetry*, World Scientific.

[118] D. Pletcher and S. E. Group, *Instrumental methods in electrochemistry*, Ellis Horwood.

[119] P. Zanello, *Inorganic Electrochemistry: Theory, Practice and Applications*, Royal Society of Chemistry.

[120] P. T. Kissinger and W. R. Heineman, *Journal of Chemical Education*, **60**, 702.

[121] J. E. Randles, *Discussions Of The Faraday Society*, **1**, 11–19.

[122] P. J. Goodhew, F. J. Humphreys and R. Beanland, *Electron microscopy and analysis*, Taylor & Francis.

[123] N. McEvoy, N. Peltekis, S. Kumar, E. Rezvani, H. Nolan, G. P. Keeley, W. J. Blau and G. S. Duesberg, *Carbon*, **50**, 1216–1226.

[124] S. Ranganathan, R. McCreery, S. M. Majji and M. Madou, *Journal of The Electrochemical Society*, **147**, 277–282.

[125] J. Kim, X. Song, K. Kinoshita, M. Madou and R. White, *Journal of The Electrochemical Society*, **145**, 2314–2319.

[126] A. Singh, J. Jayaram, M. Madou and S. Akbar, *Journal of The Electrochemical Society*, **149**, E78–E83.

[127] M. Schreiber, T. Lutz, G. P. Keeley, S. Kumar, M. Boese, S. Krishnamurthy and G. S. Duesberg, *Applied Surface Science*, **256**, 6186–6190.

[128] M. Hadi, A. Rouhollahi and M. Yousefi, *Journal of Applied Electrochemistry*, **42**, 179–187.

[129] T. Kwon, H. Nishihara, H. Itoi, Q.-H. Yang and T. Kyotani, *Langmuir*, **25**, 11961–11968.

[130] R. Liu, D. Wu, X. Feng and K. Müllen, *Angewandte Chemie*, **122**, 2619–2623.

[131] G. P. Keeley, N. McEvoy, S. Kumar, N. Peltekis, M. Mausser and G. S. Duesberg, *Electrochemistry Communications*, **12**, 1034–1036.

[132] X. Mei and J. Ouyang, *Carbon*, **49**, 5389–5397.

[133] H. L. Poh, F. Šaněk, A. Ambrosi, G. Zhao, Z. Sofer and M. Pumera, *Nanoscale*, **4**, 3515.

[134] O. C. Compton, D. A. Dikin, K. W. Putz, L. C. Brinson and S. T. Nguyen, *Advanced Materials*, **22**, 892–896.

[135] D. Sun, X. Yan, J. Lang and Q. Xue, *Journal of Power Sources*, **222**, 52–58.

[136] Y. Shao, S. Zhang, M. Engelhard, G. Li, G. Shao, Y. Wang, J. Liu, I. Aksay and Y. Lin, *Journal of Materials Chemistry*, **20**, 7491–7496.

[137] X. Li, H. Wang, J. T. Robinson, H. Sanchez, G. Diankov and H. Dai, *Journal of the American Chemical Society*, **131**, 15939–15944.

[138] J. Kim, D. Jung, Y. Park, Y. Kim, D. W. Moon and T. G. Lee, *Applied Surface Science*, **253**, 4112–4118.

[139] B. Ruelle, S. Peeterbroeck, R. Gouttebaron, T. Godfroid, F. Monteverde, J.-P. Dauchot, M. Alexandre, M. Hecq and P. Dubois, *Journal of Materials Chemistry*, **17**, 157–159.

[140] K. K. Cline, M. T. McDermott and R. L. McCreery, *J. Phys. Chem.*, **98**, 5314–5319.

[141] Richard L. McCreery and Mark T. McDermott, *Analytical Chemistry*, **84**, 2602–2605.

[142] X. Ji, C. E. Banks, A. Crossley and R. G. Compton, *ChemPhysChem*, **7**, 1337–1344.

[143] L. Xiong, C. Batchelor-McAuley, K. R. Ward, C. Downing, R. S. Hartshorne, N. S. Lawrence and R. G. Compton, *Journal of Electroanalytical Chemistry*, **661**, 144–149.

[144] A. N. Patel, M. G. Collignon, M. A. O'Connell, W. O. Y. Hung, K. McKelvey, J. V. Macpherson and P. R. Unwin, *Journal of the American Chemical Society*, **134**, 20117–20130.

[145] R. S. Nicholson, *Analytical Chemistry*, **37**, 1351–1355.

[146] M. E. G. Lyons and G. P. Keeley, *Sensors*, **6**, 1791–1826.

[147] E. Mahé, D. Devilliers and C. Comninellis, *Electrochimica Acta*, **50**, 2263–2277.

[148] H. Nolan, N. McEvoy, G. P. Keeley, S. D. Callaghan, C. McGuinness and G. S. Duesberg, *Physical Chemistry Chemical Physics*, **15**, 18688–18693.

[149] G. P. Keeley, N. McEvoy, H. Nolan, S. Kumar, E. Rezvani, M. Holzinger, S. Cosnier and G. S. Duesberg, *Analytical Methods*, **4**, 2048–2053.

[150] A. Ambrosi and M. Pumera, *Nanoscale*.

[151] W. S. Hummers and R. E. Offeman, *Journal of the American Chemical Society*, **80**, 1339–1339.

[152] L. Mao, K. Zhang, H. S. O. Chan and J. Wu, *Journal of Materials Chemistry*, **22**, 1845–1851.

[153] M. D. Stoller and R. S. Ruoff, *Energy & Environmental Science*, **3**, 1294.

[154] B. Mendoza-Sánchez, B. Rasche, V. Nicolosi and P. S. Grant, *Carbon*, **52**, 337–346.

[155] Z. Lei, L. Lu and X. S. Zhao, *Energy & Environmental Science*, **5**, 6391–6399.

[156] D. Hulicova-Jurcakova, M. Seredych, G. Q. Lu and T. J. Bandosz, *Advanced Functional Materials*, **19**, 438–447.

[157] J. Xie, H. Zhang, S. Li, R. Wang, X. Sun, M. Zhou, J. Zhou, X. W. D. Lou and Y. Xie, *Advanced Materials*, **25**, 5807–5813.

[158] T. Wang, L. Liu, Z. Zhu, P. Papakonstantinou, J. Hu, H. Liu and M. Li, *Energy & Environmental Science*, **6**, 625–633.

[159] T. Wang, D. Gao, J. Zhuo, Z. Zhu, P. Papakonstantinou, Y. Li and M. Li, *Chemistry - A European Journal*, **19**, 11939–11948.

[160] C. Yim, M. O'Brien, N. McEvoy, S. Winters, I. Mirza, J. G. Lunney and G. S. Duesberg, *Applied Physics Letters*, **104**, 103114.

[161] C. Backes, R. J. Smith, N. McEvoy, N. C. Berner, D. McCloskey, H. C. Nerl, A. OâĂŹNeill, P. J. King, T. Higgins, D. Hanlon, N. Scheuschner, J. Maultzsch, L. Houben, G. S. Duesberg, J. F. Donegan, V. Nicolosi and J. N. Coleman, *Nature Communications*, 2014, **5**, year.

[162] C.-B. Ma, X. Qi, B. Chen, S. Bao, Z. Yin, X.-J. Wu, Z. Luo, J. Wei, H.-L. Zhang and H. Zhang, *Nanoscale*, **6**, 5624–5629.